High-Performance Reconfigurable Piezoelectric Resonators and Filters for RF Frontend Applications

by

Arash Fouladi Azarnaminy

A thesis

presented to the University of Waterloo

in fulfillment of the

thesis requirement for the degree of

Doctor of Philosophy

in

Electrical and Computer Engineering

Waterloo, Ontario, Canada, 2022

Examining Committee Membership

The following served on the Examining Committee for this thesis. The decision of the Examining Committee is by majority vote.

External Examiner	Amir Mortazawi Professor, Department of Electrical Engineering & Computer Science, University of Michigan-Ann Arbor
Supervisor	Raafat R. Mansour Professor, Department of Electrical & Computer Engineering, University of Waterloo
Internal Member	Dayan Ban Professor, Department of Electrical & Computer Engineering, University of Waterloo
Internal Member	William S. Wong Professor, Department of Electrical & Computer Engineering, University of Waterloo
Internal-external Member	John Yeow Professor, Department of Systems Design Engineering, University of Waterloo

Author's Declaration

I hereby declare that I am the sole author of this thesis. This is a true copy of the thesis, including any required final revisions, as accepted by my examiners.

I understand that my thesis may be made electronically available to the public.

Abstract

A conventional RF frontend module consists of many filters where each filter is allocated for a specific frequency band. These filters are connected through multiplexing switch networks to support multi-band wireless standards. Using an individual filter for each frequency band increases the module size, power consumption and cost. Therefore, implementation of reconfigurable filters that can operate at different frequency bands while maintaining key RF performance requirements such as low insertion loss, good linearity and power handling is necessary for manufacturing of future RF frontends.

Acoustic wave resonators based on piezoelectric devices such as Surface Acoustic Wave (SAW) and Bulk Acoustic Wave (BAW) are the most commonly used technologies to manufacture filters for RF applications. The objective of the research described in this thesis is to investigate the feasibility of tunable filter solutions using piezoelectric SAW resonators. A tunable SAW technology which can maintain required performance parameters and can be commercially manufactured will constitute a technological breakthrough in wireless communications.

Thin-Film Piezoelectric on Substrate (TPoS) resonators, based on Aluminum Nitride (AlN) piezoelectric material which are fabricated using commercially available Silicon on Insulator (SOI) PiezoMUMPs process, have been demonstrated. By combining the superior acoustic properties of AlN and single crystalline silicon substrate, this class of resonators achieves ultra-high quality factor (Q) values in excess of 3600. A 3-pole bandpass filter using direct electrical coupling between the resonators has been presented and we have studied the performance of the fabricated filter over a temperature range from -196ºC up to +120ºC and under high power.

For the first time, we have demonstrated the integration of switching elements, based on Vanadium Dioxide (VO_2) phase change material, with Incredible-High-Performance SAW (IHP-SAW) technology which allows us to design and implement switchable and reconfigurable SAW resonators and filters for wireless applications.

Switchable multi-band filters using VO_2 switches strategically imbedded within the resonators of the filter have been demonstrated. A switchable dual-band filter with four switching states and two channels was presented using hybrid integration approach where discrete VO_2 switches were fabricated separately and then integrated with the SAW resonators and filters using wire bonds. The fabricated 5-pole dual-band filter demonstrated good insertion loss in both transmission states but had inadequate performance in terms of isolation between the channels due to the limitations of the hybrid integration approach. Moreover, hybrid integration does not allow us to use more than a few switching elements and cannot be used for the implementation of higher order filters. To address these issues, we have demonstrated the monolithic integration of VO_2 switches using an in-house fabrication process that allows us to fabricate VO_2 switches and SAW resonators and filters on a single chip. A dual-band switchable higher order 7-pole filter with six monolithically integrated VO_2 switches, three for each channel, was demonstrated. The monolithic integration allows the single-chip implementation of the proposed switchable dual-band filter with improved performance along with significant size reduction and ease of manufacturing, paving the path for commercialization of this technology.

Novel reconfigurable SAW resonators and filters with tunable center frequency were also presented for the first time. Tuning of the center frequency between two different states was achieved by changing the configuration of interdigitated electrodes within the SAW resonator and by using a set of tuning electrodes and VO_2 switches. In the first implementation, the VO_2 switches

were integrated over the electrodes and inside the active area of the SAW resonator. Each resonator consists of hundreds of tuning electrodes and for a reliable switching each resonator requires a number of heater elements which results in increased DC power consumption and total size. A second reconfigurable resonator with a modified structure and using a modified in-house fabrication process to include a second electrode layer was proposed to reduce the number of required VO_2 switching elements for an even more compact implementation and ten times reduction in the required DC power consumption. Design, implementation, and measurement results for a 3-pole tunable SAW filter based on the proposed reconfigurable resonators have been presented. The filter's center frequency is tuned from 733 MHz to 713 MHz while the insertion loss was maintained below 2.5 dB. The fabricated SAW resonators and filters also showed acceptable linear and high-power performance characteristics. This is the first time a single-chip implementation of a reconfigurable SAW filter with center frequency tuning and acceptable RF performance using monolithically integrated VO_2 switches is ever reported. The single-chip implementation of the proposed SAW resonators and filters enables the development of future low-cost RF multi-band transceivers with improved performance and functionality.

Acknowledgements

I would like to thank Professor Raafat Mansour for giving me the opportunity to work as a PhD student in his research group. We spent tremendous amount of time discussing various aspects of the research projects together. I am grateful for his patience and interest to advise me from the first day of my PhD program when I was hesitant coping with challenges, to the day of my defense when I was confident about my achievements. He always played a key role to inspire me during this time.

I would like to appreciate Professor Amir Mortazawi, Professor William Wong, Professor Dayan Ban and Professor John Yeow for serving as committee members for my PhD defense, reviewing my thesis and providing valuable feedbacks.

During the six years of PhD program that was the most enjoyable time in my life I had the pleasure of having a great group of collogues in the CIRFE lab. I would like to thank all of them, especially Dr. Junwen Jiang for helping me when I joined the group. I also want to mention my other office mate, Dr. Huayong Jia for the valuable discussions we had together.

I am thankful to our lab manger, Dr. Luis Gutierrez for mentoring me on using various equipment within the CIRFE lab. He was always available when I requested for help. I would like to extend my appreciation to staff members of QNC, especially Dr. Greg Holloway for spending time to train me on lithography equipment and Mr. Rodello Salandanan for friendly talks and his effort to repair the equipment quickly when I had a deadline.

I would like to thank Dr. Aminat Oyiza Suleiman and Prof. Mohamed Chaker from Institut National de la Recherche Scientifique (INRS), Canada, for their support in the VO_2 deposition process.

I would like to acknowledge CMC Microsystem for providing the software tools and Natural Sciences and Engineering Research Council of Canada (NSERC) for their financial support.

Finally, I would like to thank my parents and brothers, especially Siamak for guiding me through this path to start a new chapter in my life by helping me to move to Canada and for all their support.

Table of Contents

List of Figures

List of Tables

List of Abbreviations

RF	Radio Frequency
LTE	Long-Term Evolution
SAW	Surface Acoustic Wave
BAW	Bulk Acoustic Wave
IDT	Interdigital Transducer
IHP	Incredible High Performance
TPoS	Thin Piezoelectric Film on Substrate
CMR	Contour Mode Resonator
MBVD	Modified Butterworth Van-Dyke
MEMS	Microelectromechanical systems
VO_2	Vanadium Dioxide
GeTe	Germanium Telluride
BST	Barium Strontium Titanate
DC	Direct Current
Q	Quality Factor
PCM	Phase Change Material
PECVD	Plasma-enhanced Chemical Vapor Deposition
PLD	Pulsed Laser Deposition
RIE	Reactive-ion Etching

Chapter 1

Introduction

1.1. Motivation

Mobile communication systems have been revolutionized by the demand for higher capacity and bandwidth that is able not only to support ever-increasing global data traffic but also to incorporate new functionalities and features to cellphone devices, such as music and video streaming, GPS navigation, gaming, video calling, etc. The growth in handset shipment was originally driven by the demand for 3G and 4G broadband networks. Long-Term Evolution (LTE) and 5G are the latest cellular standards introduced to increase data transmission throughput utilizing IP packets that enable better usage of the limited radio frequency spectrum. Despite the fact that global transition to 4G technology began just a few years ago, network operators are already starting the transition to the next major evolution – 5G technology.

A significant challenge in the evolution of wireless handsets is the development of multi-band RF frontend modules that enable global coverage with high bandwidth connections. The frontend module is generally defined as everything between the antenna and the digital baseband signal processing unit, which includes all the filters, low-noise amplifiers (LNAs), power amplifiers (PAs), switches, and mixers. Frontend complexity accounts in large part for the need to support any number of frequency bands. For example, a smartphone for international use that supports 2G,

3G and 4G modes must cover up to 16 different bands in addition to coverage for WiFi, Bluetooth, and GPS systems. An increase in the number of supported frequency bands leads to an increase in the number of filters and duplexers within the frontend module. In a current smartphone, there are between 30 and 40 filters for different frequencies, and this number is about to increase up to 50 for future generations of smartphones.

In addition to the increasing number of filters and duplexers within RF frontend modules, the market is also pushing for solutions that include smaller form factors and higher levels of integration while improving performance to achieve more capabilities in less space. This requires the development of new technologies for integrated filters, power amplifiers, and switches either in a single module or in multi-band Power Amplifier Duplexer (PAD) modules. In addition to smaller size, integration will also enable reduced manufacturing costs and increased production yield.

Filters and duplexers are essential parts of RF frontend modules. In a full duplex communication system, where the handset receives and transmits RF signals simultaneously, a duplexer consists of a receiver (Rx) filter and a transmitter (Tx) filter that share the same antenna port, as shown in Figure 1-1. In order to accommodate for a crowded frequency spectrum, these filters are required to be highly selective, with very sharp skirts; they also need to provide substantial out-of-band rejection and isolation between the Tx and Rx bands to prevent interferences, as shown in Figure 1-2. Another important performance characteristic for these filters and duplexers is low insertion loss to maximize the transmitted power and improve the strength of the incoming signal. This will enable the improvement of data throughput and also increase battery lifetime in a handheld device.

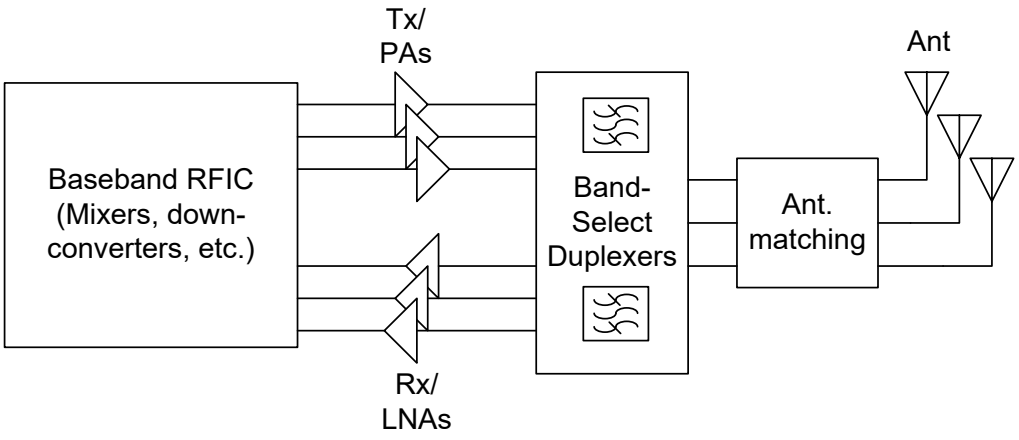

Figure 1-1: Simplified block diagram of full-duplex wireless communication system

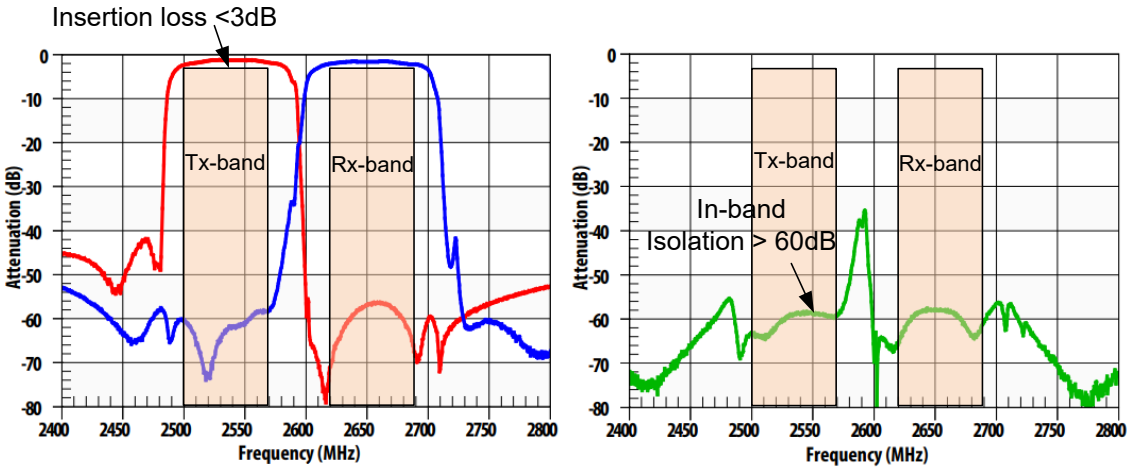

(a) Transmission Response (b) Isolation

Figure 1-2: Frequency response of LTE Band-7 duplexer [1].

Currently, the most widely used technology to implement these high-performance filters and duplexers for commercial wireless applications is the acoustic piezoelectric resonator, realized either in Surface Acoustic Wave (SAW) up to 1.5 GHz or Bulk Acoustic Wave (BAW) technology for higher frequencies up to 6 GHz. An overview of these technologies is presented in [2] and will be discussed in greater detail in Chapter 2. While the conventional SAW and BAW technologies offer exceptional performance in terms of low insertion loss, sharp roll-off and high isolation, stringent requirements for emerging 5G (and beyond) communication standards impose serious

limitations on these technologies. For example, there are limitations for both SAW and BAW technologies in terms of maximum frequency range due to manufacturing issues. Another major requirement for filters and duplexers employed in emerging RF frontends is higher power handling capability, which is limited to below 38 dBm for the current SAW and BAW technologies.

Novel technological developments are required for piezoelectric resonators to address the issues related to higher frequency range (above 6 GHz), higher power handling, better linearity, and higher Q and more importantly tuning to be able to cover multiple frequency bands. New developments are also required to advance integration technologies to provide an entire system-on-a-chip solution for future RF frontends, where the amplifiers, filters and duplexers can be integrated in a compact package.

1.2. Objectives

The objective of this research is to develop, design, analyze, and fabricate highly innovative integrated reconfigurable piezoelectric filters. These filters should possess performance improvements in terms of tuning, power handling and linearity. Such integrated filters also enabled a new class of RF frontends with unprecedented performance and functionality. The realization of this class of filters was possible due to the use of unconventional fabrication processes to manufacture novel piezoelectric resonator structures which are monolithically integrated with novel tuning devices. The stages of research are accomplished as follows:

- **Development, modeling and fabrication of novel piezoelectric resonators:** Contour Mode Resonator (CMR) and Thin-Film Piezoelectric-on-Substrate (TPoS) resonator technologies are investigated to fabricate filters for various frequency bands. These

technologies allow the fabrication of high-performance resonators with different frequencies on the same chip and potentially can be used for ultra-high frequency ranges above 6 GHz. We will demonstrate the application of the commercially available PiezoMUMPs® process [3] for the fabrication of TPoS resonators and filters. Using the proposed fabrication process, it is possible to achieve very high Q while maintaining good power handling capability.

- **Development and modeling of novel switchable multi-band filters using IHP-SAW technology and discrete VO_2 switches:** A switched dual-band filter using piezoelectric IHP-SAW resonators and VO_2 switches is developed that can achieve four different switching states: a) transmission only of the lower channel, b) transmission only of the upper channel, c) transmission of both channels, and d) no transmission. Switching between the four states is implemented using VO_2 switches that are fabricated in-house on separate chips and are integrated within the resonators of the proposed filter structure using hybrid integration with wire bonds.
- **Development of a monolithic integration technique of VO_2 switches with IHP-SAW technology:** A novel monolithic integration approach using an in-house fabrication process at the CIRFE lab at the University of Waterloo to manufacture VO_2 switches and SAW resonators on the same chip is presented. The monolithic integration approach is used to design and implement switched dual-band filters with higher order and improved RF performance by eliminating parasitics that result in from the use of the wire-bonds in hybrid integration approach.
- **Design and implementation of reconfigurable SAW resonators and filters with center frequency tuning:** Novel tunable piezoelectric SAW resonators and filters using

monolithically integrated VO_2 switches to tune the frequency response are presented. Tuning is achieved without compromising important performance characteristics such as the quality factor, power handling, or nonlinear performance. Two different structures are demonstrated for frequency tuning. The first structure is based on using switching elements directly connected to the tuning electrodes within the resonator and employs multiple heater elements. The second improved structure is using a modified fabrication process, which includes a second electrode layer allowing the use of a single switching element per resonator for a compact implementation of higher order tunable filters while reducing the total DC power consumption. A tunable SAW filter is designed using the proposed reconfigurable resonators, which achieves center frequency tuning with good RF performance in terms of insertion loss, power handling, linearity and DC power consumption.

1.3. Thesis Outline

Following the motivations and objectives given in Chapter 1, Chapter 2 presents an overview of several different technologies available to realize piezoelectric resonators, filters and duplexers. This chapter also presents an overview of possible solutions for tunable filters using piezoelectric resonator technology. In Chapter 3, a detailed description of the Contour Mode Resonator (CMR) and Thin-Film Piezoelectric-on-Substrate (TPoS) technologies is given. This is followed by presentation of the simulation results and design of resonators and bandpass filters using TPoS technology and the PiezoMUMPs process. Next part of this chapter is dedicated to measurement results for fabricated resonators and filters over wide temperature range of -196°C to +120°C and also linear and nonlinear characterization of the proposed resonators. Chapter 4 introduces

switched dual-band filters implemented using Vanadium Dioxide (VO_2) switches integrated with SAW resonators and filters. Both hybrid and monolithic integration approaches are presented and the linear, nonlinear and high-power characterization results of the proposed switchable dual-band filters are presented. Chapter 5 discusses the development of novel reconfigurable SAW resonators and filters with tunable center frequency employing VO_2 switches and tuning electrodes. Modeling, simulation and measurement results for the reconfigurable SAW resonators are presented, after which we discuss the design and implementation of filters using these resonators. Finally, a brief summary of contributions of the thesis with an outline of the future research plan are provided in Chapter 6.

Chapter 2

Literature Survey

As the demand for emerging multi-functional wireless devices increases, so does the demand for smaller, higher performance, power efficient and low-cost RF transceivers that can support multiple frequency bands and wireless standards. A transceiver is a wireless device that consists of both a transmitter and a receiver sharing an RF frontend for transmission and reception of radio frequency signals. The main function of a transmitter is to modulate and up-convert baseband data to a selected carrier frequency to achieve high efficiency transmission with a reasonably sized antenna. It also provides signal amplification through the medium, which is free space in the case of wireless communication. The receiver is used to filter, amplify, and down-convert the incoming signal in the presence of unwanted interference and noise. The transceiver configuration mostly used is the super-heterodyne architecture, as shown in Figure 2-1.

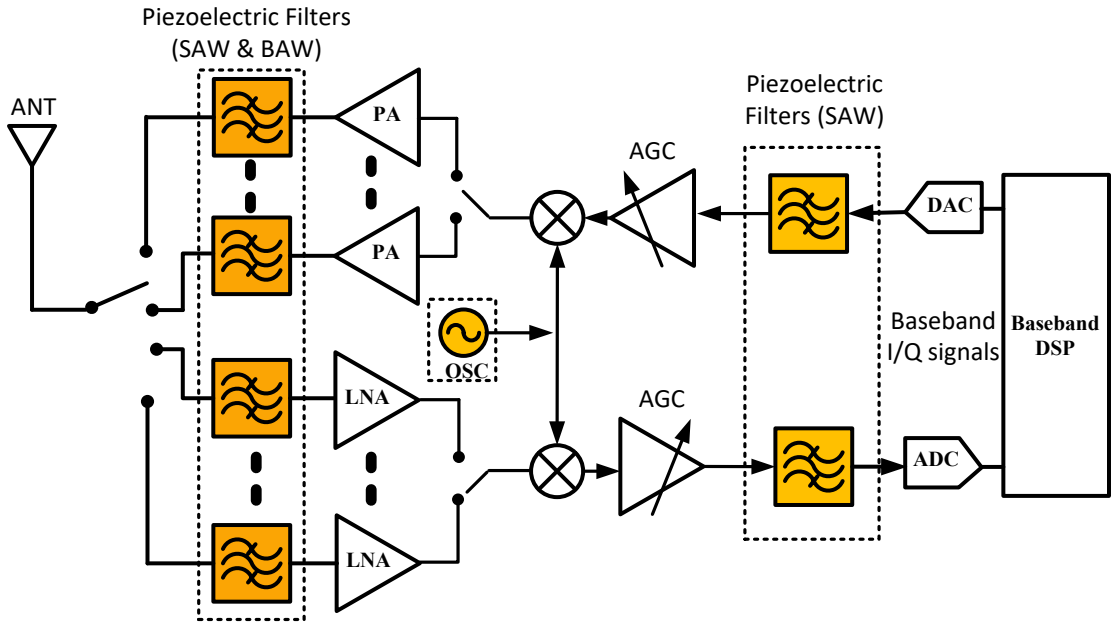

Figure 2-1: Simplified schematic diagram of wireless communication transceiver

The transceiver in Figure 2-1 consists of three main building blocks: frequency generation, amplification, and spectral shaping or frequency filtering. The first two functionalities (frequency generation and amplification) have been successfully implemented using mature integrated circuit (IC) technologies. However, the third functionality (frequency filtering) requires mechanically resonating components such as quartz crystals, Surface Acoustic Wave (SAW), and Bulk Acoustic Wave (BAW) with high quality factors that currently cannot be integrated with conventional transistor technologies on a single chip. Although filter banks and multiplexers implemented with SAW and BAW technologies can fulfill all the requirements for current wireless communication systems in terms of insertion loss, bandwidth, achievable out-of-band rejection and isolation, they still suffer from limitations such as miniaturization, power handling, maximum achievable frequency range and nonlinearities for future demanding standards, including 5G and beyond.

Efforts have been focused on developing alternative piezoelectric resonant structures and technologies to address these issues, which will be discussed in this chapter.

2.1 Micro-Mechanical Resonators for RF Frontend Applications

The concept of micro-mechanical resonators was first introduced in 1965 by H.C. Nathanson through the implementation of a resonant gate transistor structure as a frequency-selective device [4]. The device was fabricated using a fabrication process similar to current micro-electro-mechanical systems (MEMS) processing and consisted of a resonating cantilever (gate electrode), an input and output drive, and sense electrodes, as shown in Figure 2-2. In this case, the energy coupling from electrical to mechanical domain and vice versa is achieved using electrostatic transduction. Extensive research has been conducted on MEMS resonant structures based on electrostatic transduction, and we will discuss some of these structures in this chapter.

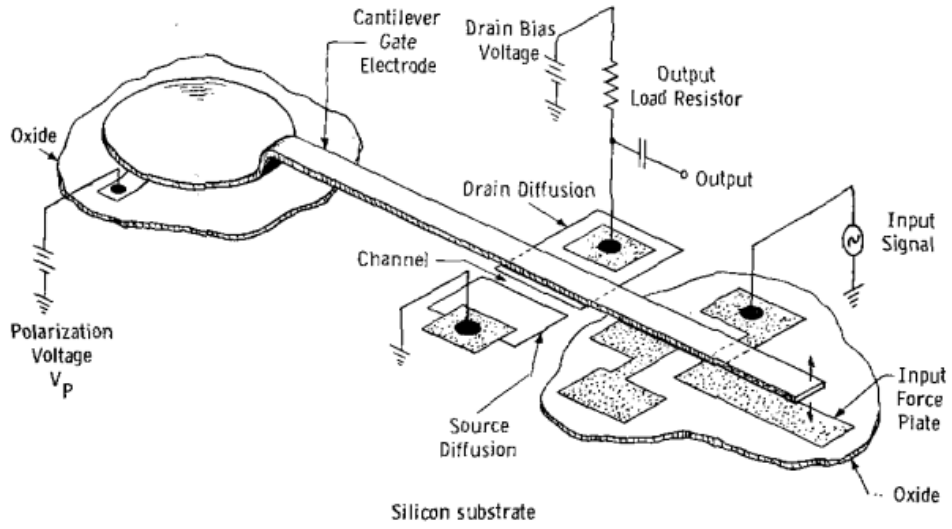

Figure 2-2: Resonant gate transistor device [4]

The other energy conversion or transduction mechanisim used in micro-mechanical resonators is the piezoelectric effect, where the electrical signal is converted to acoustic waves propagating in a solid medium. The acoustic wave approach has, for a long time, been utilized in RF electronics to implement various building blocks, such as local oscilators, filters, and delay lines. These devices are based on transduction between electric signals and acoustic waves, with part of the signal processing being performed in the mechanical domain. Acoustic wave devices benefit from i) low mechanical loss and attenuation of acoustic waves through the crystalline material and ii) lower acoustic wave velocity in the medium compared to electromagnetic waves. The low mechanical losses enable resonators to be fabricated with a high quality factor (Q values in excess of thousands), which is essential for implementing low loss filters using SAW or BAW technologies. The mechanical wave velocity of acoustic devices (in the range of 5000 m/sec) is orders of magnitude smaller compared to electromagnetic wave velocity, which enables the implementation of RF devices of a much smaller size compared to conventional RF transmission lines or cavities. Recent developments in MEMS processing have opened up even more possibilities for acoustic devices in terms of miniaturization and integration with other electronic circuitry, which is discussed in this chapter.

2.2 Surface Acoustic Wave (SAW) Resonators

SAW is the most mature and low cost technology in use since the introduction of mobile phones. In a SAW resonator, as shown in Figure 2-3, surface acoustic waves are generated using interdigital transducers (IDT), which are periodic arrays of metal fingers deposited over a piezoelectric substrate material. The application of an RF signal, and hence an electric field between the fingers, excites an acoustic wave that horizontally travels over the surface of the substrate perpendicular to the IDT fingers. Conventional piezoelectric materials used as a substrate

include quartz, lithium tantalite ($LiTaO_3$) or lithium niobate ($LiNbO_3$). As shown in Figure 2-3, a SAW resonator consists of input and output IDT electrodes as well as gratings that are used to reflect back the acoustic waves from both sides in order to reduce energy loss and improve Q. The IDT finger width and spacing is usually equal to a quarter wavelength (λ/4), so the interdigital electrode and grating period is equal to half a wavelength (λ/2).

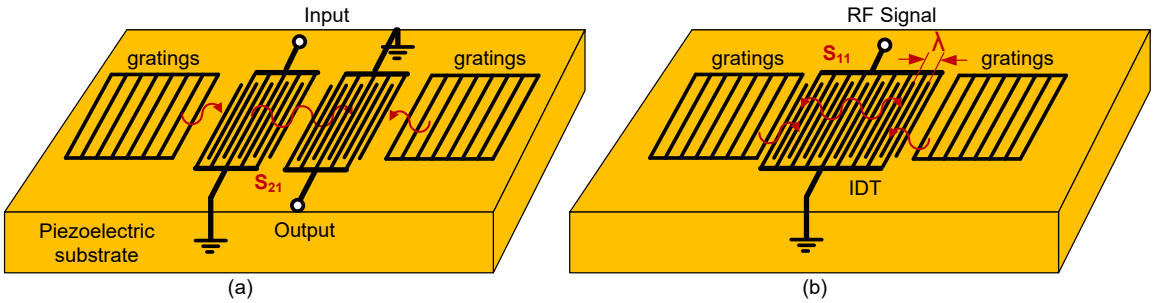

Figure 2-3: Structure of (a) two-port and (b) one-port SAW resonators

SAW resonators are widely used in 2G and 3G frontends, duplexers, and receiver filters at frequencies below 2 GHz. SAW filters achieve low insertion loss, good rejection and wide bandwidth and are only tiny fractions of the size of traditional cavity and ceramic filters. They also benefit from low fabrication cost due to wafer-level processing that only requires a single deposition and patterning of IDT metal electrodes. In addition, SAW technology allows the fabrication of filters for different frequency bands on the same wafer and chip due to the fact that the frequency is tuned only by adjusting the spacing between the IDT fingers.

The most severe limitations of SAW resonators at higher frequencies are the decrease in the quality factor and the size of the electrodes starting to approach sub-micron scale. At such small sizes, the fabrication of SAW devices above 2 GHz requires special photolithography techniques such as electron-beam lithography. Other limitations of SAW technology include temperature

sensitivity, electrostatic discharge and power handling capability when the IDT finger width and spacing shrink to sub-micron dimensions. SAW devices are also inherently limited in terms of integration with other CMOS electronic circuitry due to the thick piezoelectric substrate material required for device operation that makes it incompatible with standard microelectronic manufacturing using a Silicon substrate.

Numerous research studies have addressed the limitations in SAW technology, such as higher frequency operation, power handling, and reducing temperature drift and sensitivity. High frequency SAW resonators operating above 10 GHz were proposed in [5], where an operational frequency range of 10-14 GHz was achieved using e-beam lithography to produce nanometer-scale IDT fingers with a width and spacing of 200 nm over an Aluminum Nitride (AlN)/Diamond composite substrate material.

Temperature-compensated SAW (TCSAW) filters and resonators with high Q factors were presented in [6], [7]. To achieve a lower temperature coefficient of frequency (TCF), a heavy metal electrode with a planar silicon dioxide (SiO_2) overcoat was used over the piezoelectric $LiNbO_3$ substrate, as shown in Figure 2-4. The combination of negative TCF for the piezoelectric substrate material and positive TCF for the overcoat SiO_2 layer resulted in near-zero TCF for the overall stack. Adding a SiO_2 layer caused coupling of the acoustic energy to this layer, which resulted in lowering the Q and coupling coefficient of the resonator. This indicates that there is a trade-off between temperature compensation, bandwidth, and quality factor.

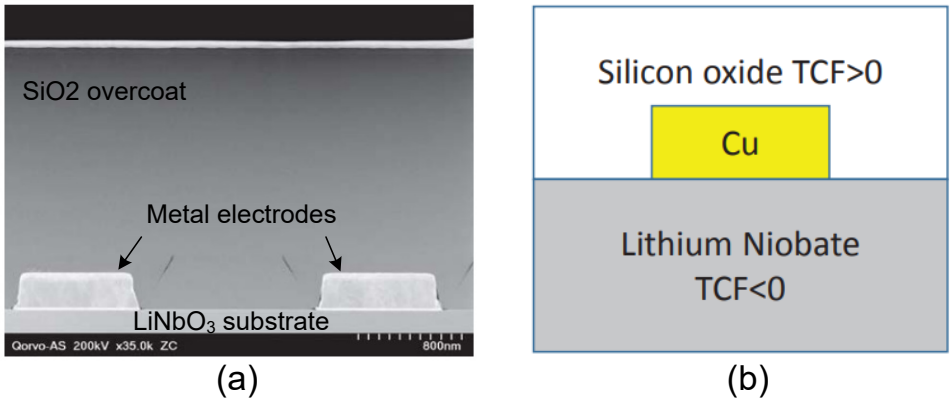

Figure 2-4: Structure of temperature-compensated SAW (TCSAW) resonator [6].

2.3 Balk Acoustic Wave (BAW) Resonators

The shortcomings of SAW technology, especially for higher frequencies, can be addressed using Balk Acoustic Wave (BAW) technology. In a BAW device, the acoustic wave propagates in a vertical direction prependicular to the substrate. As shown in Figure 2-5, a thin film piezoelectric layer is deposited between top and bottom metal electrodes. The thickness extension (TE) resonance frequency, which is the main acoustic mode for BAW devices, is determined by the thickness of the piezo layer ($t = \lambda/2$) and the mass of the electrodes.

There are two different approaches for reducing mechanical acoustic loss through the substrate in BAW devices. In a Thin-Film Piezoelectric Resonator (FBAR) device, as shown in Figure 2-5 (a), this is achieved by creating an air-cavity under the resonator. The air cavity creates an open circuit mechanical impedance which completely eliminates the propagation of acoustic waves in the vertical direction and into the substrate. In an alternative embodiment, called a Solidly Mounted Resonator (SMR) structure, a Bragg reflector stack is used to reflect the acoustic waves back into the resonator. The Bragg reflector is a periodic stack that consists of alternating materials with high and low mechanical acoustic impedance, such as Tungsten and SiO_2.

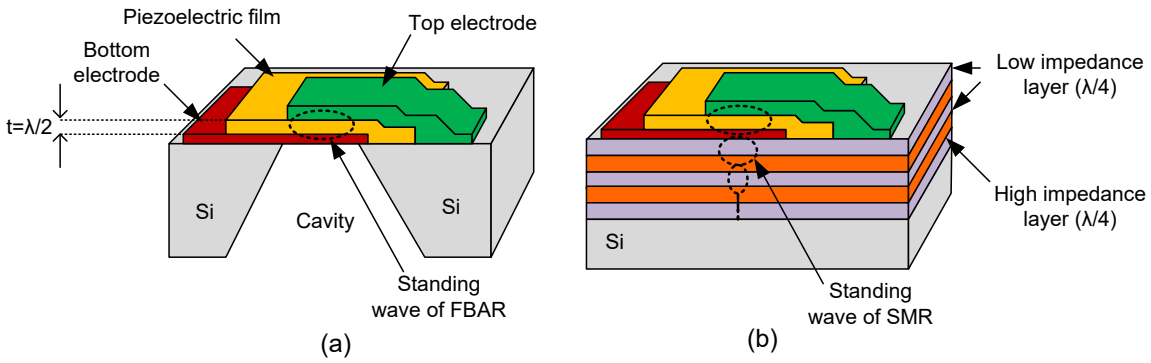

Figure 2-5: Structure of BAW resonators (a) FBAR and (b) SMR.

The mechanical energy is well contained in BAW devices compared to SAW technology. Hence, BAW devices offer superior performance in terms of higher Q factors for the GHz frequency range. Q values of > 2000 at 2 GHz represent the state-of-art for FBARs and SMRs [2]. Unlike SAW resonators, BAW devices do not have narrow metal fingers or electrode spacing. Power handling is mainly limited by the maximum temperature that the material present in the BAW stack can handle, which is typically orders of magnitude higher than in SAW technology. Power handling for SMR resonators is even better compared to FBAR resonators due to better thermal conduction through the Bragg reflector and silicon substrate compared to FBAR resonators, where the piezoelectric stack is floating over an air cavity.

BAW resonators, in particular SMR, also have much better temperature sensitivity and drift compared to SAW technology. Better TCF for SMR resonators is achieved by utilizing the Bragg reflector as a temperature compensation layer for the main piezoelectric stack. The most important advantage of BAW technology is that frequencies up to 6 GHz can be achieved without any major manufacturing issues. The thickness of the piezoelectric layer and the area of resonators scale with

a factor of (1/f) and ($1/f^2$), respectively, which makes this technology favorable for higher frequencies in terms of area savings.

One of the main limitations of BAW technology is the higher manufacturing cost compared to SAW technology. The higher cost is due to more complex manufacturing and extra processing steps required for deposition and patterning of the layers present in the piezo stack and Bragg reflector. Another disadvantage of BAW technology compared to SAW is that BAW cannot host resonators and filters with different frequency bands on the same wafer, as the resonance frequency is mainly limited by the thickness of the deposited piezoelectric layer, which is the same everywhere on the wafer. Although FBAR/SMR resonators offer advantages that are unmatched by SAW technology, for frequencies above 5 GHz, they suffer from performance issues such as power handling and manufacturability caused by ultra-thin layers of piezoelectric material required for higher frequency stacks, lower Q, and smaller bandwidth. Recent scientific studies have been conducted to address these issues.

Aluminum Nitride (AlN) piezoelectric material growth using a metal organic chemical vapor deposition (MOCVD) technique instead of conventional physical vapor deposition (PVD) is proposed in [8] to improve Q-values and power handling at 3.7 GHz. Higher Q and better power handling is achieved by using a single crystalline AlN layer grown on Silicon Carbide (Si-C) substrate instead of poly-crystalline material employed in conventional FBAR and SMR devices. FBAR resonators for millimeter-wave applications with ultra-thin (~100 nm) layers of MOCVD deposited piezoelectric AlN layer is presented in [9]. A resonant frequency higher than 7 GHz was achieved with a Q value around 300. BAW resonators and filters are inherently limited in terms of achievable bandwidth. This is due to the limited value of intrinsic piezoelectric coupling coefficient for the Aluminum Nitride (AlN) material that is traditionally used in BAW technology.

Significant improvement in piezoelectricity was reported in [10] by applying AlN films heavily doped with Scandium (Sc). A five-fold increase in thickness extensional piezoelectric constant (d_{33}) value was observed compared to pure AlN by using $Sc_{0.43}Al_{0.57}N$ alloy film.

2.4 Lamb Wave and Contour Mode Resonators (CMR)

Despite the dominance of BAW devices in the current wireless market, they suffer from a major limitation, as their resonance frequency is set by the thickness of the piezeoelectric film. For this reason, to obtain a yield suitable for mass production, the thickness of the piezoelectric film must be accurately controlled. In addition, using the current fabrication processes and structures for BAW resonators, it is practcally impossible to fabricate resonators and filters that operate at different frequency bands using one process run on the same wafer. This places a barrier to applying BAW technology for single-chip implementation of multi-band RF frontends.

To address this issue, Yantchev et al. [11] and Piazza et al. [12] proposed the concept of thin-film piezoelectric Lamb Wave Resonators or Contour Mode Resonators (CMR) with an in-plane mode of vibration. CMR technology combines the major advantages of BAW and SAW technologies. Higher Q values and higher frequency bands similar to BAW can be achieved, while the resonance frequency is determined by the lithography defined lateral dimensions similar to SAW resonators.

AlN CMR resonators with plate and ring shaped structures, as shown in Figure 2-6, were proposed in [12]. These resonators achieve Q values as high as 4300 at frequencies up to 230 MHz. The resonators consist of an AlN layer between bottom Pt and top Al electrodes, where the vertical electric field applied on the piezo material creates in-plane dilation of the structure through the d_{31} piezoelectric coefficient and excites either length extension or width extension acoustic modes, as

shown in Figure 2-6 (c-d), depending on the excitation frequency. The lateral dimensions of the plate (L and W) determine the resonance frequency of the CMR resonator in Figure 2-6 (a), and the thickness of the AlN layer has only a second order effect on resonance frequency.

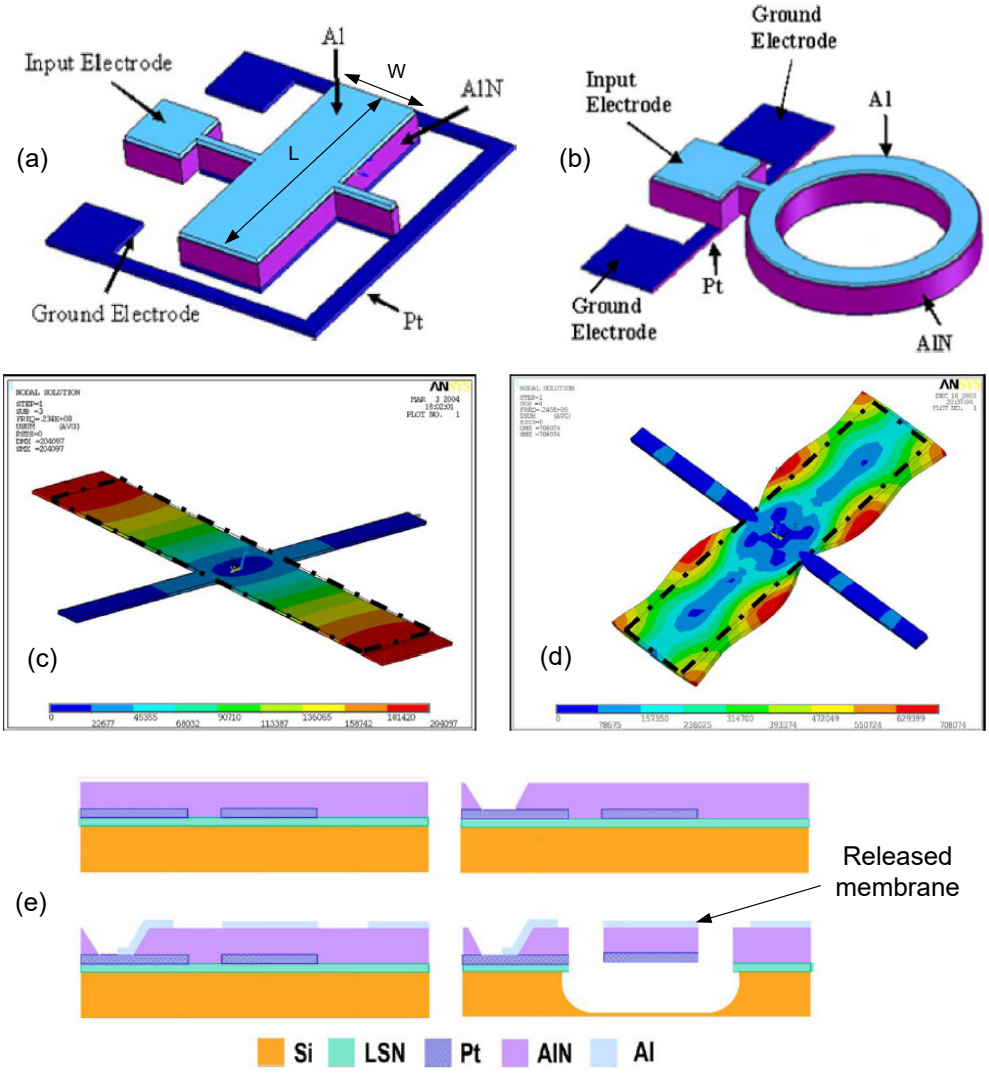

Figure 2-6: Schematic diagram of AlN CMR resonator with (a) rectangle and (b) ring shapes, fundamental mode shapes for (c) length extension and (d) width extension in rectangular CMR resonator, (e) fabrication process of CMR resonator [12].

Similar to FBAR resonators, acoustic energy loss through the substrate is eliminated by using an air cavity under the released membrane, as shown in Figure 2-6. Therefore, the mechanical losses

are only limited to anchor losses and losses within the piezoelectric layer itself. This results in high Q values comparable to FBAR technology.

A new CMR resonator based on selective excitation of higher order plate modes was proposed in [13]. Two different excitation schemes based on thickness field excitation (TFE) and lateral field excitation (LFE) were used to excite adjacent strips of rectangular plates out of phase with respect to each other, as shown in Figure 2-7. These resonators exhibit resonance frequencies ranging from 200 MHz to 800 MHz, with Q values of a few thousands (1000 to 2500). Electrode periodicity and plate absolute dimensions set the resonance frequency of these devices. Furthermore, the number of electrode strips can be modified to adjust the motional resistance and impedance of the resonator.

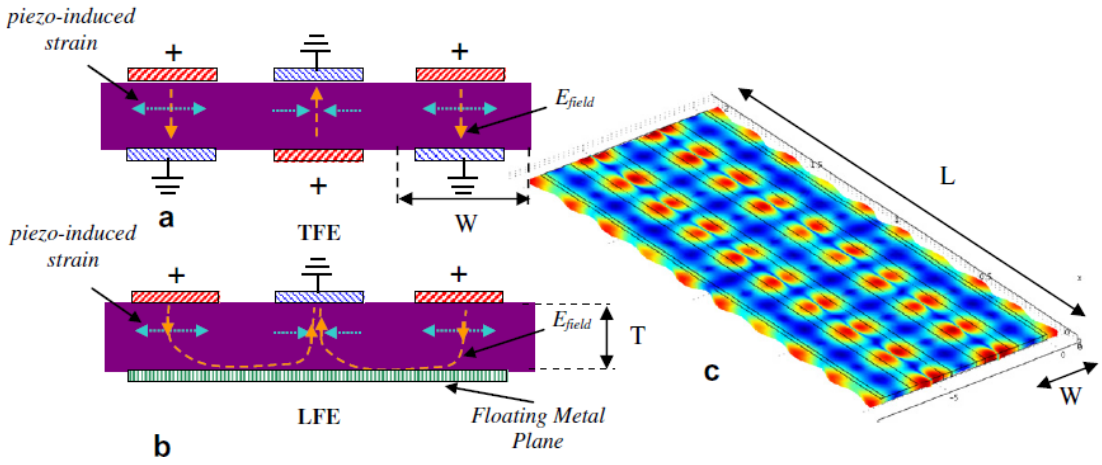

Figure 2-7: CMR resonator with higher order plate mode excitation mode [13].

AlN CMR resonators with resonance frequencies between 5 GHz to 10 GHz and Q values from 400 to 700 were reported in [14]. Resonators with different center frequencies were fabricated on the same chip by adjusting the lateral dimensions of resonators and using nanometer scale electrode strips (500 to 1000 nm wide). Figure 2-8 (a) shows an SEM image of a fabricated

resonator with 100 nm-thick metal electrodes patterned using e-beam lithography and a 250 nm thick AlN piezoelectric layer directly grown on top of a high resistivity silicon substrate. The resonator is released by isotropic etching of the silicon substrate using XeF_2. It consists of (n = 99) electrodes and has a plate area of (17 × 49.5 µm). The measured admittance curve of an 8.5 GHz CMR resonator is shown in Figure 2-8 (b), where a Q value of 414 was achieved.

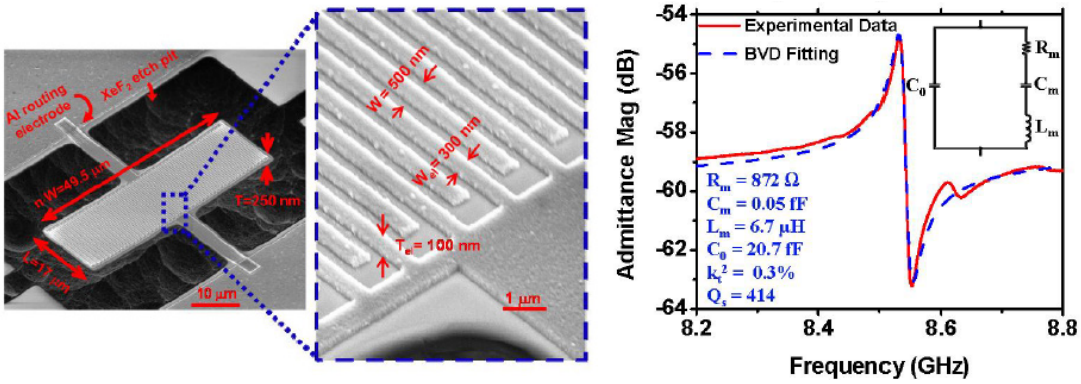

Figure 2-8: AlN CMR resonators for 5GHz to 10GHz frequency range [14].

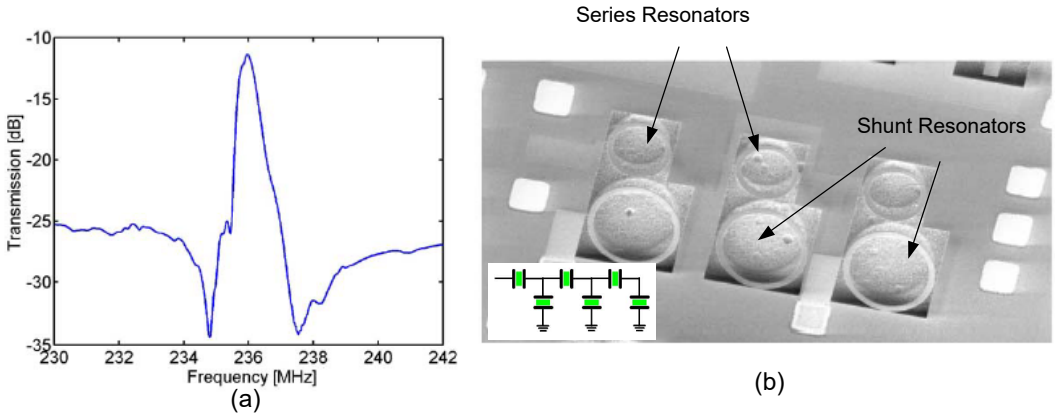

Figure 2-9: Frequency response and SEM image of 236MHz ladder filter using ring-shaped AlN CMR resonators [15].

Bandpass filters utilizing AlN CMR resonators were presented in [15]. The filter was fabricated using ring shaped CMR resonators of different sizes for series and shunt resonators in a ladder configuration, as shown in Figure 2-9.

2.5 Thin-Film Piezoelectric on Substrate (TPoS) Resonators

A new class of piezoelectric resonators, called thin-film piezoelectric-on-substrate (TPoS), was introduced by Abdolvand et al. [16]. These devices benefit from a high piezoelectric coupling coefficient and transduction of piezoelectric materials such as AlN and superior acoustic properties (low acoustic loss and high acoustic velocity) of substrates such as single crystalline Silicon or Diamond. Using this technology, it is possible to further increase frequency range while maintaining a higher Q value. The higher Q and resonance frequency is achieved by employing single crystalline substrate material as a medium for acoustic wave propagation instead of the piezoelectric layer itself. The thin-film piezoelectric material in this case is only used to excite the acoustic waves into the single crystalline substrate material.

A schematic diagram of a TPoS two-port resonator is shown in Figure 2-10. The resonant structure in this case consists of a stack of top and bottom metal electrodes, a piezoelectric layer, and a relatively thick single crystalline silicon substrate. The resonance frequency is determined by the lateral dimensions of electrodes, similar to CMR devices, and the acoustic material properties of the single crystalline substrate material.

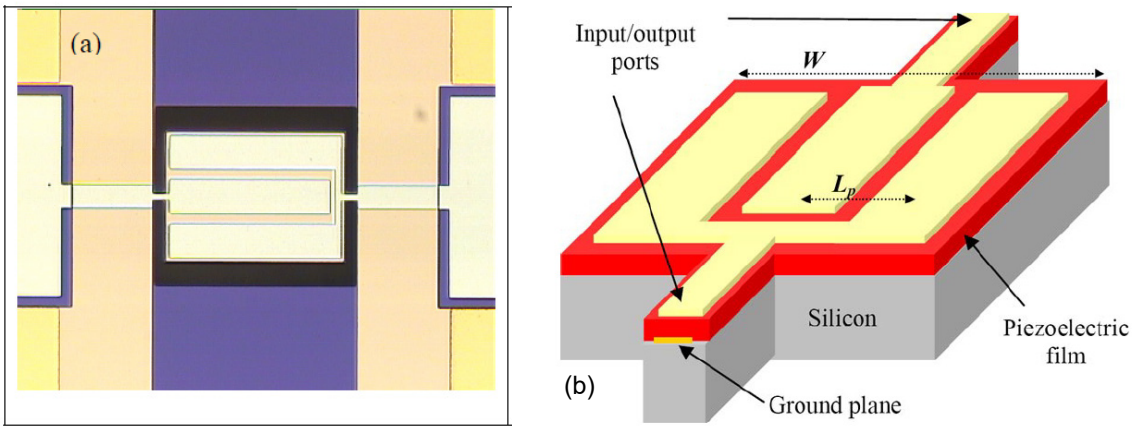

Figure 2-10: (a) Optical photo and schematic diagram of TPoS resonator [17].

Figure 2-11 shows a measured S-parameter response and SEM images of filters using TPoS resonators fabricated on a 5 um thick SOI silicon substrate. Filters with center frequencies ranging from 300 MHz to 3.5 GHz have been demonstrated within a single chip using the same technology.

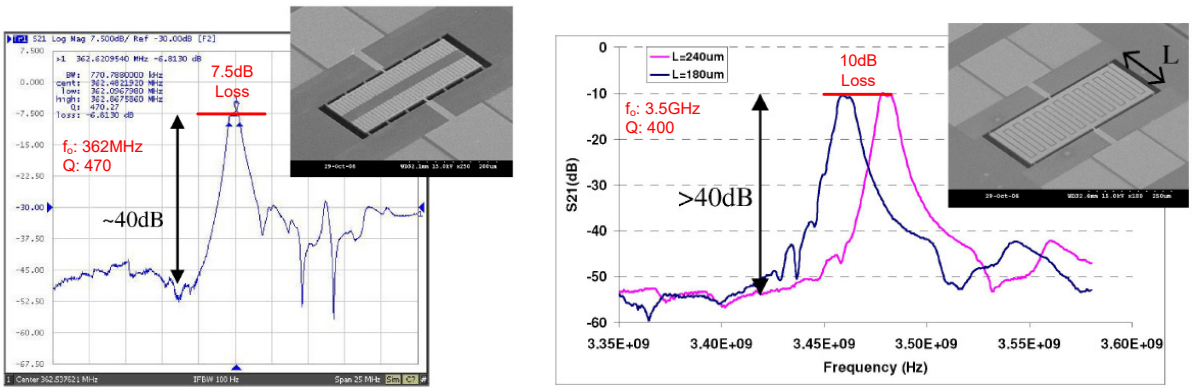

Figure 2-11: S-parameter response and SEM image of (a) 360MHz and (b) 3.5GHz thickness mode TPoS filters [16].

2.6 Electrostatic Resonators

Electrostatic or capacitively-transduced resonators were introduced by R.T. Howe in [18] where a capacitively actuated resonant microbridge was used for vapor sensing. In electrostatic resonators, as shown in Figure 2-12 (a), an electrostatic transducer with sub-micron air gap is used to convert electrical signals to mechanical vibrations in the resonant body, as opposed to piezoelectric resonators, where acoustic waves are used.

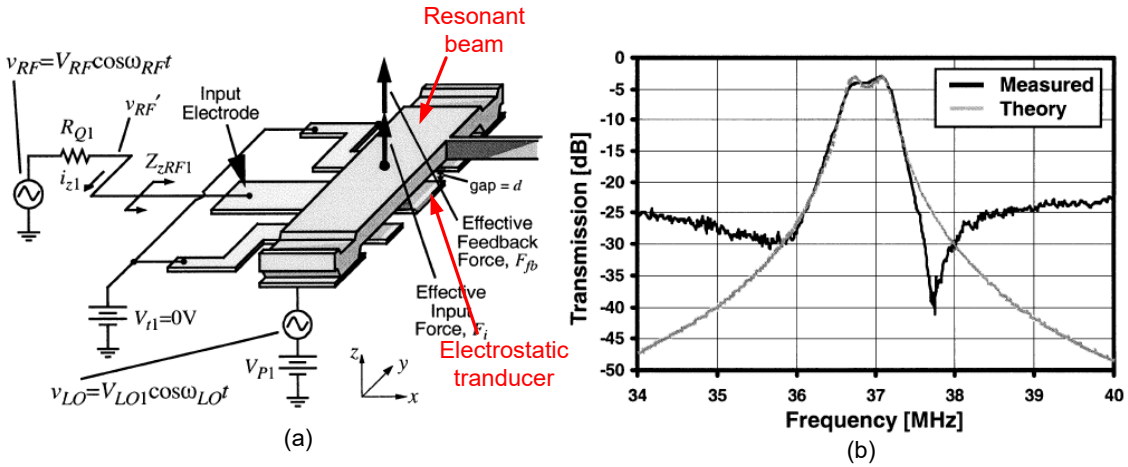

Figure 2-12: (a) Schematic diagram of electrostatic micro-mechanical resonator and (b) S-parameter response of 37MHz bandpass filter [19].

The resonance frequency is determined by the mechanical resonance frequency of the vibrating beam or membrane, which is controlled by geometrical parameters such as width, length and thickness of the resonant body as well as material properties such as stiffness and density. Advances in surface micromachining has enabled the fabrication of micrometer-scale structures with resonance frequencies in the range of 30 MHz to 300 MHz that achieve Q values in the order of a few tens of thousands in a vacuum or air environment [19]. Lateral contour mode disk resonators vibrating at higher order modes were proposed in [20] and [21] to increase the frequency

of operation to the GHz range while maintaining a higher Q. The radial contour mode resonator shown in Figure 2-13 demonstrated a resonance frequency up to 1.156 GHz, with a measured Q close to 3000 in both vacuum and air [21].

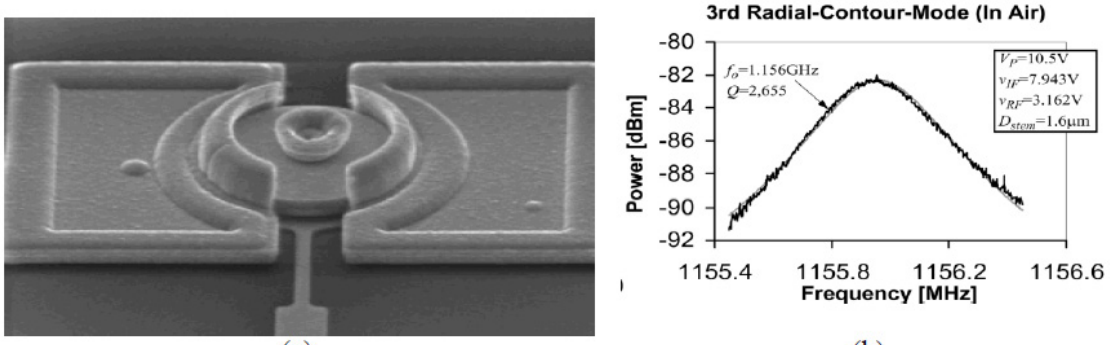

Figure 2-13: Radial contour mode micromechanical resonator [21].

Dielectric electrostatic transduction, instead of air-gap capacitive transduction used in conventional electrostatic resonators, was reported in [22] to achieve higher resonance frequency. Dielectric transduction was implemented using dielectric films embedded in a single crystalline silicon resonant body, as shown in Figure 2-14. A resonance frequency of 4.5 GHz with a quality factor of over 11,000 was achieved using the proposed structure.

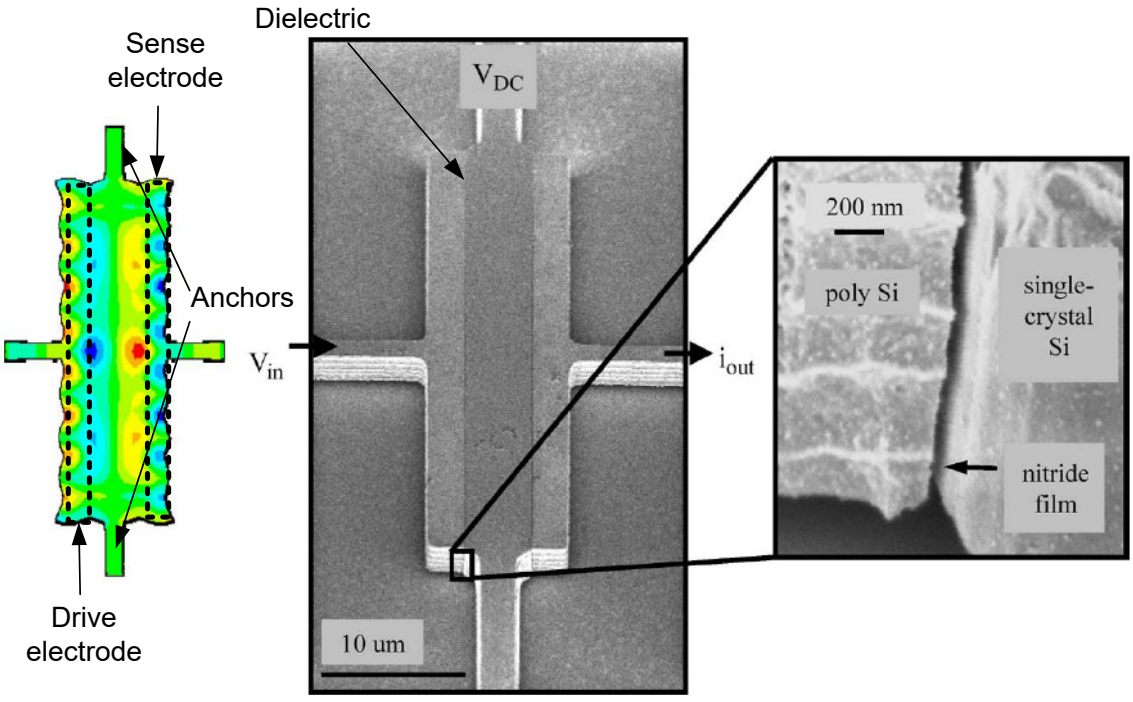

Figure 2-14: Bulk longitudinal mode resonator with dielectric transduction [22].

Despite the high Q and wide frequency range achieved for electrostatic micromechanical resonators, they suffer from a major disadvantage. The motional resistance of these resonators is too high (>1kΩ), which makes it difficult to match them with the standard 50 Ω impedance of today's RF components. For this reason, the application of these resonators was mainly limited to sensors and oscillators. Research towards lowering the motional impedance of these devices is required if this technology is to be used for RF filter applications.

2.7 Tunable Piezoelectric Resonators and Filters

To address the demand for ever-increasing data traffic in wireless communication, new standards and many more frequency bands are expected to be employed in the near future. This will require the addition of new RF filters and duplexers for each new frequency band, resulting in a more complex and expensive RF frontend module. Miniaturization will be mandatory to fit such a large number of filters into the limited space that is assigned for the RF frontend module. A tunable filter solution can address this major issue by enabling the use of a single tunable filter that can cover multiple frequency bands. However, this tunable filter is still required to meet the critical performance requirements, such as low insertion loss, good power handling and nonlinearities, while still maintaining a compact size. Several research studies have been conducted in recent years to find a tunable filter solution that is applicable for commercial use in wireless communication, but there is currently no known tunable RF filter technology able to match the performance of conventional BAW and SAW filters.

Tunable filters using transmission lines and MEMS tuning elements such as varactors and inductors have been proposed. These demonstrate a sufficient tuning range [23] - [25] but the circuits still suffer from low Q values (<300) and they are not as compact as the conventional BAW or SAW filters. An RF MEMS tunable bandpass filter with a tuning range from 1.5 to 2.5 GHz was reported in [23]. The filter consists of corrugated coupled transmission lines and a 3-bit MEMS varactor, as shown in Figure 2-15. This filter achieves an insertion loss below 2 dB with a narrow bandwidth (72 MHz), which is suitable for wireless applications. However, the total footprint of the filter, including transmission lines and tuning elements, is almost four times the size of current BAW filters for the same frequency band. The other limitation of MEMS tunable filters is their reliability and lower yield for mass production in wireless market.

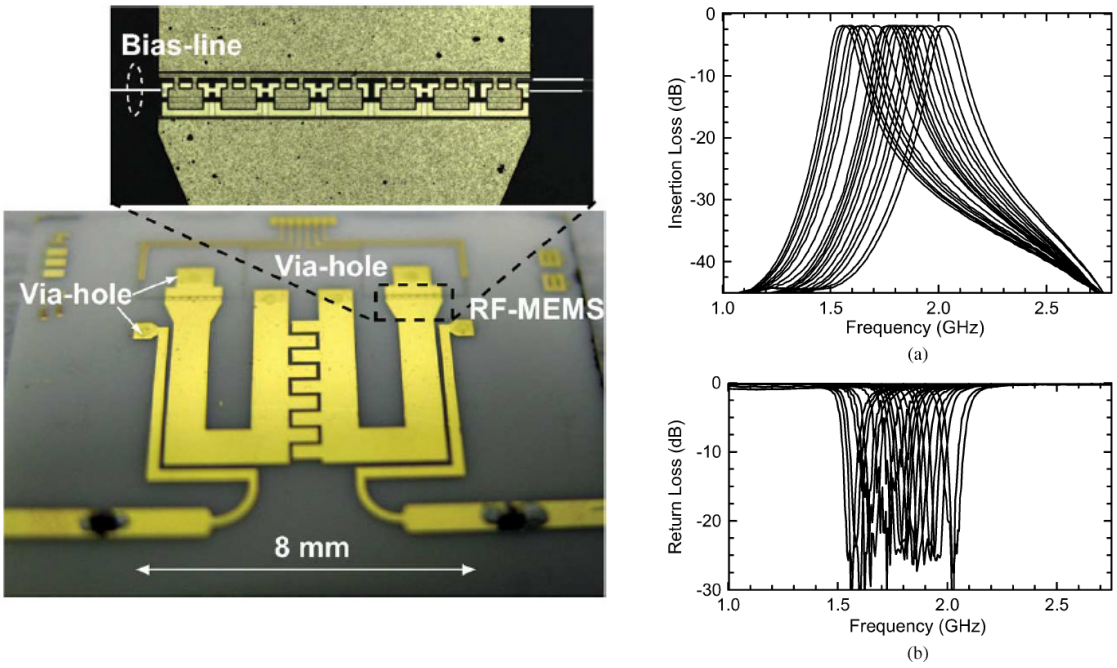

Figure 2-15: Tunable RF MEMS filter for wireless band [23].

Tunable filters using active circuits are also proposed for wireless applications in [26] - [28]. Although these filters have a very compact footprint implemented by utilizing state-of-the-art integrated circuit technologies and can provide sufficient insertion loss using active loss compensation circuits, they suffer from nonlinearity issues and low power handling for current wireless standards.

In this research, we mainly focus on tunable filter solutions using piezoelectric SAW resonators. The conventional BAW and SAW technologies can provide key performance characteristics, such as low insertion loss, high out-of-band rejection and isolation, good temperature stability, power handling, robustness against electrostatic discharge, good nonlinearity (intermodulation and harmonics), small size, light weight, and low manufacturing cost. A tunable

BAW and SAW solution which could maintain these performance characteristics would constitute a technological breakthrough in wireless communications.

The possibility of developing tunable SAW and BAW filters using variable capacitors was discussed in [29]. Tuning was achieved by connecting variable capacitors in parallel and/or series with SAW resonators in a ladder filter configuration, as shown in Figure 2-16. The proposed configurations consist of variable capacitors C_s and C_p connected in parallel and series with series resonators Z_s and shunt resonators Z_p. It is possible to tune the lower and upper edges of the passband as well as the center frequency within a certain range by adjusting the varactors. The figure also shows that the quality factor of the variable capacitors does not have a significant impact on the filter insertion loss for the configuration in Figure 2-16 (a).

An optical image and S-parameter response of a proposed SAW filter is shown in Figure 2-17. For this implementation of the proposed tunable filter, fixed capacitors are used instead of variable capacitors. Two different designs with the same filter configurations and SAW resonators are used. The only difference between the two filters is in the capacitance value of tuning elements (not an actual tunable filter with tunable capacitors). As shown in the S-parameter response in Figure 2-17, a tuning range of around 20 MHz (2%) was achieved.

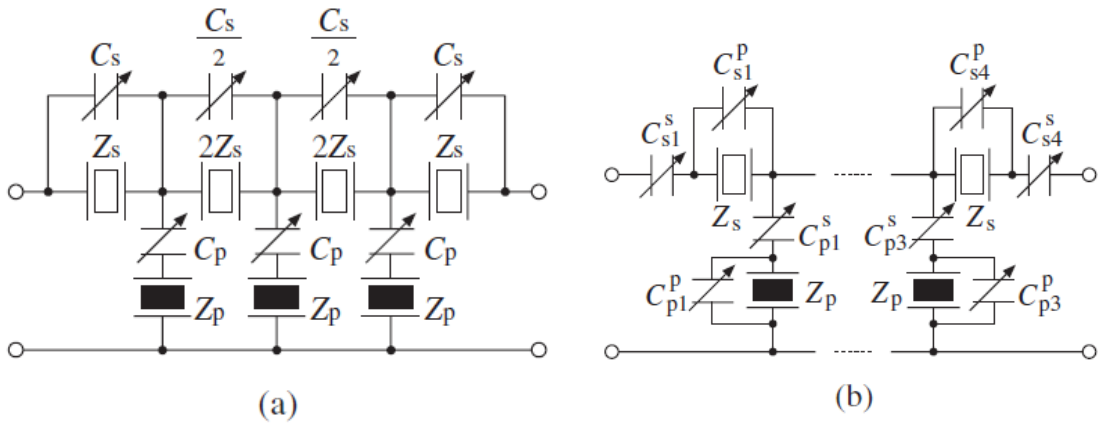

Figure 2-16: Tunable SAW/BAW filters with variable capacitors

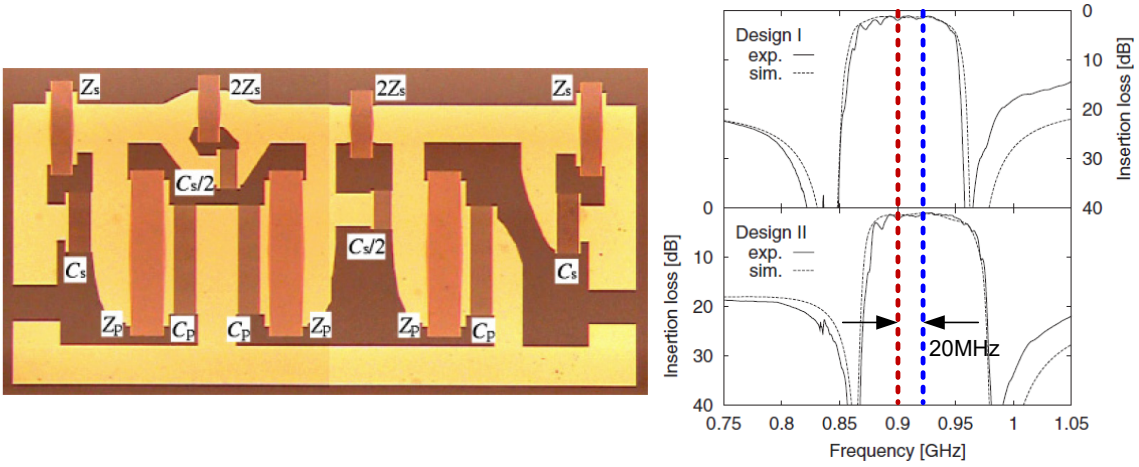

Figure 2-17: Image and S-parameter response of SAW filter with tuning elements [29]

Another circuit configuration of tunable SAW filters which allows for the adjustment of the bandwidth and center frequency for a wider range was proposed in [30]. The proposed circuit in Figure 2-18 consists of two pairs of SAW resonators and varactors in both series and parallel arms. Tunable filters with both adjustable bandwidth and center frequency were designed, as depicted in Figure 2-18 (a) and (b), respectively. Although filter bandwidth can be continuously adjusted for more than four times, as shown in Figure 2-18 (c), the insertion loss of the filter increases with decreased bandwidth.

Simulated S-parameters for a tunable SAW filter with adjustable center frequency are also presented in Figure 2-18 (d). To implement these SAW tunable filters, a transfer process to integrate barium strontium titanate (BST) varactors with SAW devices on the same substrate was proposed in [31]. The BST varactors were fabricated on a sapphire substrate and then transferred to a Lithium Niobate substrate used to fabricate SAW resonators. Figure 2-19 shows an optical image of the fabricated tunable SAW filter with integrated BST varactors. As shown in the S-parameter response of the tunable filter in Figure 2-19 (c), the bandwidth was tuned between 3.25 MHz and 6.25 MHz, while the center frequency was constant at around 1 GHz. The insertion loss of the proposed filter was degraded due to the low Q value of the BST varactors used as tuning elements.

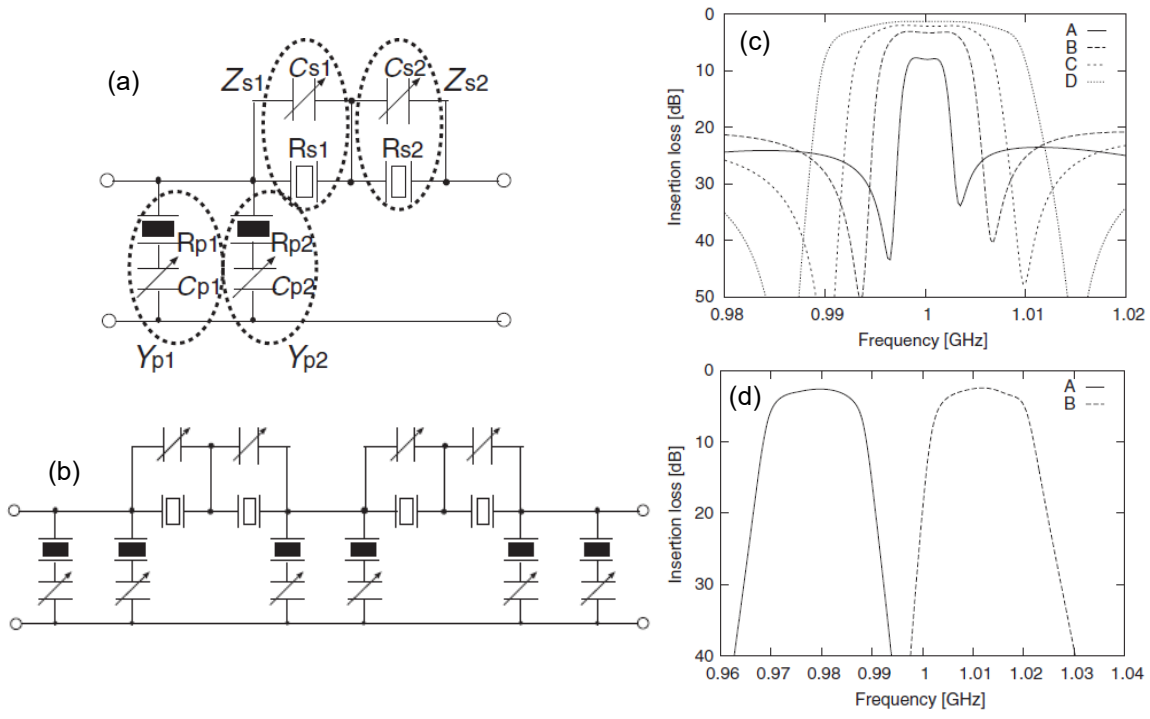

Figure 2-18: (a) Circuit topology for tuning elements and (b) tunable SAW filter (c, d) simulated S-parameters of tunable SAW filter with a wider tuning range [30].

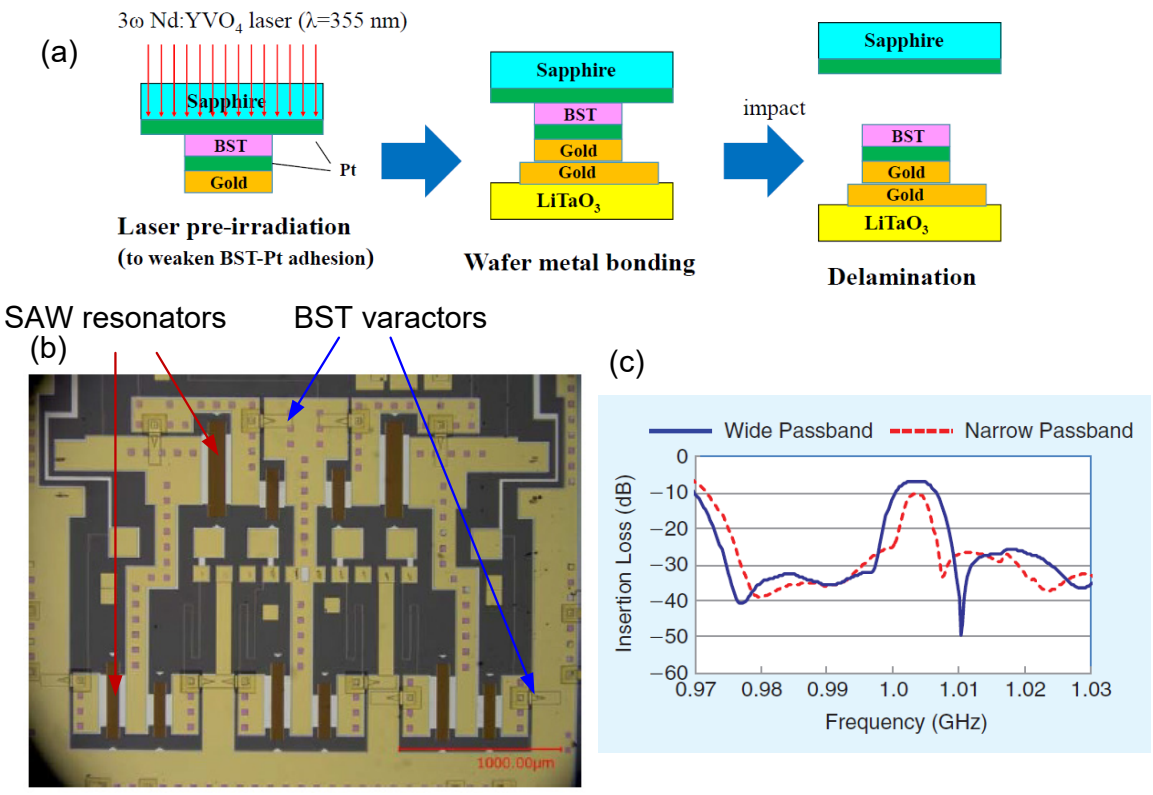

Figure 2-19: (a) Transfer process to integrate BST varactors, (b) optical image and (c) S-parameter response of fabricated tunable filter [31].

Another technique to implement tunable SAW filters, by combining a wideband bandpass filter and band-reject filters was presented in [32]. This type of tunable filter is less affected by reductions in the insertion loss due to the lower Q values of the tunable capacitors. A T-type ladder filter with an ultra-wideband response using SH0 plate mode resonators was designed. The S-parameter response of the initial wideband bandpass filter is shown in red in Figure 2-20 (a) and (b). Two different band-reject filters were also fabricated using series or parallel resonators, as depicted in the figure. A band-reject filter with a wide rejection band can be obtained when several resonators with slightly different frequencies are connected in parallel or series. For example, Figure 2-20 (a) shows the frequency response of a band-reject filter consisting of four resonators with 30 MHz frequency spacing connected in parallel. A tunable bandpass filter with a smaller

bandwidth was obtained by combining the ultra-wideband bandpass filter with the two band-reject filters. Each band-reject filter can be tuned by using tuning elements in series or in parallel with SAW resonators, as shown in the figure. Since the varactors are used to tune only the band-reject filters, the Q value of these varactors is not expected to affect the insertion loss of the overall bandpass filter.

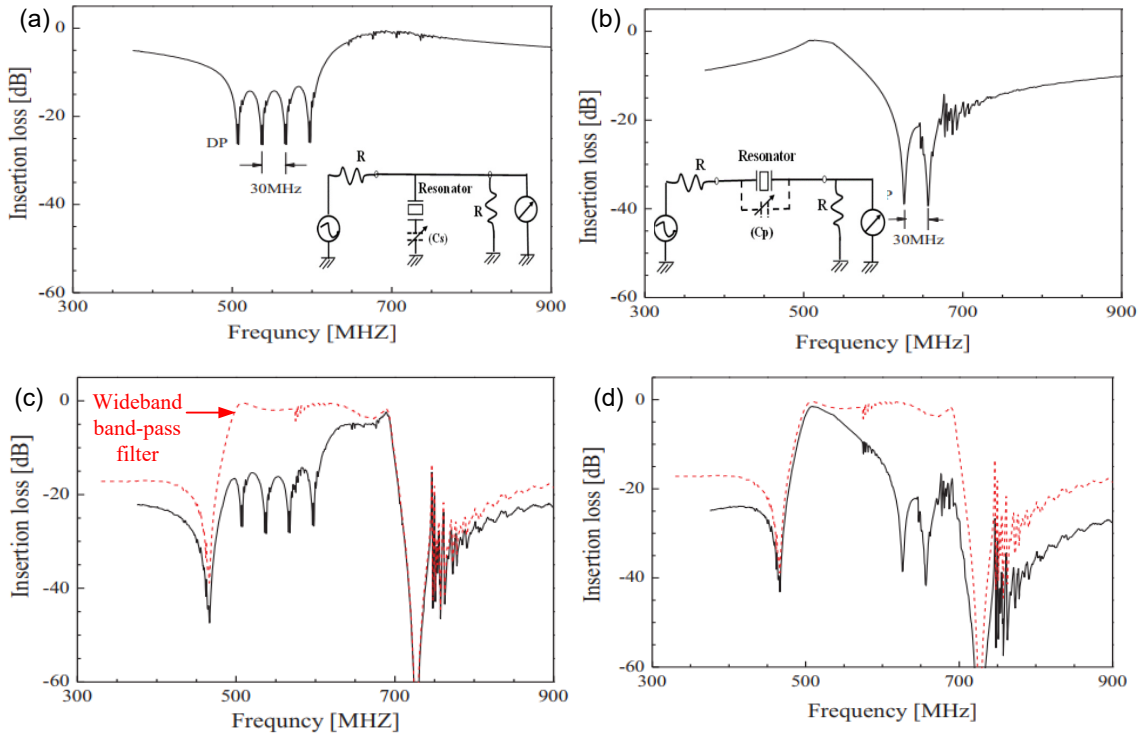

Figure 2-20: S-parameter response of (a, b) band-reject filters with parallel and series SAW resonators, (c, d) tunable bandpass filter by combining the wideband bandpass filter with band-reject filters [32].

Switchable and tunable acoustic resonators and filters using electric field-induced piezoelectricity in ferroelectric materials such as barium strontium titanate (BST) were also reported in [33] - [36]. In an intrinsically switchable BST-FBAR resonator, as shown in Figure 2-21, the acoustic response is controlled by an applied DC bias voltage. In the off state for 0 V DC bias, the device operates as a capacitor, while for the on state when a DC bias voltage is applied to the device, it functions

as an acoustic resonator with resonance and anti-resonance frequencies that can be tuned by adjusting the applied DC bias voltage.

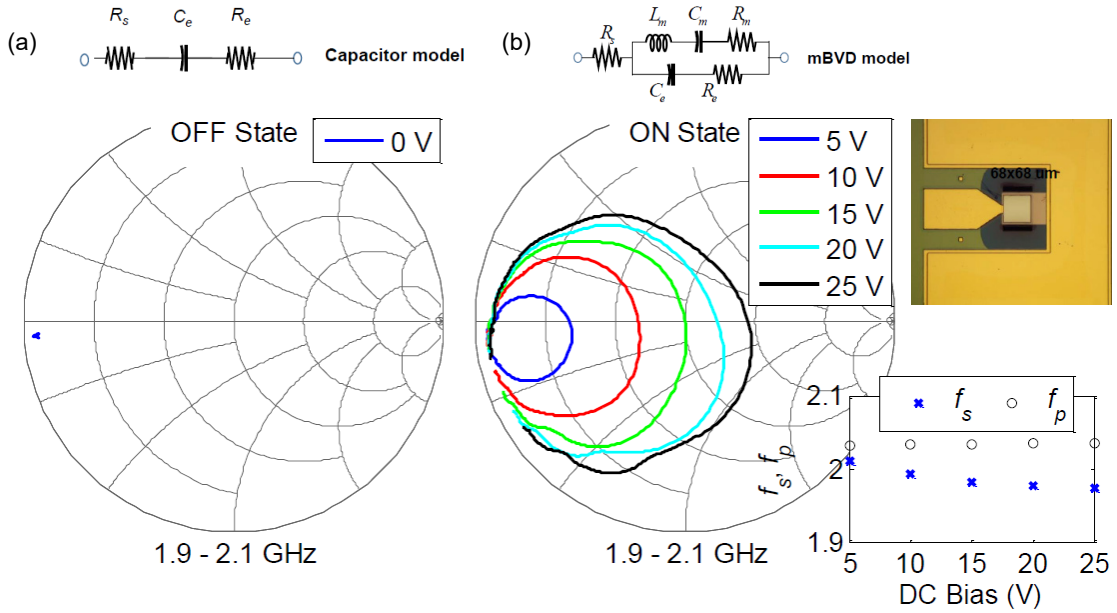

Figure 2-21: Intrinsically switchable BST-FBAR resonator (a) unbiased and (b) biased [33].

A switchable ladder-type bandpass filter using ferroelectric BST-on-Silicon composite FBAR resonators was presented in [35]. The passband response of the filter can be turned on and off by the application of an external bias voltage, as shown in Figure 2-22. The filter also shows an insertion loss of 7.8 dB with a 0.33% fractional bandwidth at 2.58 GHz when the filter operates in its on state with a DC bias voltage of 40 V. In the off state, the filter provides an isolation of 31 dBm. The main reason for the high insertion loss is the low resonator Q (<1000) for such a small fractional bandwidth of 0.33%.

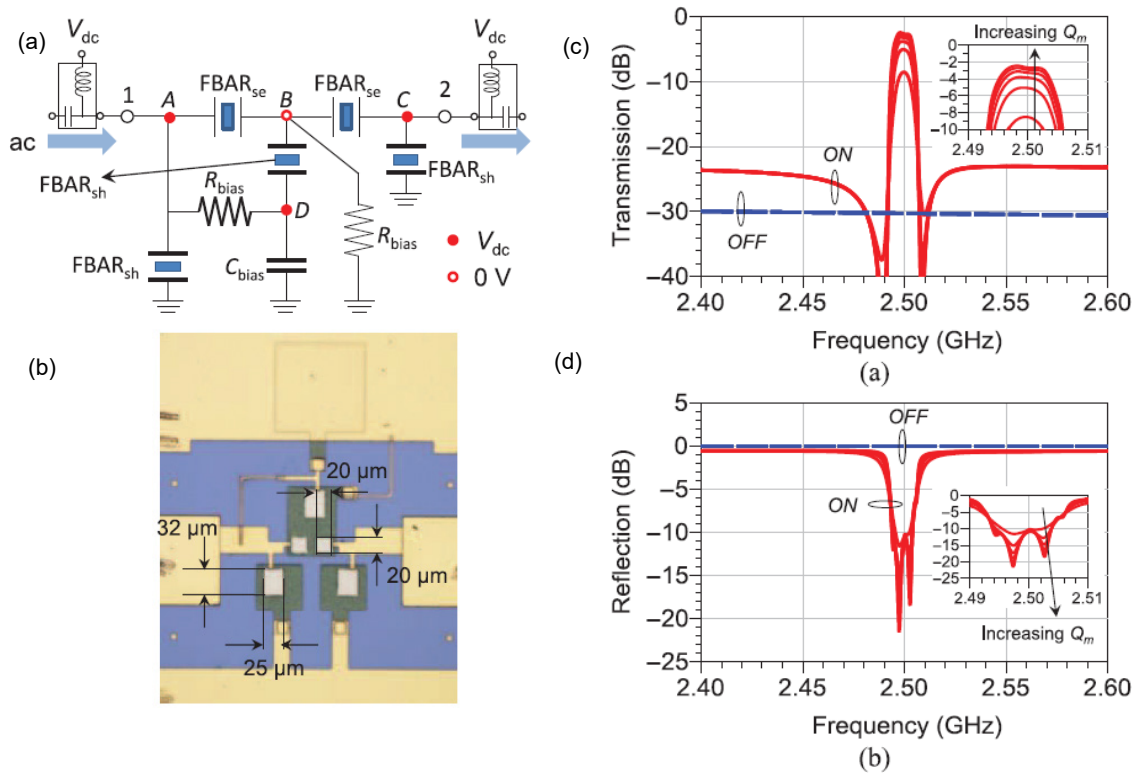

Figure 2-22: (a) Schematic circuit diagram and (b) optical image of switchable bandpass filter using BST-FBAR resonators, (c, d) S-parameter response for on and off states [35].

Chapter 3

Aluminum Nitride TPoS Resonators and Filters

3.1 Introduction

Contour Mode Resonators (CMR) [37], [38] and Thin-Film Piezoelectric on Substrate (TPoS) resonators [16], [39] have been studied for application in RF filters. This class of resonators utilizes an in-plane mode of vibration and combines the major advantages of surface acoustic wave (SAW) and bulk acoustic wave (BAW) technologies. Similar to SAW resonators the resonance frequency is determined by the lithography defined lateral dimensions of metal fingers in the IDT electrodes. The thickness of the piezoelectric layer has only a second order effect on resonance frequency. For this reason, resonators and filters with different center frequencies can be fabricated on the same chip. These laterally vibrating resonator structures not only provide compact size and ease of fabrication for multiple frequency filters, they also enable solutions for higher frequency and higher Q resonators required for future wireless communication applications. This is achieved by eliminating the acoustic energy loss through the substrate using an air cavity under the released acoustic membrane. Therefore, the mechanical losses are only limited to anchor losses and losses within the acoustic medium itself. This results in high Q values comparable to BAW technology. In this chapter, we demonstrate the application of a commercially available Silicon on Insulator (SOI) PiezoMUMPs process to fabricate AlN-on-Silicon resonators and filters. Using the SOI

process it is possible to combine the benefits of high piezoelectric coupling coefficient of AlN and the superior acoustic properties of single crystalline silicon substrate to achieve very high Q values while maintaining good performance over temperature and high power. Finite element modeling of the resonators using COMSOL and design of a 3-pole bandpass filter using direct electrical coupling between the resonators are presented. We also investigate linear and nonlinear performance of proposed resonators and filters over temperature and under high power [40].

3.2 Basics of CMR and TPoS Resonators

An overview of CMR resonators and thin-film piezoelectric-on-substrate (TPoS) resonators was given in Chapter 2. As shown in the 3D schematic view of Figure 3-1 (a), a CMR resonator consists of IDT electrodes deposited over a thin-film piezoelectric layer. In a CMR resonator, surface acoustic waves are guided laterally into a sufficiently thin plate (thickness < λ) and are referred to as Lamb waves [41]. A thin-film piezoelectric-on-substrate (TPoS) resonator, as shown in Figure 3-1 (b), consists of an IDT electrode and a thin-film piezoelectric layer similar to a CMR resonator. However, for TPoS resonators, there is a substrate layer with a thickness in the range of a few tens of microns under the piezoelectric layer. In a TPoS resonator, Lamb acoustic waves are excited through the IDT electrodes and the thin-film piezoelectric layer, but the waves travel inside the substrate medium instead of the piezoelectric layer itself. For this reason, using a substrate which is not a piezoelectric material but has good mechanical properties in terms of high acoustic wave velocity, lower acoustic loss and thermal conductivity for power handling, it is possible to fabricate TPoS resonators that have higher resonance frequency and Q value compared to conventional CMR resonators.

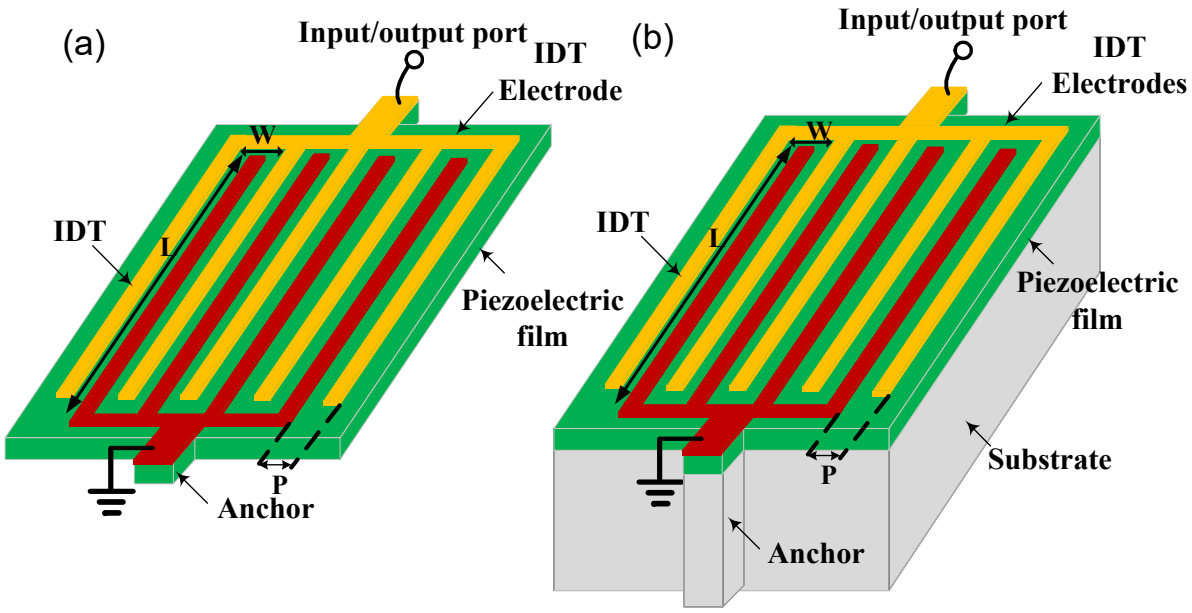

Figure 3-1: 3D schematic view of (a) CMR and (b) TPoS resonators

The resonance frequency of the main acoustic mode for both TPoS and CMR resonators is calculated from:

$$f = \frac{v}{\lambda} \quad (3.1)$$

Where v and λ are the phase velocity and wavelength of the propagating acoustic mode, respectively. The wavelength is determined by the IDT electrode pitch:

$$\lambda = 2 \times p \quad (3.2)$$

Figure 3-2 shows calculated phase velocities for different acoustic modes in an aluminum nitride (AlN) piezoelectric material for different thicknesses. As shown in the figure, the longitudinal mode has the highest phase velocity (around 11,000 m/s). This is the pure thickness mode that is used in all BAW resonators. The Rayleigh wave, which is the pure surface mode and is used in SAW resonators, has a phase velocity of around 6000 m/s. The phase velocity for the lowest symmetric Lamb wave (S_0 mode) used in CMR resonators has a phase velocity that is dependent

on the AlN film thickness. For very thin layers of AlN, the phase velocity of Lamb waves approaches the phase velocity of longitudinal waves. For this reason, by using CMR resonators, it is possible to achieve a higher resonance frequency close to BAW resonators. In the next sections, we will discuss the modeling, design and fabrication of TPoS resonators and filters using the PiezoMUMPs process.

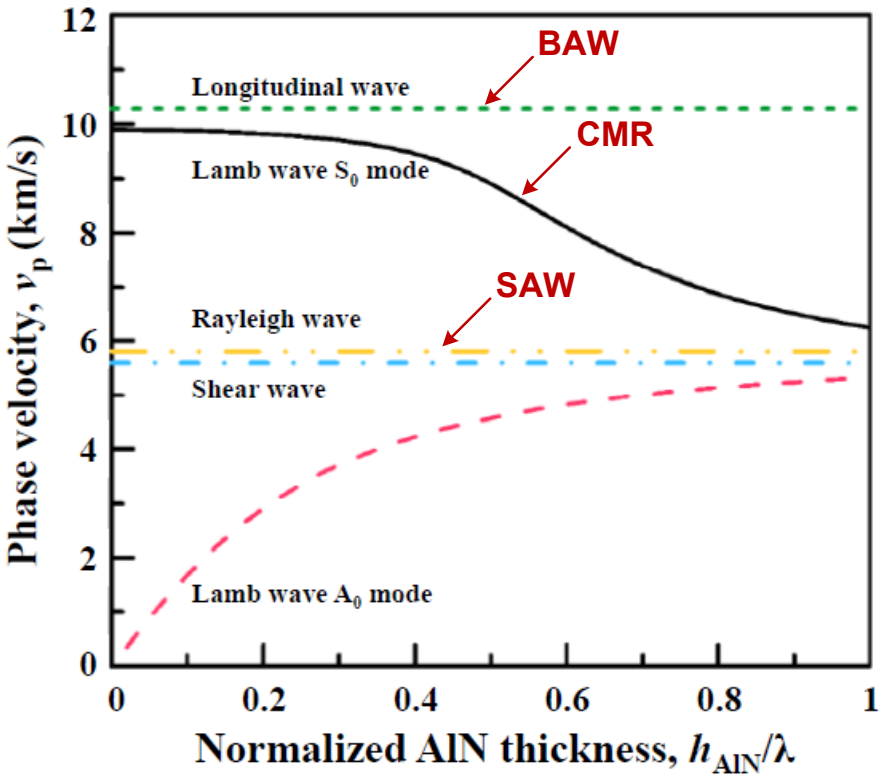

Figure 3-2: Phase velocities for different acoustic modes in AlN material [42].

3.3 TPoS Resonator Design

The proposed TPoS resonator, as shown in Figure 3-3, consists of IDT electrodes deposited over a thin-film AlN piezoelectric layer and a SOI silicon substrate. In a TPoS resonator, lamb wave acoustic waves are excited through the IDT electrodes and the thin-film piezoelectric layer, but the waves are travelling inside the silicon substrate instead of the piezoelectric layer itself. The SOI silicon is selected to have a high acoustic wave velocity to achieve a higher resonance frequency. In addition, the substrate material is also required to have low mechanical losses and good thermal conductivity to obtain a higher Q value and suitable power handling capability.

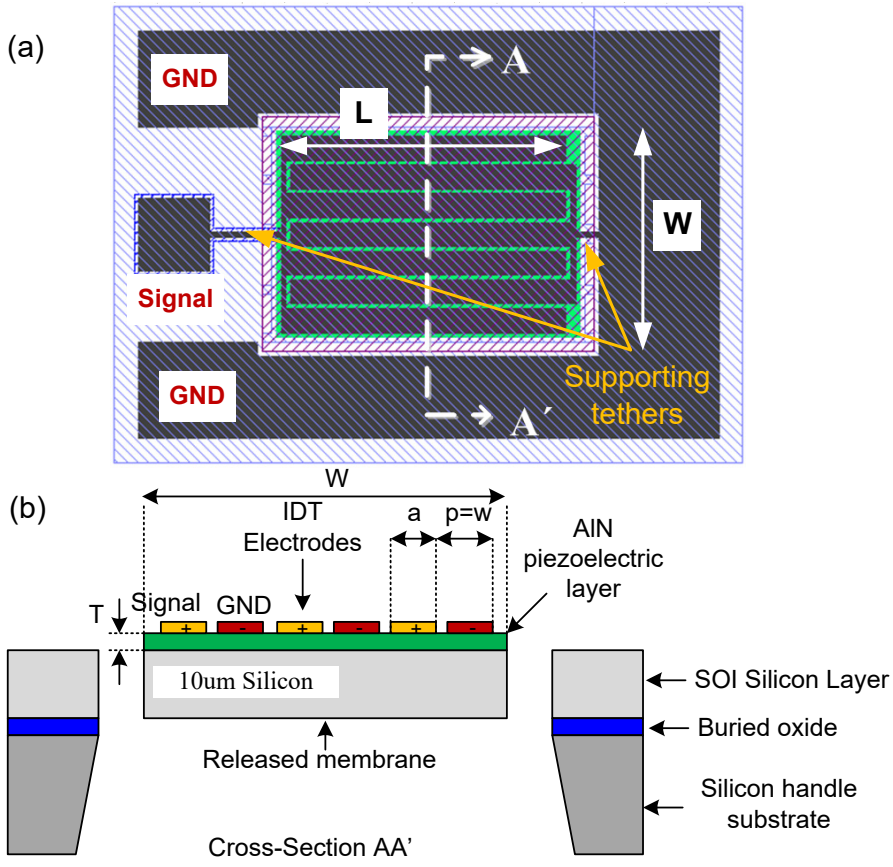

Figure 3-3: a) Top view and b) cross-section view of the TPoS resonator.

The released AlN-on-Si membrane acting as acoustic resonant body consists of a 0.5 µm thick AlN piezoelectric layer and a 10 µm thick single crystalline silicon layer. The IDT electrodes consist of two sets of 1 µm thick aluminum metal fingers with equal length and width (L × W) and periodic spacing of p as shown in Figure 3-3. One set of IDT electrodes are connected to the RF signal while the other set is grounded in a one-port configuration of the proposed resonator. The 10 µm thick highly doped silicon layer is conductive and it can also act as a ground electrode.

An excitation scheme of TPoS resonator is shown in Figure 3-4 (a). The IDT electrodes are excited out of phase with respect to each other and the conductive silicon layer is used as a ground plane. This creates electric fields both in lateral and vertical directions. The induced strain due to piezoelectric effect generates lamb waves into the AlN-on-Si membrane. The loading effect of AlN and metal electrodes over the silicon layer breaks the symmetry compared to a purely silicon membrane. Hence, the lowest order symmetric mode (S_0) is distorted to a 1st order quasi-symmetric mode (QS_0). Figure 3-4 (b) shows the simulated mode shape for the QS_0 mode using COMSOL.

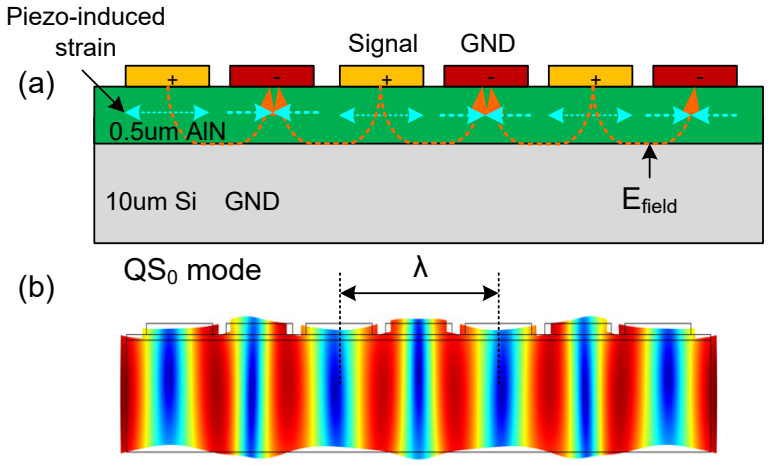

Figure 3-4: a) Excitation of lamb waves and b) simulated mode shape for QS_0 mode in AlN-on-Si membrane.

The pitch distance (P = λ/2) determines the resonance frequency for the intended QS_0 mode by using the equation below:

$$f_r = \frac{v_p}{\lambda} = \frac{1}{2p}\sqrt{\frac{E_{eq}}{\rho_{eq}}} \quad (3.3)$$

where v_p, ρ_{eq} and E_{eq} are the phase velocity, equivalent mass density and Young's modulus for the AlN-on-Silicon material stack, respectively. In the case of sufficiently thin AlN piezoelectic film ($t_{AlN} < \lambda$), these parameters are mainly set by the mechanical propoerties of the single crystalline silicon layer. The number of fingers and total length of the resonator are selected to achieve a specific impedance value. Figure 3-5 shows 3D FEM simulation results for a TPoS resonator with metal finger width and pitch values of a = 10 µm and p = 15 µm, respectively. The resonator has a total length of L = 315 µm and width of W = 240 µm. The main QS0 mode for the designed resonator occurs at f_{QS0} = 268MHz.

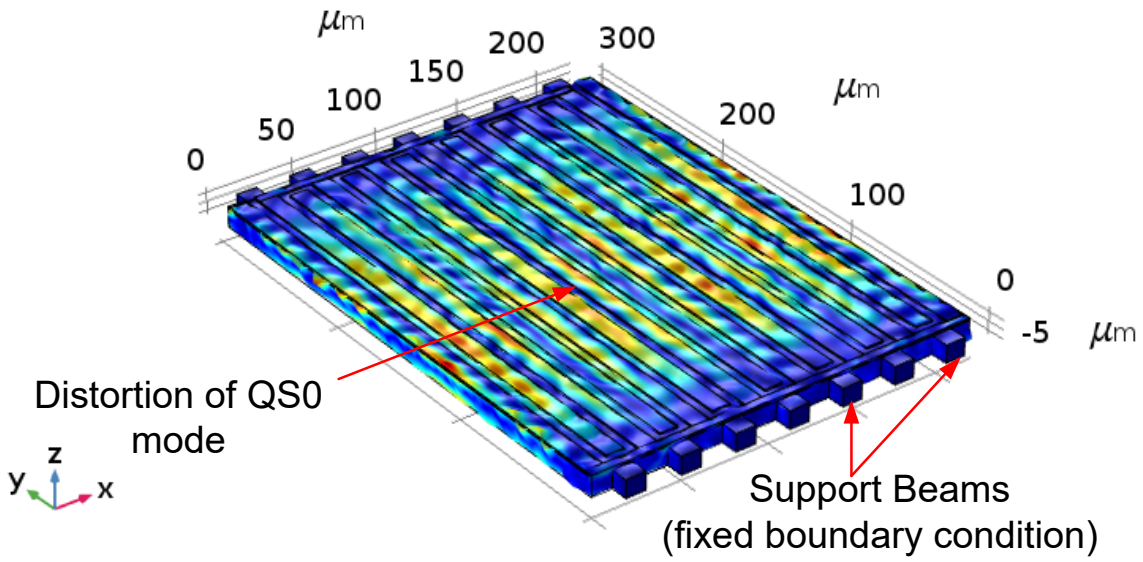

Figure 3-5: 3D FEM simulation showing QS0 mode.

A typical frequency response of a piezoelectric resonator is shown in Figure 3-6. At acoustic resonance frequency (f_r), the resonator has the highest admittance (lowest impedance), while at anti-resonance frequency (f_a), the resonator behaves as an open circuit with the lowest admittance value. The behavior between the two resonances is inductive and out of this range is capacitive, as shown on the Smith chart in Figure 3-6 (b).

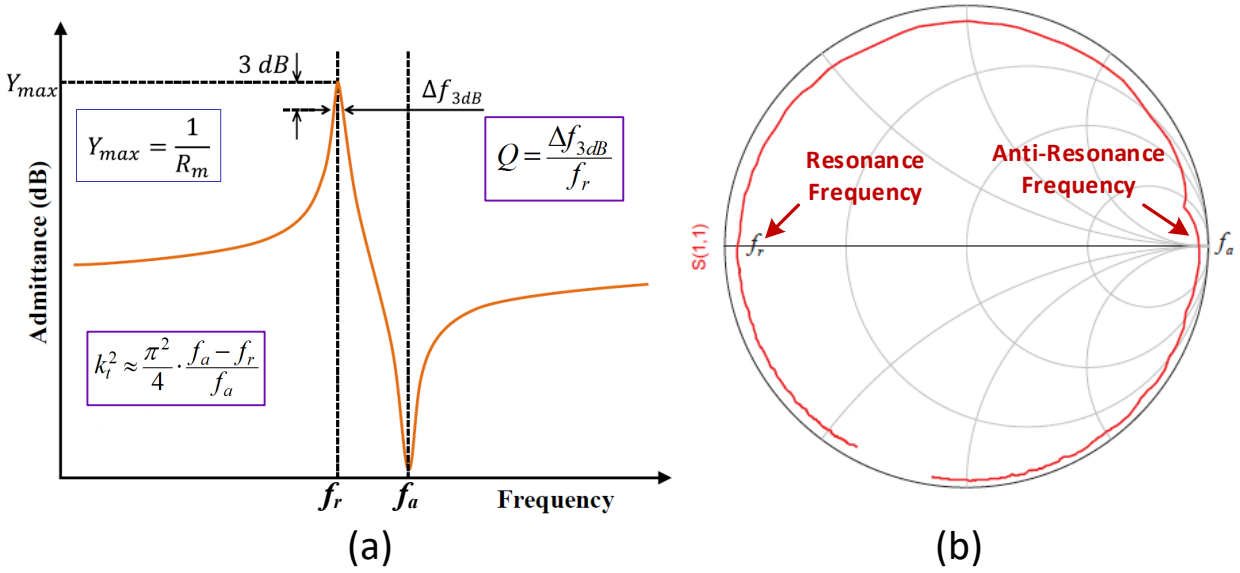

Figure 3-6: (a) Electrical admittance and (b) S-parameter response of a piezoelectric resonator [42].

The electrical behavior of the proposed TPoS resonator can be described by an equivalent circuit known as the Butterworth Van Dyke (BVD) model, as shown in Figure 3-7. The figure shows an equivalent circuit model for both one-port and two-port configurations. C_o and C_f represent the static capacitance between the IDT electrode fingers, C_m is the motional capacitance, and L_m is the motional inductance. The motional resistance R_m represents the mechanical energy loss in the membrane. The parasitic resistance R_p models electrical loss through the single crystalline silicon membrane.

The motional branch, composed of C_m, L_m and R_m, represents the resonance frequency f_r and the parallel static capacitance C_o ($C_f << C_o$) represents the anti-resonance frequency. For a one-port resonator, the admittance is expressed as:

$$Y_{in} = \frac{1}{Z_{in}} = \frac{\frac{C_0}{C_m} + j\omega C_0 R_m - \omega^2 C_0 L_m + 1}{R_m + j\omega L_m + \frac{1}{j\omega C_m}} \qquad (3.4)$$

For an ideal case when $R_m = 0$, infinite admittance occurs at resonance frequency f_r, as given by:

$$f_r = \frac{\omega_s}{2\pi} = \frac{1}{2\pi}\frac{1}{\sqrt{L_m C_m}} \qquad (3.5)$$

The admittance is zero at anti-resonance frequency f_a, which can be expressed as:

$$f_a = \frac{\omega_p}{2\pi} = \frac{1}{2\pi}\sqrt{\frac{C_0 + C_m}{L_m C_m C_0}} = f_r \cdot \sqrt{1 + \frac{C_m}{C_0}} \qquad (3.6)$$

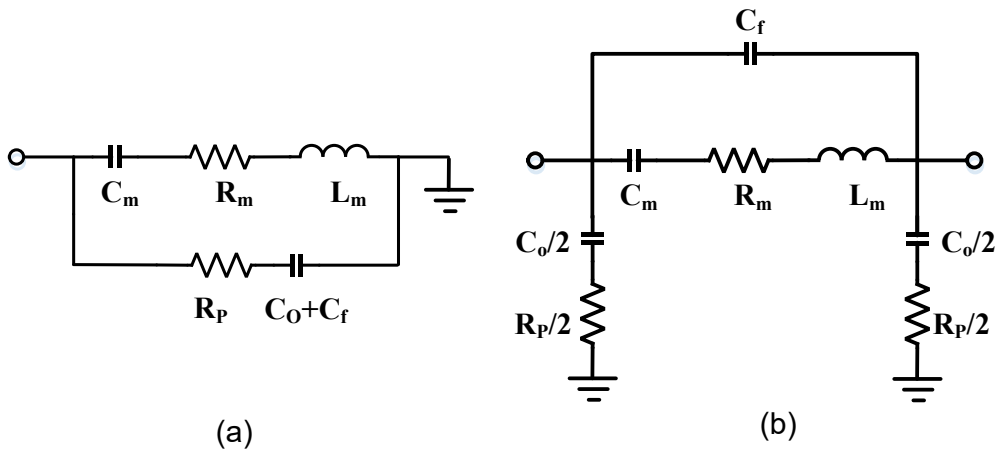

Figure 3-7: Butterworth Van Dyke (BVD) equivalent circuit model of TPoS resonator (a) one port and (b) two port model.

The resonator can be designed as a two-port device with input and output signal ports. Figure 3-7 (b) shows an equivalent circuit model of a two-port TPoS resonator. The equivalent circuit model parameters can be derived using the energy method introduced by Piazza et al. [12]:

$$C_0 \approx n\varepsilon_{33}\varepsilon_0 \frac{wL}{T}, \qquad R_m = \frac{1}{n}\frac{\pi}{8}\frac{T}{L}\frac{\rho_{eq}^{1/2}}{E_{eq}^{3/2} d_{31}^2 Q}$$
$$L_m = \frac{1}{n}\frac{\rho_{eq}}{8}\frac{wT}{L}\frac{1}{E_{eq}^2 d_{31}^2}, \quad C_m = n\frac{8}{\pi^2}\frac{wL}{T}E_{eq} d_{31}^2 \tag{3.7}$$

where ε_0 is the permittivity of the free space; ε_{33} is the dielectric constant of AlN along the c-axis; L, w and T, as shown in Figure 3-3, are the length, width and thickness of each sub-section of the resonator, respectively; E_{eq} and ρ_{eq} are the equivalent in-plane modulus of elasticity and mass density of stacked AlN-on-Silicon layers; d_{31} is the piezoelectric constant coefficient of AlN film along the Z-axis; and n represents the number of IDT fingers.

The Q value of a piezoelectric resonator is defined as the ratio of stored energy and the energy dissipated during one cycle of oscillation. It indicates how well the mechanical energy is confined within the resonator:

$$Q = \omega.\frac{energy\ stored}{power\ dissipated} = 2\pi\frac{energy\ stored}{energy\ dissipated\ per\ cycle\ of\ oscillation} \tag{3.8}$$

Common energy loss mechanisms in a piezoelectric resonator include mechanical loss in the acoustic medium, electrical losses, spurious mode excitation and anchor loss. In order to calculate the overall Q value, all loss mechanisms must be considered, as given by:

$$1/Q_{tot}=1/Q_{MTR}+1/Q_{ELE}+1/Q_{ANC}+1/Q_{SPU} \tag{3.9}$$

The resonator Q can be derived from measured or simulated electrical response using the equation below [43]:

$$Q = \frac{\omega |S_{11}| \, group\ delay\ (S_{11})}{1 - |S_{11}|^2} \quad (3.10)$$

Q value can also be directly obtained from the -3dB bandwidth measurement of the admittance peak, as shown in Figure 3-6 (a), using the equation below:

$$Q = \frac{\Delta f_{3dB}}{f_r} \quad (3.11)$$

The quality factor can also be expressed using the equivalent circuit model parameters:

$$Q = \frac{\sqrt{L_m / C_m}}{R_m} \quad (3.12)$$

Another important parameter for piezoelectric resonators is the electromechanical coupling coefficient (k_t^2), which is a measure of energy transduction efficiency between electrical and mechanical domains. This parameter also determines the bandwidth of the RF filters that can be constructed using piezoelectric resonators, as will be explained later in the filter design section. The coupling coefficient k_t^2 can be obtained from the measured electrical admittance and f_r and f_a values or by using the equivalent circuit parameters, as expressed below:

$$k_t^2 \approx \frac{\pi^2}{4} . \frac{f_a - f_r}{f_a} \approx \frac{\pi}{8} . \frac{C_m}{C_0} \quad (3.13)$$

The design of a TPoS resonator starts by determining the center frequency and selecting the required IDT electrode pitch and spacing values. Then the number of fingers and the total length of the resonator are selected in order to achieve a specific impedance value for the resonator (e.g., a 50 Ω resonator). Figure 3-8 shows the layout of TPoS resonators with different IDT electrode pitch values ranging from 10 um to 30 um. These resonators are designed to cover a frequency

range from 140 MHz to 350 MHz. All of the resonators have almost the same length L and width W.

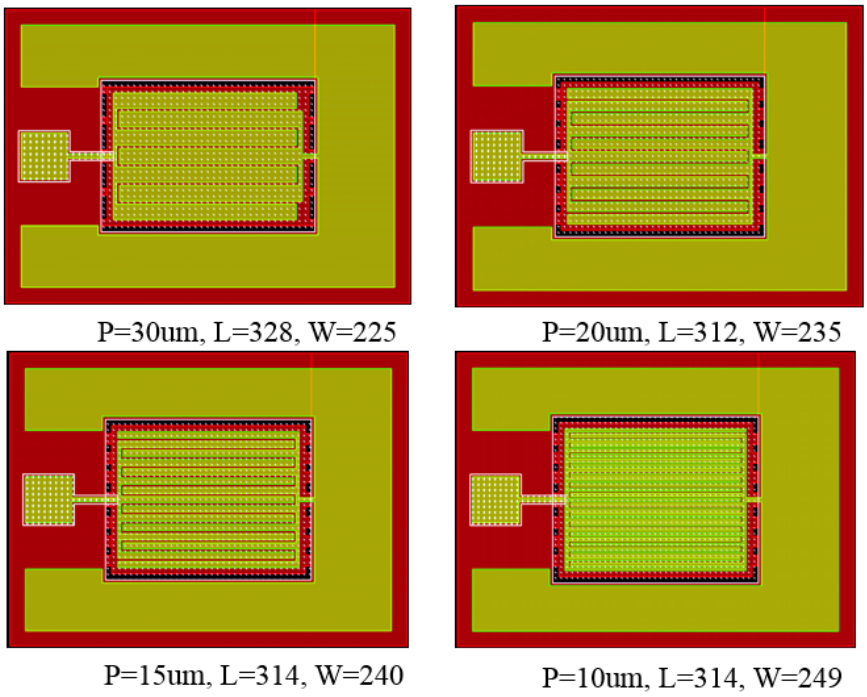

Figure 3-8: Layout of TPoS resonators with different center frequencies.

The simulated wideband admittance response of the TPoS resonator with the largest pitch size (p = 30 um) is shown in Figure 3-9. As depicted in the figure, the strongest Lamb wave mode (QS_0) is around 140 MHz. There are spurious acoustic modes which will create spurious passbands in the filter response. The second strongest mode is the lowest Quasi-Asymmetric Lamb wave (QA_0) mode, which has a frequency of around 33.5 MHz.

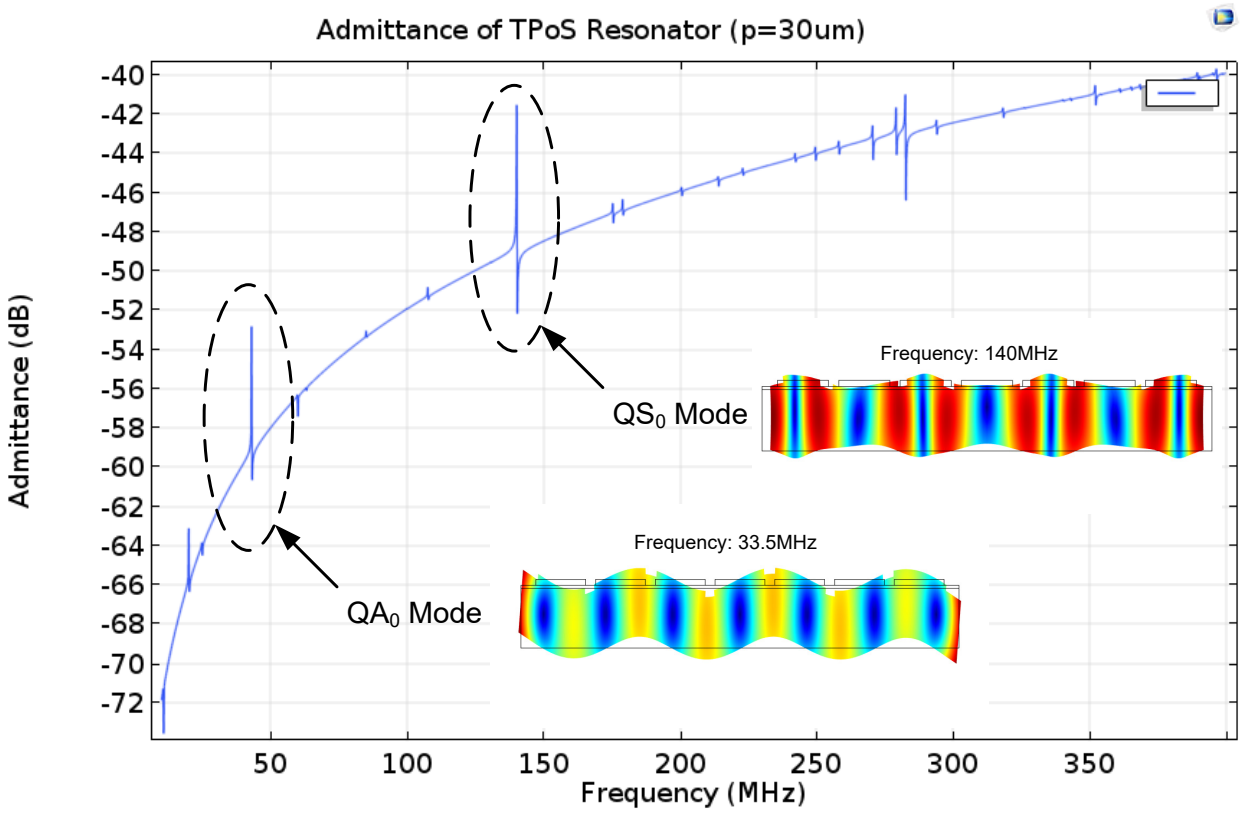

Figure 3-9: Simulation electrical admittance for TPoS resonator with p=30um in COMSOL and mode shapes for QS_0 and QA_0 modes.

The simulated S-parameter response (S_{11}) for the one-port resonator with a pitch distance of p = 30 um is illustrated in Figure 3-10. This figure also shows the main resonance at 140 MHz and the lowest spurious mode at 33.5 MHz. We can also see the other spurious modes in both the admittance and S_{11} response. Since the two-port equivalent circuit model, as shown in Figure 3-7 (b), has a symmetric configuration, it is more accurate to perform FEM simulation on a two-port resonator. Figure 3-11 shows the layout of a two-port TPoS resonator. As depicted in the figure, the two RF ports serve as input and output and the Silicon slab in the resonant membrane is used as the ground plane.

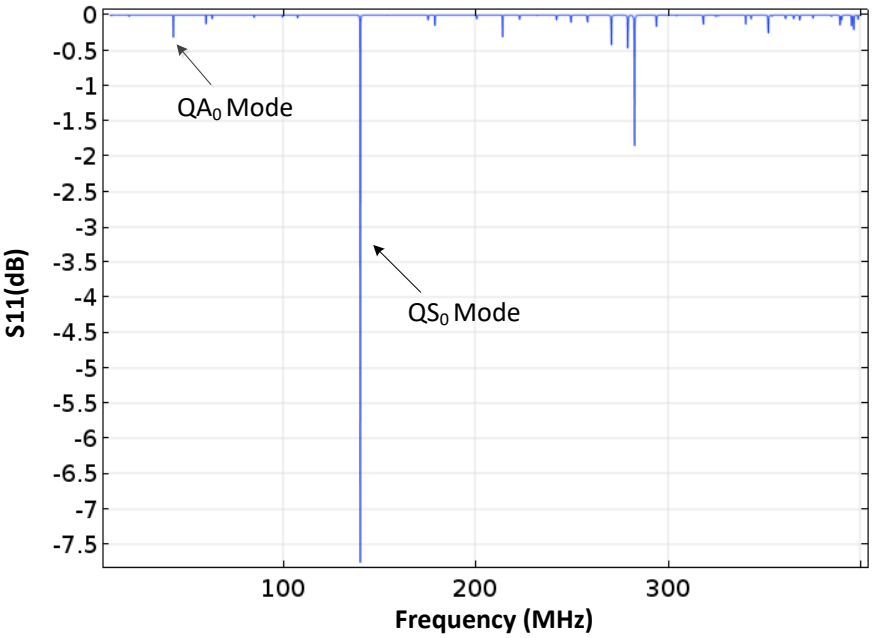

Figure 3-10: Simulated S-parameter (S_{11}) for TPoS resonator with p = 30 um in COMSOL

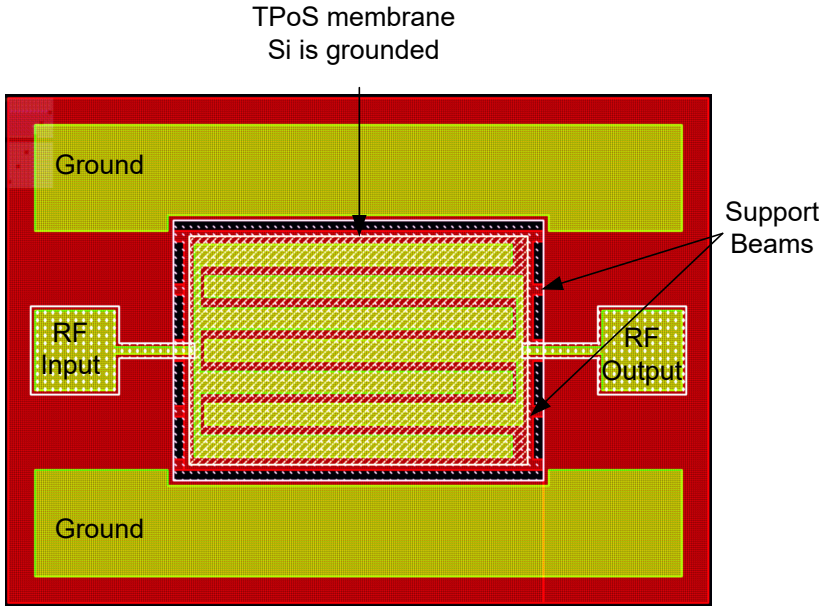

Figure 3-11: Layout of two-port TPoS resonator with p = 30 um.

Figure 3-12 shows the simulated wideband S-parameter response (S_{21}) in COMSOL for the two-port resonator configurations with different IDT electrode pitch values. The main mode (QS_0) is

determined by the highest peak observed in the S_{21} response. The other spurious modes also create peaks at other frequencies which are not as strong as the main mode, as shown in Figure 3-12.

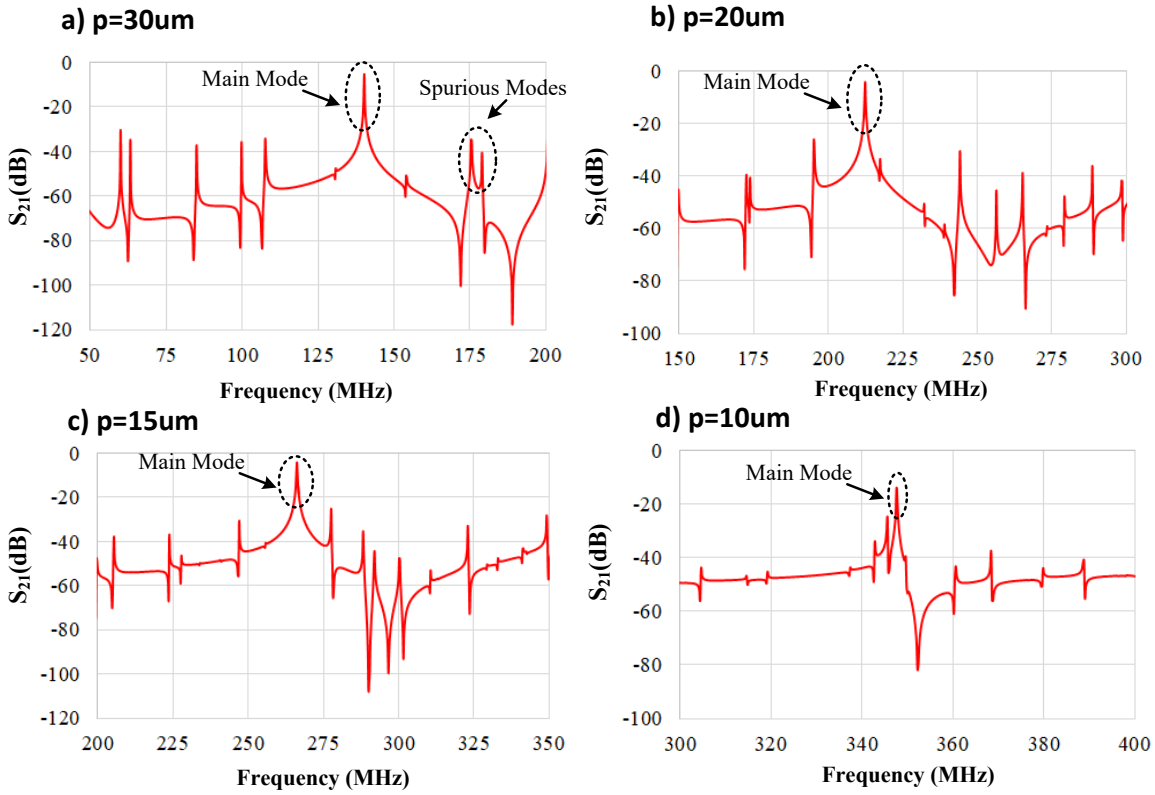

Figure 3-12: Simulated S-parameter response (S_{21}) in COMSOL for two-port TPoS resonators with different pitches (a) 30 um; (b) 20 um; (c) 15 um and (d) 10 um.

The simulated S_{21} response shows the resonance frequency varies from 140 MHz for p = 30 um to 347 MHz for a resonator with p = 10 um. Using the PiezoMUMPs process and due to fabrication constraints for minimum metal-to-metal spacing, the minimum IDT electrode pitch is p = 10 um.

3.4 PiezoMUMPs Fabrication Process

Figure 3-13 illustrates the cross-sectional process flow for the TPoS resonators fabricated using the PiezoMUMPs process. PiezoMUMPs is a commercially available MEMS fabrication process designed for the general purpose micromachining of piezoelectric devices on Silicon-on-Insulator (SOI) substrates [3]. The fabrication process starts with a 0.2 um thermally grown oxide layer over an SOI wafer, as shown in Figure 3-13 (a). This oxide layer is used as a dielectric to isolate the metal electrodes from the conducting silicon layer underneath. In the next step, a 0.5 um piezoelectric AlN layer is deposited using RF sputtering and then patterned. The metal electrodes are deposited using e-beam evaporation of 20 nm Chromium (Cr) followed by 1 um Aluminum (Al) and then patterned using Mask 3. The wafer is coated with a UV sensitive photoresist and exposed to UV light for subsequent etching of the Silicon layer using deep reactive ion etching (DRIE) from the top side. The final processing step includes patterning and etching the handle silicon substrate from the back side using DRIE. During this step, the buried oxide layer in the SOI stack acts as an etch stop layer protecting the AlN piezoelectric layer. This oxide layer is then removed using wet etching and the piezoelectric membrane is released, as depicted in the cross-sectional view in Figure 3-13 (e).

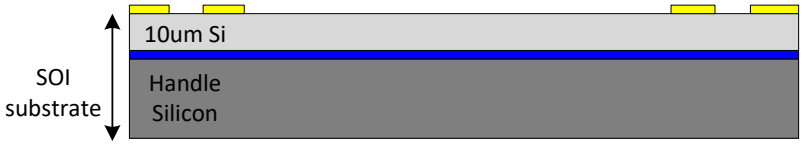

a) Thermal Oxide is grown and patterned (mask 1)

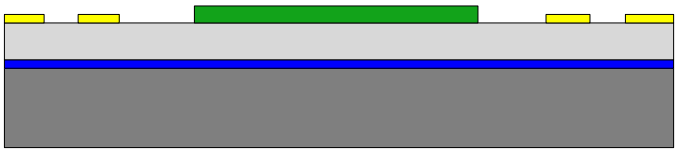

b) Aluminum Nitride is deposited by RF sputtering and patterned (mask 2)

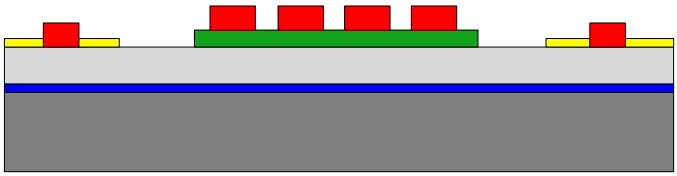

c) Metal electrodes (Al+Cr) are deposited by e-beam evaporation and patterned (mask 3)

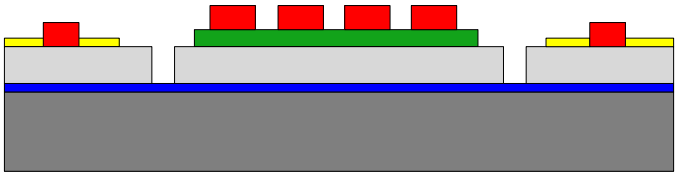

d) Top silicon layer is patterned and etched by DRIE (mask 4)

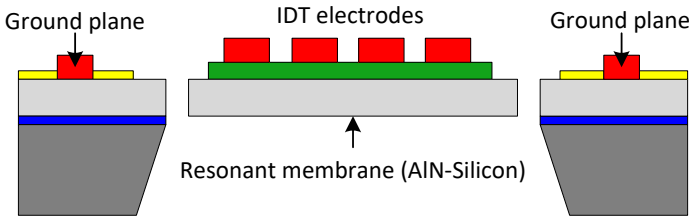

e) Handle substrate is etched by patterning and DRIE from back-side and then oxide layer is removed using wet etch to release the membrane (mask 5)

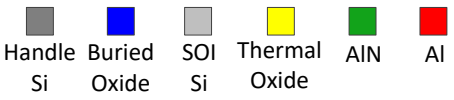

Figure 3-13: PiezoMUMPs processing steps for a TPoS resonator.

3.5 Experimental Results

Optical images of fabricated resonators in one-port and two-port configurations for 15 um pitch are shown in Figure 3-14. The linear S-parameter response of the resonators are measured using a VNA and standard SOLT calibration. Figure 3-15 shows the measured wideband admittance of the one-port resonator. The main QS0 mode occurs at 268 MHz. There are also spurious modes with the strongest being the lowest quasi-asymmetric lamb wave (QA0) mode which has a frequency around 118 MHz. The second strongest spurious mode close to the main mode is at 250 MHz. These spurious modes create spurious passbands in the filter response and they need to be mitigated by optimized placement of supporting tethers. As shown in the inset of Figure 3-15, the measured resonance and anti-resonance frequencies of the fabricated one-port TPoS resonator are $f_r = 268.04$ MHz and $f_a = 268.12$ MHz, respectively. This results in a measured coupling coefficient k_t^2 less than 0.1% using equation (3.13). The electromechanical coupling coefficient k_t^2 determines the bandwidth of the RF filters that can be constructed using these resonators.

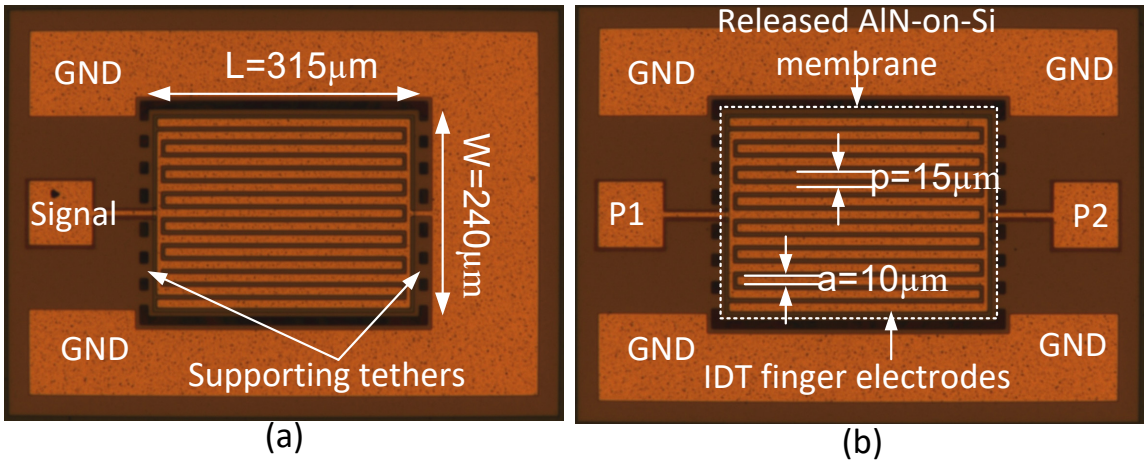

Figure 3-14: Images of fabricated resonators in a) one-port and b) two-port configuration for p = 15 um.

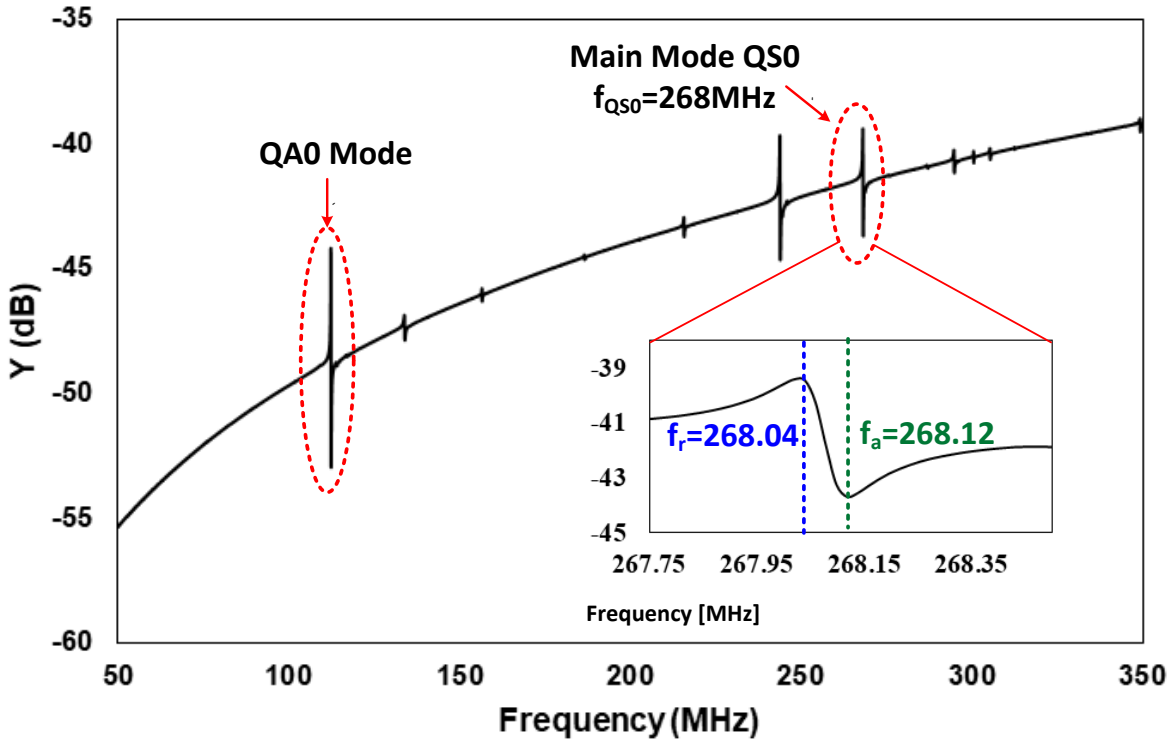

Figure 3-15: Measured admittance of one-port resonator with p = 15 um.

The measured and simulated return loss (S_{11}) for the one-port resonator is shown in Figure 3-16 (a). This figure also shows the main resonance mode at 268 MHz and the spurious modes similar to admittance plot. There is a good agreement between measured data and FEM simulation

in COMSOL. Figure 3-16 (b) shows measured wideband S-parameter response (S_{21}) for the two-port resonator configuration. The main QS0 mode is determined by the highest peak observed in S_{21} response. The other spurious modes also create passbands at other frequencies. The equivalent MBVD circuit model parameters for the fabricated resonators, as shown in Figure 3-17 (c), are obtained by fitting the S-parameter (S_{11}) and impedance response from measurements to the S_{11} and impedance response from the MBVD circuit model within a frequency range near the resonance frequency, as shown in Figure 3-17 (a) and (b).

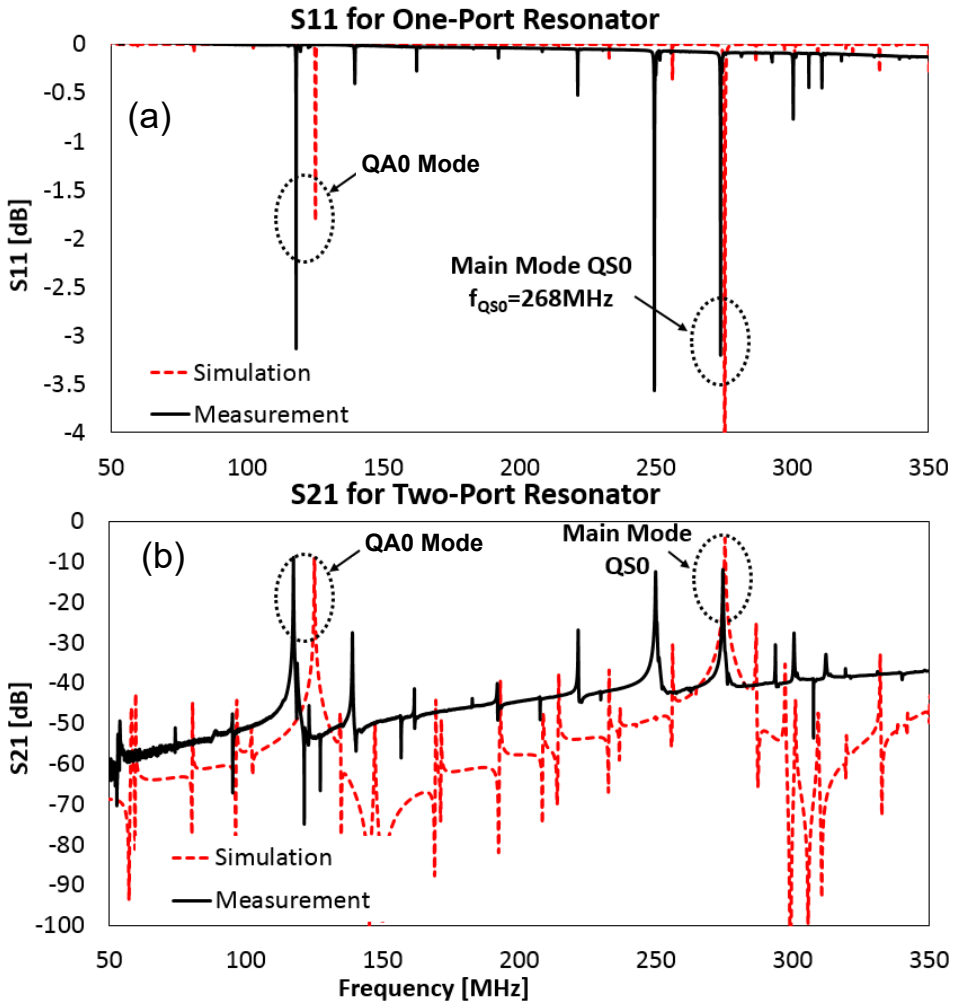

Figure 3-16: Measured vs. simulated S-parameters for a) one-port and b) two-port TPoS resonators.

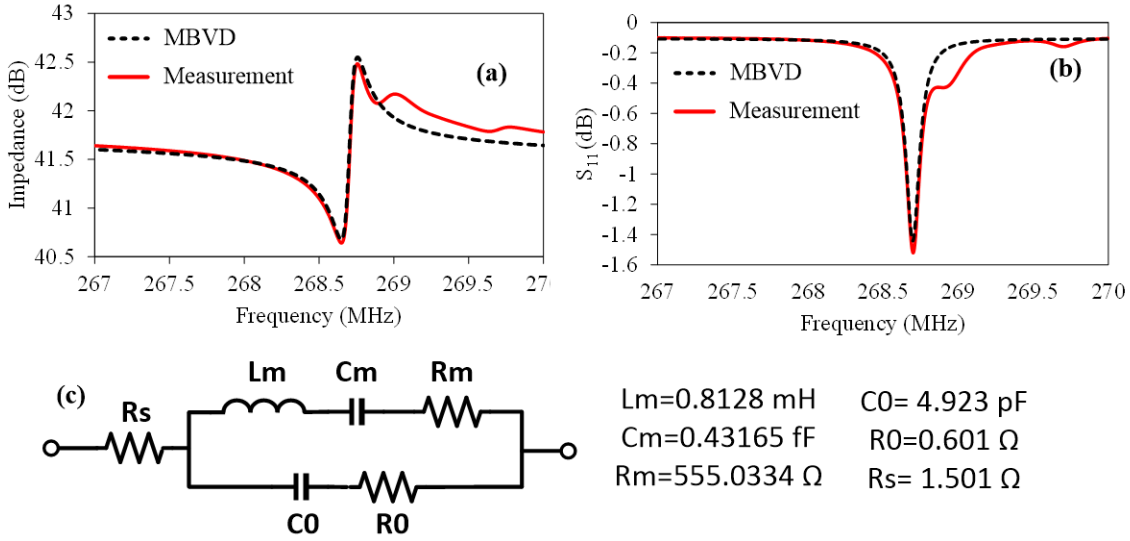

Figure 3-17: a) and b) parameter fitting around QS0 mode; c) Equivalent MBVD circuit model of a one-port TPoS resonator

In the BVD circuit model of Figure 3-17 (c), C_o represent static capacitance between the IDT electrode fingers, C_m is the motional capacitance and L_m is the motional inductance. The motional resistance R_m represents mechanical energy loss in the membrane. The parasitic resistance R_p models electrical loss through the conductive single crystalline silicon layer. The Q value of a piezoelectric resonator indicates how well the mechanical energy is confined within the resonator. In the case of designed TPoS resonators, energy loss mechanisms include mechanical loss in the acoustic medium, electrical losses, spurious mode excitation and anchor loss. To calculate overall Q, all loss mechanism must be considered. The resonator Q can be derived from measured S-parameters [43] using equation (3.10).

Figure 3-18 shows measured return loss and extracted Q values for the one-port resonator at different temperatures ranging from -196ºC (77ºK) to +120ºC. A change in both center frequency and resonator Q is observed.

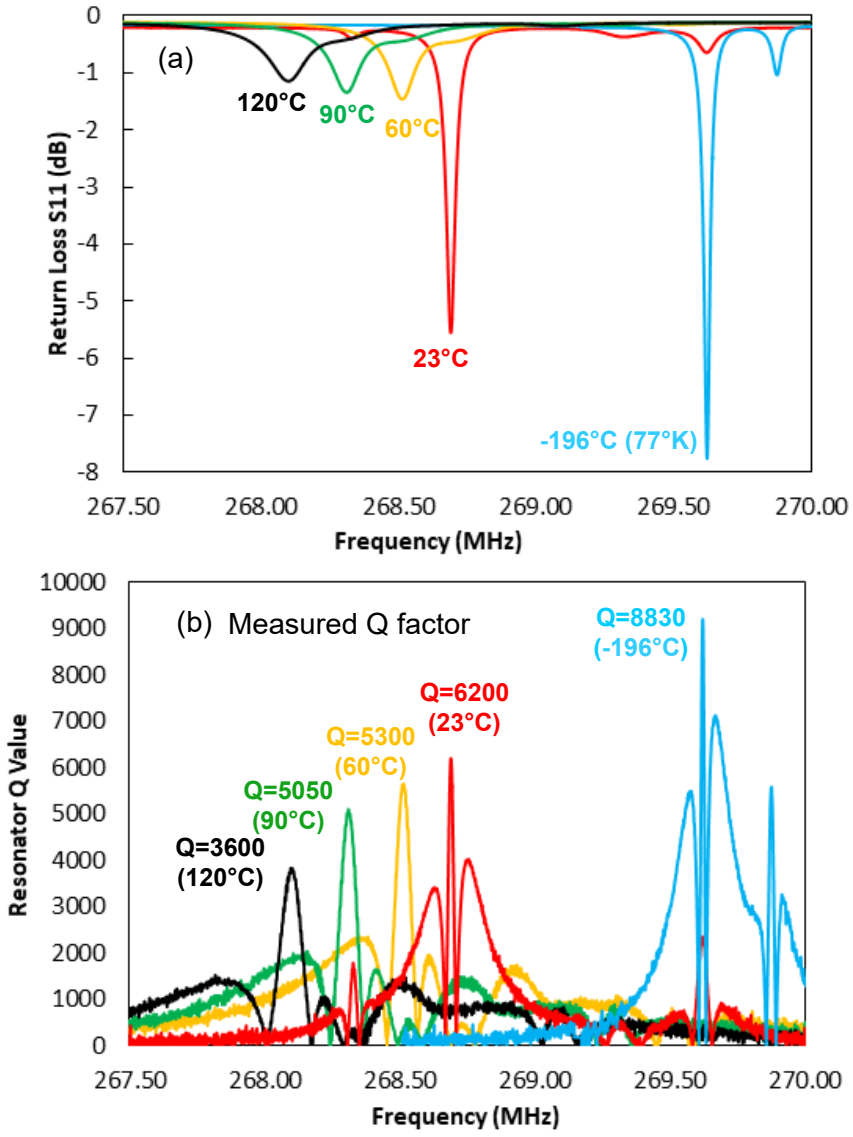

Figure 3-18: Measured a) return loss and b) Q at different temperatures.

The resonance frequency is shifted down by almost 1.5 MHz resulting in a temperature coefficient of frequency (TCF = -23 ppm/ºC) which is related to change in effective Young's modulus and density of AlN-on-Si stack according to equation (3.3). The resonator Q, as shown in Figure 3-18 (b), varies from 8830 at -196ºC to 3600 at +120ºC. The higher Q factor at lower temperatures is related to lower mechanical damping loss in the acoustic medium and also lower

electrical losses in the conductive silicon substrate and metal loss in IDT electrodes.

Nonlinear characterization of the fabricated resonator is performed using a single tone 2nd harmonic measurement setup. A high-power tone with a frequency f around the resonance frequency is applied to the resonator and the reflected 2nd harmonic emission is measured at 2×f. The peak value of 2nd harmonic changes from -76dBm to -52dBm (24dBm variation) while the incident power is swept from 8dBm up to 20dBm, as shown in Figure 3-19.

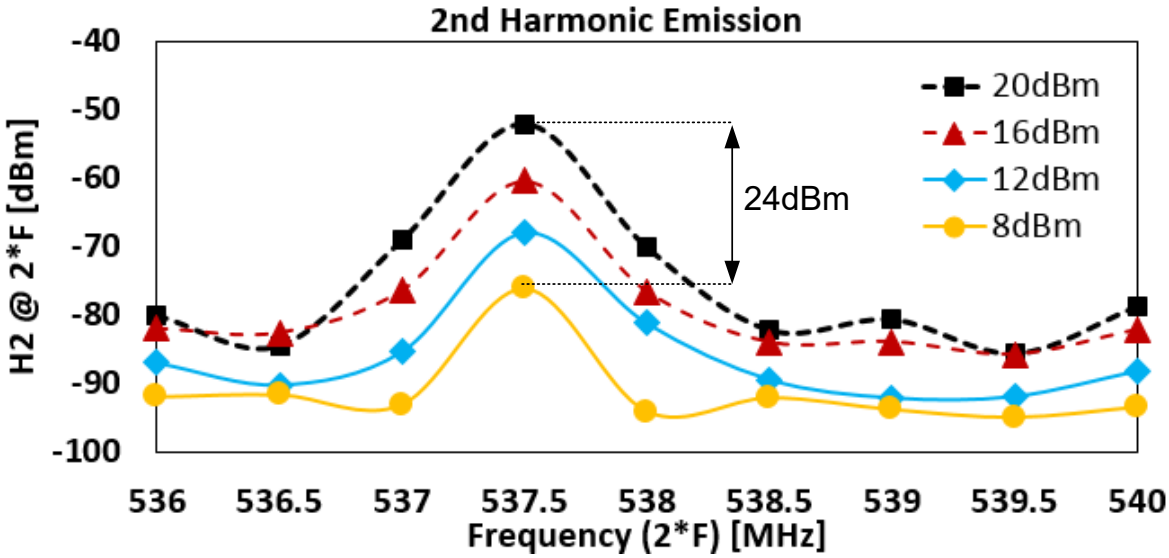

Figure 3-19: 2nd harmonic emission at different power levels.

3.5.1 3-Pole Bandpass TPoS Filter

A three-pole bandpass filter is designed using direct capacitive coupling between three identical resonators as shown in Figure 3-20 (a). In this configuration the intrinsic shunt capacitance of each resonator modeled by C_p in the BVD circuit model provides the required coupling between the resonators, as shown in Figure 3-20 (b). Figure 3-21 shows measured

insertion loss S_{21} for the fabricated filter at room temperature and at 77ºK. The insertion loss obtained at room temperature is relatively high since the filter is designed with a very narrow bandwidth (60 KHz) considering the extremely low coupling coefficient of the proposed TPoS resonators (k_t^2 = 0.1%). Also the particular resonators used in this fabrication run of the filter exhibited a Q of only 2800 at room temperature and a Q of 3800 at 77ºK. The insertion loss of the filter at room temperature would be reduced to half if the resonators shown in Figure 3-18 with the Q value of 6200 at room temperature were used in implementing this filter.

3.6 Summary

A commercially available PiezoMUMPs process is used to design and fabricate TPoS resonators with high Q values. Design, modeling, FEM simulations and linear and nonlinear characterization of the fabricated resonators over a wide range of temperatures and power sweep are presented. The proposed resonator is used to design a narrowband bandpass filter using direct electrical coupling between the resonators, where it is shown that about 3 dB improvement in insertion loss can be achieved when the filter operates at 77ºK.

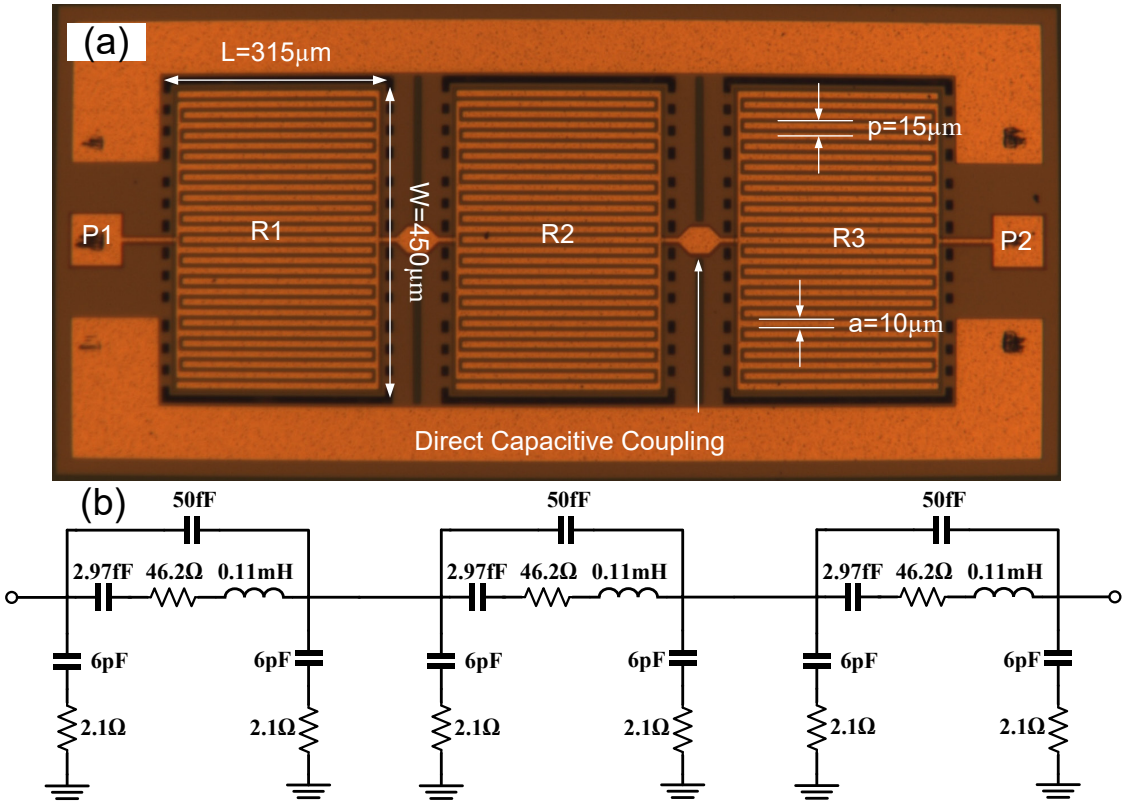

Figure 3-20: a) fabricated 3-pole bandpass filter and b) equivalent circuit model.

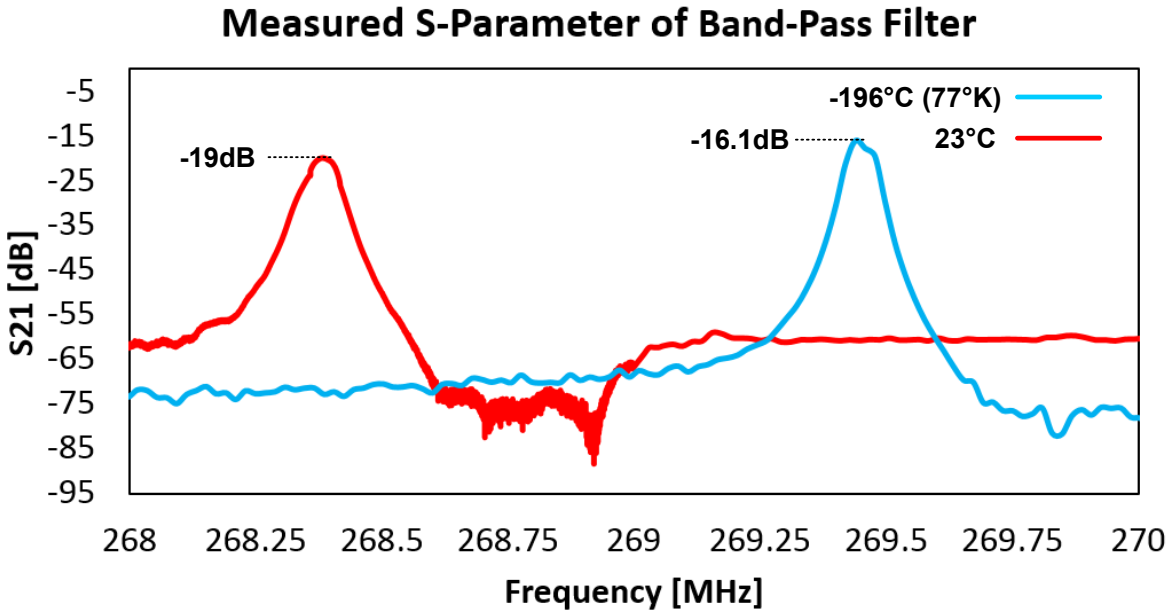

Figure 3-21: Measured S-parameter response for filter

Chapter 4

Switched Dual-Band SAW Filters Using Hybrid and Monolithically Integrated Vanadium Oxide Switches

4.1 Introduction

Current multi-band wireless frontend modules require switched filter banks that are constructed using a large quantity of discrete filters and switches at the input and output terminals to support different frequency bands which leads to increased module size, cost, and power consumption. Adaptive filtering solutions where different frequency channels can be added or removed while maintaining the smallest number of required elements and satisfying the performance requirements is desirable. A number of research studies have been conducted to explore the possibility of using reconfigurable BAW and SAW filter technologies [36], [47]. Integration of Phase Change Material (PCM) switches in the form of vias with a single Aluminum Nitride (AlN) piezoelectric resonator has been studied to achieve switching of the acoustic resonance mode [48]. However, the previously reported methods lack practical implementation and suffer from performance degradation. In this chapter we propose switched dual-band filtering solutions using piezoelectric SAW technology combined with Vanadium Dioxide (VO_2) based switches.

The main advantage of using VO_2 switches versus MEMS or semiconductor switches is that VO_2 switches are amenable to monolithic integration with SAW filters on a single chip. In this chapter, for the first time, we demonstrate both hybrid and monolithic integration of VO_2 switches with SAW resonators and filters using an in-house fabrication process. In the hybrid integration approach, the VO_2 switches are fabricated as discrete chips and are connected to the resonators within each filter using wire bonds. The use of wire bonds degrades the device performance and increases its size significantly. The monolithic integration of VO_2 switches allows us to implement higher order filters with a larger number of switches which results in overall improvement of filter's performance. We also address several performance characteristics of these switchable SAW resonators in terms of linear and high-power response.

4.2 Switched Dual-Band Filter Design

4.2.1 IHP-SAW Technology

The piezoelectric SAW technology used in this section to design and fabricate the proposed switchable filters is based on a multi-layered stack of $LiTaO_3/SiO_2/Si$, known as Incredible High-Performance SAW (IHP-SAW) technology [50]. Figure 4-1 shows the top and cross-section views of the SAW resonators. It consists of 300 nm thick interdigitated aluminum electrodes that are deposited over a $LiTaO_3/SiO_2/Si$ substrate [51]. The top Y-42° cut $LiTaO_3$ piezoelectric layer has a thickness of 900 nm and is deposited over a 900 nm thick SiO_2 layer. The high resistivity silicon substrate has a thickness of 525 μm. The use of multi-layered stack enables to confine the shear SAW (SH-SAW) acoustic modes within the $LiTaO_3$ piezoelectric layer and to prevent from acoustic energy loss through the silicon substrate. This results in a higher resonator quality (Q)

and better filter insertion loss. The main design parameters of the resonators are the dimensions and number of the aluminum electrodes as shown in Figure 4-1(a). COMSOL finite element simulation of a unit-cell consisting of four electrodes with equal electrode width and spacing (W = G = λ/4) is used to determine the resonance frequency and coupling coefficient.

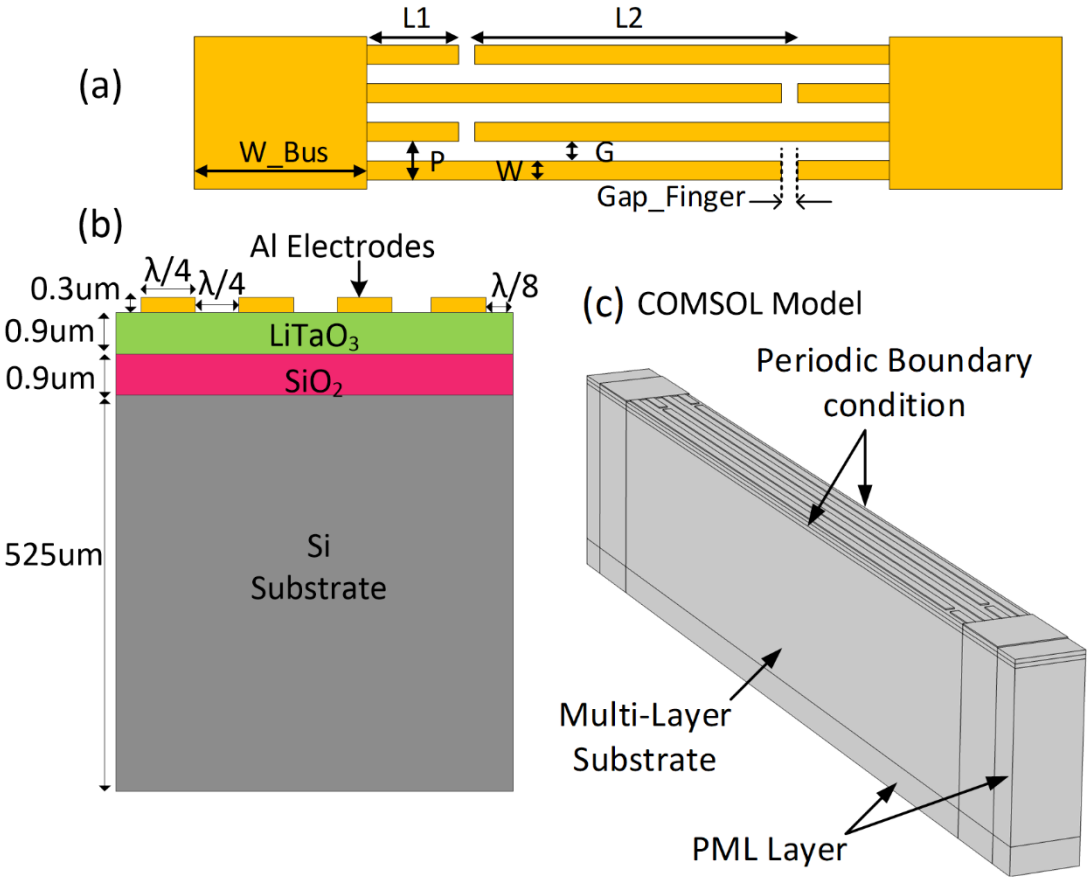

Figure 4-1: (a) Top view of the SAW resonator showing important design parameters, (b) cross-section view of the IHP-SAW resonator, and (c) 3D model of the unit cell used for FEM simulations.

Simulated S-parameters (S_{11}) and impedance of a piezoelectric resonator unit cell with four fingers and dimensions of W = G = 1.25 µm, P = 2.5 µm, L_1 = 5 µm, and L_2 = 100 µm are presented

in Figure 4-2. The resonance and anti-resonance frequencies of the resonator are F_S = 811 MHz and F_P = 859 MHz, respectively. The simulated effective coupling coefficient is Kt^2 = 13.8%.

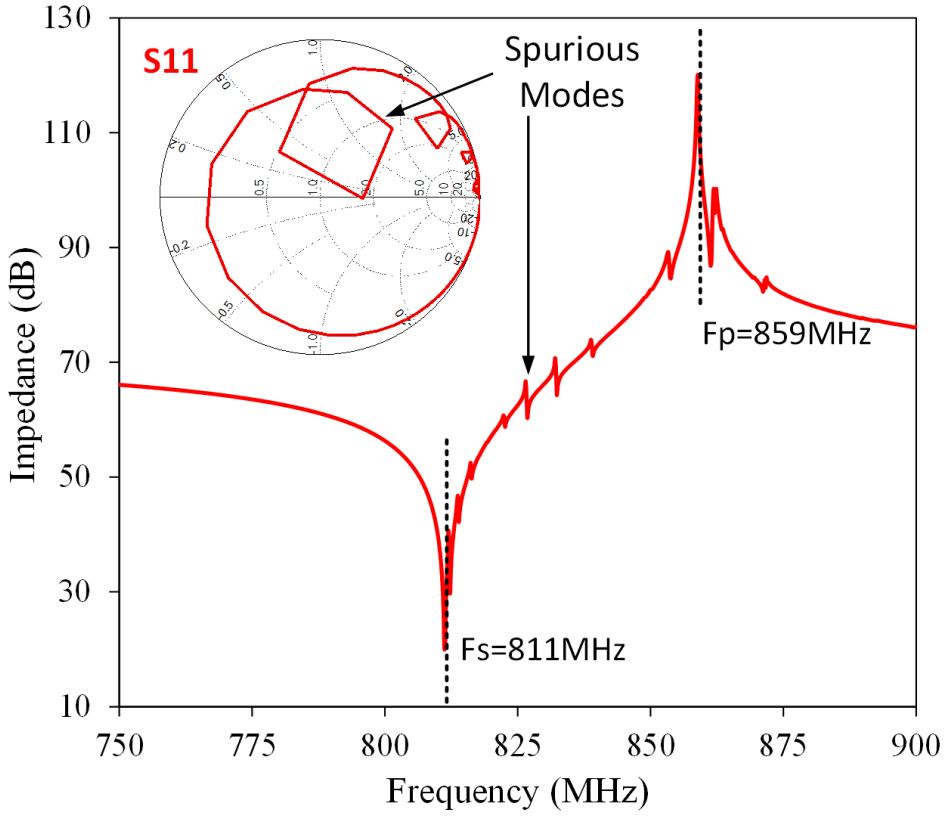

Figure 4-2: COMSOL simulated return loss (S_{11}) and impedance of a unit-cell with a pitch value of P = 2.5 µm, L_1 = 5 µm and L_2 = 100 µm.

The simulated frequencies and effective coupling coefficient values for different pitch values (P) are shown in Figure 4-3. These plots are used to determine dimensions of different resonators used in the filter design.

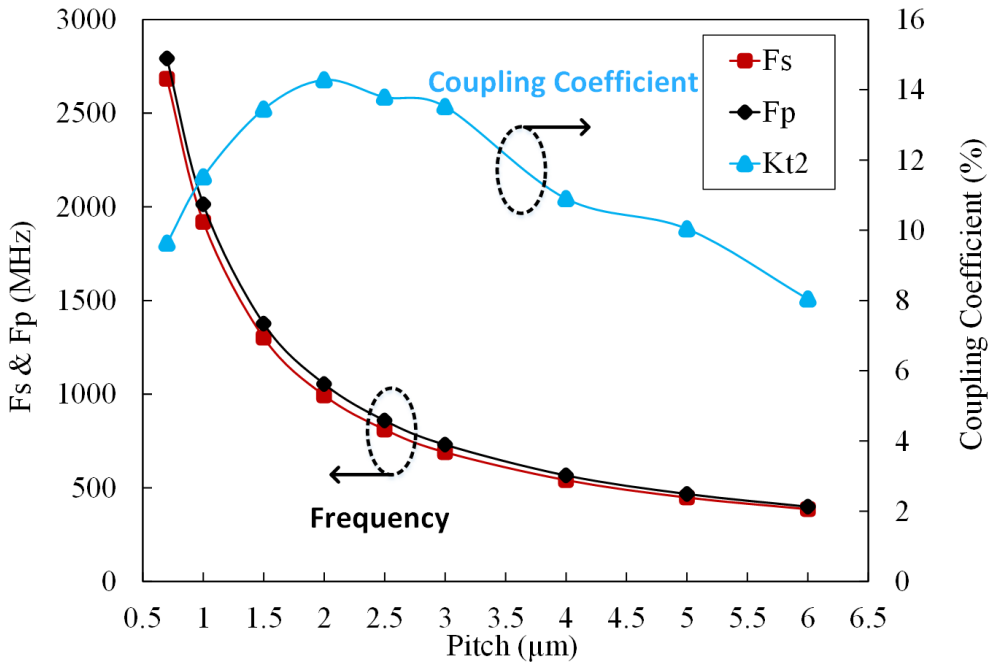

Figure 4-3: Simulated resonance (F_s) and anti-resonance (F_p) frequencies and coupling coefficient for different pitch values of the IHP-SAW resonator.

4.2.2 Measured data for array of fabricated resonators

The use of finite element modeling is beneficial in determining the critical dimensions of the IHP-SAW resonators such as the electrode spacing and dimensions of the interdigitated fingers during the initial stages of the resonator design. However an IHP-SAW resonator that is used to implement a filter consists of hundreds of electrodes and therefore, FEM modeling of an actual resonator is not practical. For this reason, an array of IHP-SAW resonators with different number of IDT electrodes (n = 50 to 1200) and electrode spacing (p = 2um to 4um), as shown in Figure 4-4, is fabricated.

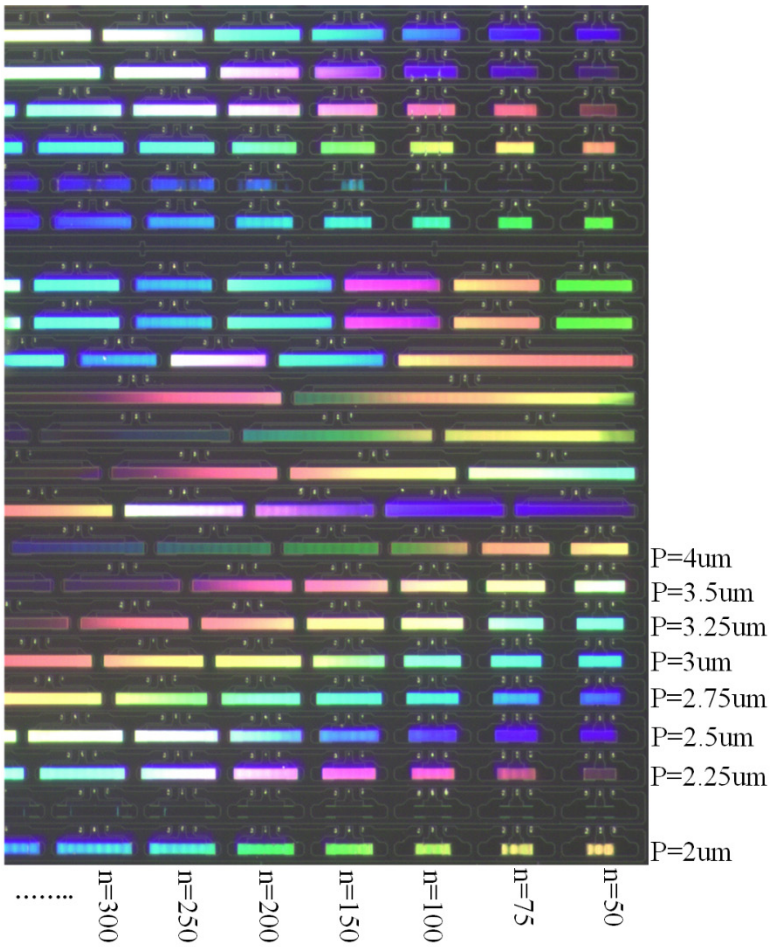

Figure 4-4: Array of fabricated IHP-SAW resonators with different number of IDT electrodes and pitch dimensions.

By creating a library of measurement data for the fabricated array of resonators we can find the required physical dimensions of the resonators with specific frequencies and impedances that are required for the implementation of the designed filters. Moreover, this measurement data can be used to create a parametric black-box model that can be utilized in a circuit simulation environment for filter design such as ADS software. The one-port S_{11} data of the array of resonators are collected using an automated probe station with temperature control. The measured data are analyzed using a MATLAB code that generates the parameters of the equivalent MBVD

circuit model for each resonator. The static capacitance value (C_0) versus the number of electrodes (n) is plotted in Figure 4-5.

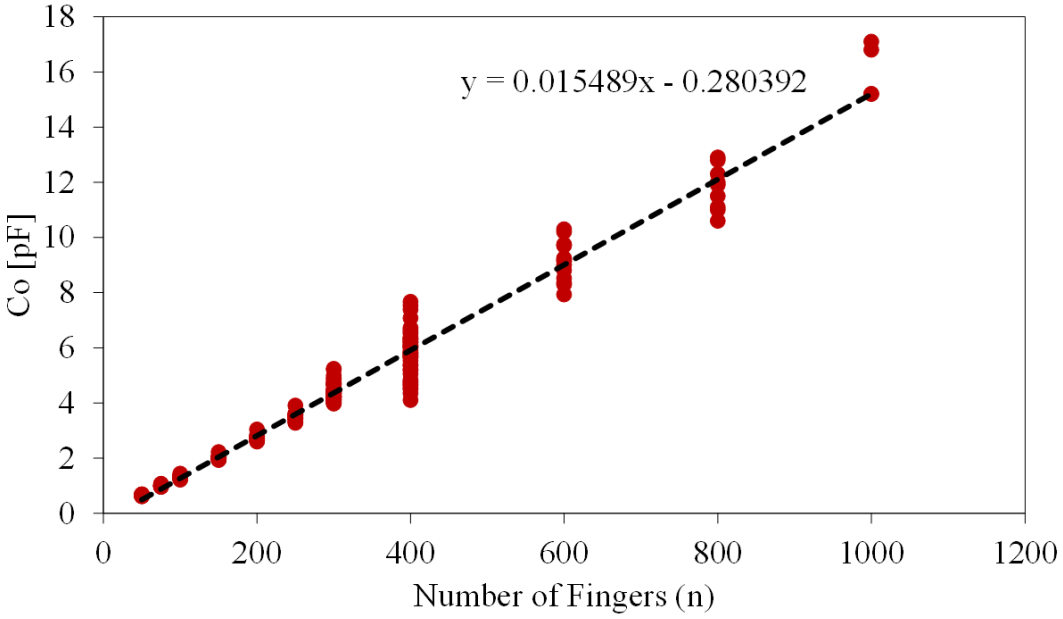

Figure 4-5: Static capacitance (C_0) versus the number of electrodes obtained from measured data for the fabricated array of resonators.

The measured anti-resonance frequency (F_p) as a function of resonator electrode spacing or pitch value (p) for different number of fingers are plotted in Figure 4-6 to Figure 4-8. To have a better accuracy, the array of resonators are divided into three groups based on the number of fingers n = 50 to n = 800.

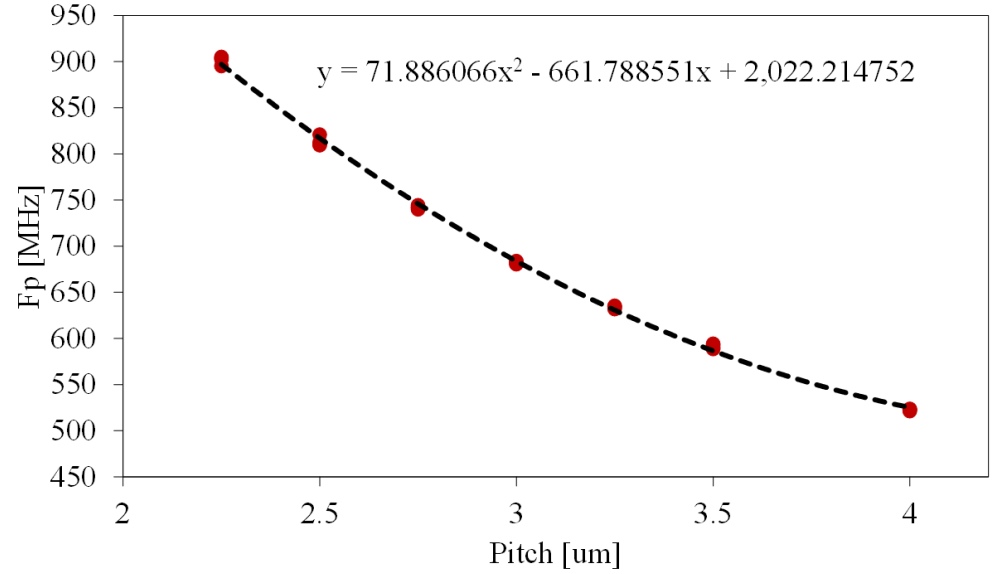

Figure 4-6: Anti-resonance frequency F_p versus pitch of the resonator for n = 50-100.

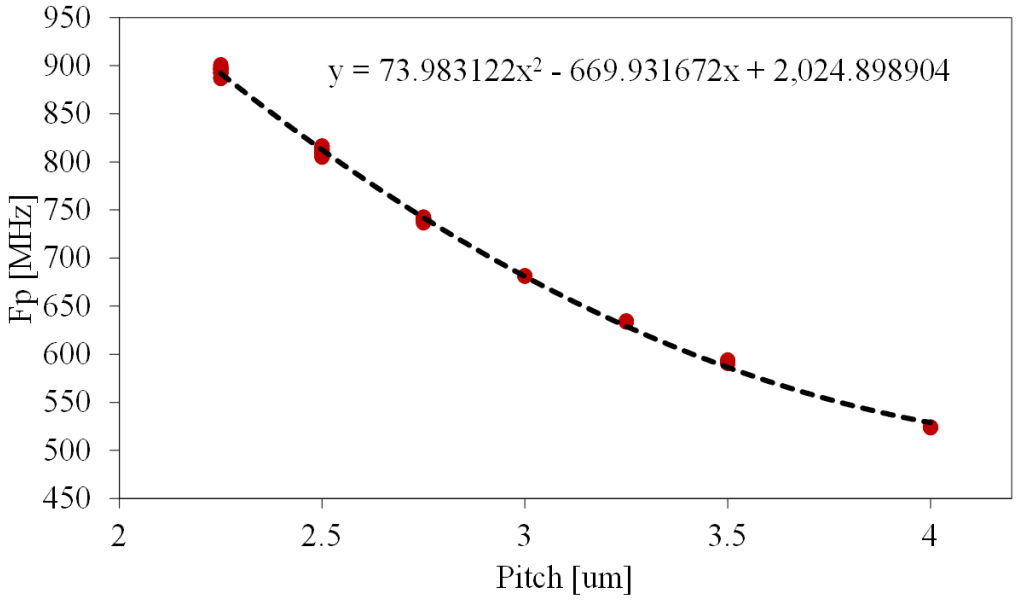

Figure 4-7: Anti-resonance frequency F_p versus pitch of the resonator for n = 250-300.

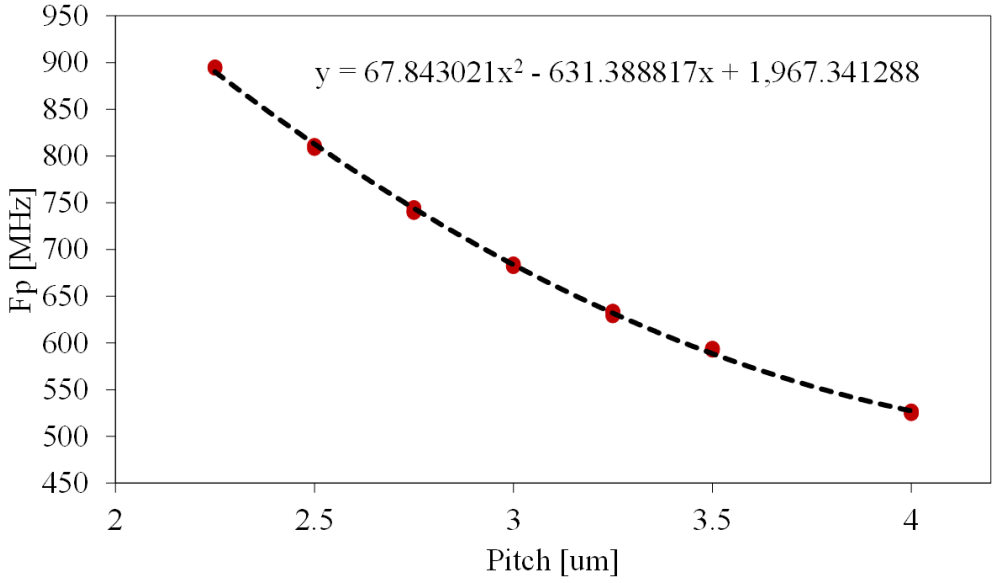

Figure 4-8: Anti-resonance frequency F_p versus pitch of the resonator for n = 600-800.

4.2.3 Design Procedure

The design of the filter is based on extracted pole technique and using the concept of coupling matrix. The complete design procedure, which is described in this section, is programmed in a MATLAB code where different filter specifications such as center frequency, bandwidth, required return loss, and order of the filter are used as the inputs and after processing these data, the code generates the equivalent BVD circuit model parameters of each series and shunt resonator within the filter.

A. Extraction of polynomials for low pass prototype filter

First step for design of the SAW bandpass filter is to specify the polynomials for a low pass prototype filter including P(s), F(s) and E(s) and subsequently to find the S-parameters for the filter according to equation (4.1). The real constant parameters (ε, ε_R) are used to normalize the polynomials [52].

$$[S]=\begin{pmatrix} S_{11} & S_{12} \\ S_{21} & S_{22} \end{pmatrix}=\frac{1}{E(s)}\begin{pmatrix} F(s)/\varepsilon_R & P(s)/\varepsilon \\ P(s)/\varepsilon & (-1)^N F(s)^*/\varepsilon_R \end{pmatrix} \quad (4.1)$$

The required input parameters that are used to extract the polynomials are the center frequency of the filter, bandwidth, return loss in the passband, order of the filter and location of transmission zeros. The designed filters in this study are fully canonical, that means the number of transmission zeros (order of P(s)) is equal to the order of the filter (N) or order of E(s) and F(s). The designed N^{th} order filter is a Chebyshev filter with a filtering function as shown in (4.2) [52]:

$$C_N=\cosh\left[\sum_{n=1}^{N}\cosh^{-1}(x_n(\omega))\right],\ x_n=\frac{\omega-1/\omega_n}{1-\omega/\omega_n} \quad (4.2)$$

The equation for x_n in (4.2) satisfies the following conditions for filtering function:

- There is a finite transmission zero at $\omega = \omega_n$ and also infinite transmission zeros at $\omega = \pm\infty$ while for both conditions we need to have $x_n(\omega) = \pm\infty$.
- At $\omega = \pm1$ which are the edges of the pass band, $x_n(\omega) = \pm1$.
- For the pass band where $-1 \leq \omega \leq 1$, we have $-1 \leq x_n(\omega) \leq 1$.

Another representation for filtering function is given in (4.4) which is obtained from unity condition expressed in (4.3):

$$E(s)E(s)^* = \frac{F(s)F(s)^*}{\varepsilon_R^2} + \frac{P(s)P(s)^*}{\varepsilon^2} \quad (4.3)$$

$$C_N(\omega) = \frac{\varepsilon F(\omega)}{\varepsilon_R P(\omega)} \quad (4.4)$$

Where P (ω) for a fully canonical filter is defined as follows:

$$P(\omega) = \prod_{n=1}^{N} (1 - \omega / \omega_n) \quad (4.5)$$

Since we know the location of transmission zeros (ω_n) based on design specifications, using this equation P (ω) can be obtained.

$C_N(\omega)$ can also be written as:

$$C_N(\omega) = \frac{1}{2}\left[\frac{\prod_{n=1}^{N}(c_n + d_n) + \prod_{n=1}^{N}(c_n - d_n)}{\prod_{n=1}^{N}(1 - \omega/\omega_n)}\right] \quad (4.6)$$

Where c_n and d_n are equal to:

$$c_n = (\omega - \frac{1}{\omega_n}), \quad d_n = \omega' \sqrt{1 - \frac{1}{\omega_n^2}} \quad (4.7)$$

$$\omega' = \sqrt{\omega^2 - 1} \quad (4.8)$$

The recursive technique is applied to find the numerator of C_N which specifies F (ω) according to (4.4). First we define the numerator of C_N (ω) in (4.6) using two polynomials: $G_N(\omega)$ and $G'_N(\omega)$ as expressed in (4.9)

$$Num[C_N(\omega)] = \frac{1}{2}[G_N(\omega) + G'_N(\omega)] \quad (4.9)$$

Where

$$G_N(\omega) = \prod_{n=1}^{N}[c_n + d_n], \quad G'_N(\omega) = \prod_{n=1}^{N}[c_n - d_n] \quad (4.10)$$

$G_N(\omega)$ can be presented with summation of two polynomials as presented in (4.11):

$$G_N(\omega) = U_N(\omega) + V_N(\omega) \quad (4.11)$$

Recursion starts with N = 1 and therefore for the first cycle, polynomials can be expressed as:

$$U_1(\omega) = \omega - \frac{1}{\omega_1}, \quad V_1(\omega) = \omega' \sqrt{1 - \frac{1}{\omega_1^2}} \quad (4.12)$$

By repeating the cycles for n=2, $G_2(\omega)$ is obtained as follows:

$$G_2(\omega) = G_1(\omega).\left[c_2 + d_2\right] = \left[U_1(\omega) + V_1(\omega)\right].\left[(\omega - \frac{1}{\omega_2}) + \omega' \sqrt{1 - \frac{1}{\omega_2^2}}\right] \quad (4.13)$$

$$= U_2(\omega) + V_2(\omega)$$

Therefore:

$$U_2(\omega) = \omega U_1(\omega) - \frac{U_1(\omega)}{\omega_2} + \omega' \sqrt{1 - \frac{1}{\omega_2^2}} V_1(\omega) \quad (4.14)$$

$$V_2(\omega) = \omega V_1(\omega) - \frac{V_1(\omega)}{\omega_2} + \omega' \sqrt{1 - \frac{1}{\omega^2}} U_1(\omega) \quad (4.15)$$

The general equations for the n^{th} cycle are equal to:

$$U_n = \omega U_{n-1}(\omega) - \frac{U_{n-1}(\omega)}{\omega_n} + \omega' \sqrt{1 - \frac{1}{\omega_n^2}} V_{n-1}(\omega) \quad (4.16)$$

$$V_n = \omega V_{n-1}(\omega) - \frac{V_{n-1}(\omega)}{\omega_n} + \omega' \sqrt{1 - \frac{1}{\omega_n^2}} U_{n-1}(\omega) \quad (4.17)$$

Similarly, by repeating the recursion process for $G'_N(\omega)$, we can find $U'_N(\omega) = U_N(\omega)$ and $V'_N(\omega) = -V_N(\omega)$. Therefore, numerator of $C_N(\omega)$ can be written as:

$$Num[C_N(\omega)] = \frac{1}{2}[G_N(\omega) + G'_N(\omega)]$$

$$= \frac{1}{2}[(U_N(\omega) + V_N(\omega)) + (U'_N(\omega) + V'_N(\omega))] = U_N(\omega) \quad (4.18)$$

According to (4.4) and using equation (4.18) we can find F (ω). P (ω) which is obtained from (4.5). Therefore, by knowing these two polynomials, real constants that are used for normalizing the polynomials in (4.1) for the filter with order of N can be calculated as follows:

$$\varepsilon = \frac{1}{\sqrt{10^{RL/10}-1}}\left|\frac{P(\omega)}{F(\omega)/\varepsilon_R}\right|_{\omega=\pm 1} \qquad (4.19)$$

Where RL is the return loss of the filter in dB that is defined as one of the specifications for the filter design as listed in Table 4.1. ε_R for a fully canonical filter can be calculated using equation (4.20) and when the number of transmission zeros is smaller than the order of the filter (N), ε_R is equal to unity.

$$\varepsilon_R = \frac{\varepsilon}{\sqrt{\varepsilon^2-1}} \qquad (4.20)$$

Until now, we found the polynomials of F(s), P(s) and also the real constants (ε, ε_R). Next step is to obtain the polynomial of E(s) using equation (4.3).

For a dual-band filter with the specifications listed in Table 4-1, E(s), F(s) and P(s) for each filter are found and presented in Table 4.2.

Table 4.1: Design specifications for low and high band filters of dual-band filter

Low Band Filter			
Filter Order	Center Frequency	Bandwidth	Return Loss
7	600MHz	30MHz	20dB

High Band Filter			
Filter Order	Center Frequency	Bandwidth	Return Loss
7	720MHz	36MHz	20dB

Table 4.2: Extracted polynomials for (a) low pass and (b) high pass filters

(a)

S^i, i	P(s)	F(s)	E(s)
0	j	1	1
1	1.61	-0.3213j	1.9637-0.3213j
2	14.83j	1.8076	3.7357-0.6422j
3	24.38	-0.5091j	4.1104-1.15061j
4	73.16j	0.9477	3.6754-1.2098j
5	122.42	-0.2088j	2.2191-0.9702j
6	120.09j	0.1279	0.9171-0.4946j
7	204.28	-0.0139j	0.1913-0.1413j
	ε=860.3622	ε_R=1	

(b)

S^i, i	P(s)	F(s)	E(s)
0	j	1	1
1	2.05	-0.2727j	1.9641-0.2727j
2	15.6j	1.8163	3.7452-0.5452j
3	30.52	-0.4321j	4.1296-0.9769j
4	75.41j	0.9593	3.7065-1.0273j
5	150.96	-0.1772j	2.2497-0.8239j
6	125.45j	0.1312	0.9376-0.42j
7	248.52	-0.0118j	0.1993-0.12j
	ε=1069.8	ε_R=1	

B. Synthesis of the filter based on extracted pole technique

The synthesis of the filter, as explained in this section, is based on extracted pole technique which has a better flexibility in comparison to other techniques in terms of adding transmission zeros to the filter response that controls the selectivity and out-of-band rejection level of the designed filter. Using this technique and by adding non resonant nodes (NRN) with in-line topology we can realize filters with maximum number of transmission zeros such as fully canonical filters without the need for coupling elements between the source and load ports. Also it has been shown in [53] that the use of in-line filter topology with NRNs that are coupled with dangling resonant nodes is an appropriate methodology for the implementation of RF filters using piezoelectric resonators.

Nodal representation of a 7-pole filter with inline topology that consists of resonant (RN) and non-resonant nodes (NRN) is shown in Figure 4-9. This topology represents a fully canonical filter with seven resonant nodes, seven non-resonant nodes and two additional NRNs. The first and last NRNs are used for phase adjustment at the input and output which is required for the implementation of a dual-band filter. These two NRNs at the output an input can be realized with a single inductor that are connected to the input and output ports. The procedure to find the required values for each inductor is explained with details in a later section.

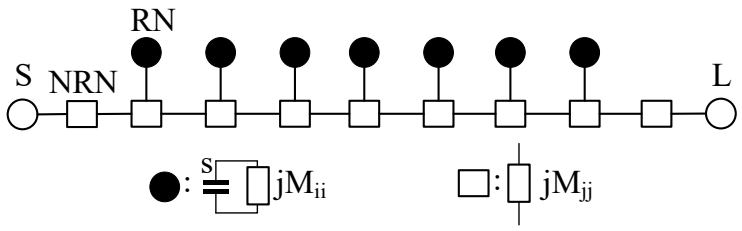

Figure 4-9: In-line topology for low pass filter with NRN nodes

In this topology, the resonant nodes shown with black filled circles, as shown in Figure 4-9, are modeled with unit capacitor in parallel with a frequency invariant admittance (M_{ii}) and empty squares which represent the NRNs are modeled with another admittance (M_{jj}) that are frequency invariant. The straight lines show the coupling between the resonators (M_{ij}) that is realized with admittance inverters. Based on the defined equivalencies for RNs and NRNs in Figure 4-9, it is evident that each dangling resonator creates a transmission zero at normalized frequency of s = -jM_{ii}.

In this section we follow the extracted pole technique for the synthesis of the filter using analytical expressions for the admittance of the sub-circuits within the filter at different scenarios. For a lossless two-port network, the reflection coefficients for the input and output have the same zeros and poles and only the phase is different as expressed using the following equations:

$$S_{11}(s) = e^{j\theta_{11}} \left|S_{11}(\infty)\right| \frac{\prod_{i=1}^{N}(s - s_{zi})}{\prod_{i=1}^{N}(s - s_{pi})} = e^{j\theta_{11}} \frac{M(s)}{D(s)} \qquad (4.21)$$

$$S_{22}(s) = e^{j\theta_{22}} \left|S_{22}(\infty)\right| \frac{\prod_{i=1}^{N}(s - s_{zi})}{\prod_{i=1}^{N}(s - s_{pi})} = e^{j\theta_{22}} \frac{M(s)}{D(s)} \qquad (4.22)$$

For normalized source and load impedances, input and output admittances are given by:

$$y_{in}(s) = \frac{1 - S_{11}(s)}{1 + S_{11}(s)} = \frac{D(s) - e^{j\theta_{11}} M(s)}{D(s) + e^{j\theta_{11}} M(s)} \qquad (4.23)$$

$$y_{out}(s) = \frac{1 - S_{22}(s)}{1 + S_{22}(s)} = \frac{D(s) - e^{j\theta_{22}} M(s)}{D(s) + e^{j\theta_{22}} M(s)} \qquad (4.24)$$

F(s), P(s) and E(s) are extracted in the previous section. Equation (4.1) is used to find M(s) and D(s) and equation (4.21) for considering the phase (Θ_{11}) and therefore we can evaluate S_{11}. Then

the input admittance can be obtained according to equation (4.23). As we discussed before, there are additional NRNs at the input and output that are used for phase adjustment. For evaluation of added phase using NRNs, the circuit diagram in Figure 4-10 is considered that represents the input/output of the filter topology shown in Figure 4-9.

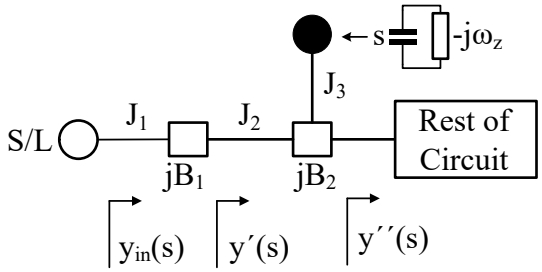

Figure 4-10: Equivalent circuit model of the filter seen from the input/output ports

The reflection coefficient is equal to:

$$S'_{11}(s) = e^{j\theta'_{11}} \frac{M(s)}{D(s)} = e^{j\theta_{11}} e^{j\theta_e} \frac{M(s)}{D(s)}, \quad \theta_e = \theta'_{11} - \theta_{11} \quad (4.25)$$

Where Θ_e is the adjusted phase which is a real number and Θ_{11} is the phase of S_{11} looking into the second NRN that is coupled with dangling resonator. The input admittance seen from the port is determined by:

$$y_{in}(s) = \frac{1 - S'_{11}(s)}{1 + S'_{11}(s)} = \frac{D(s) - e^{j(\theta_{11}+\theta_e)} M(s)}{D(s) + e^{j(\theta_{11}+\theta_e)} M(s)} = \frac{\frac{D(s)}{M(s)} - e^{j(\theta_{11}+\theta_e)}}{\frac{D(s)}{M(s)} + e^{j(\theta_{11}+\theta_e)}} \quad (4.26)$$

Since $y'(s=j\omega_z) = 0$ at the frequency of transmission zero which is added by a dangling resonator coupled with NRN shown in Figure 4-10, $S_{11}(s) = 1$ and according to equation (4.21):

$$e^{j\theta_{11}} = \frac{D(s)}{M(s)} \quad (4.27)$$

Therefore, equation (4.27) is substituted in (4.26) and the admittance seen from the port at frequency of transmission zero is given by:

$$y_{in}(s = j\omega_z) = \frac{1 - e^{j\theta_e}}{1 + e^{j\theta_e}} = -j\tan(\frac{\theta_e}{2}) \qquad (4.28)$$

In Figure 4-10, each NRN is represented by a frequency invariant reactance (FIR) which are B_1 and B_2. Therefore, y_{in} (s) is equal to:

$$y_{in}(s) = \frac{J_1^2}{jB_1 + y'(s)} \qquad (4.29)$$

Where y′(s) after FIR as shown in Figure 4-10 is:

$$y'(s) = \frac{J_2^2}{jB_2 + \frac{J_3^2}{s - j\omega_z} + y''(s)} \qquad (4.30)$$

According to this equation for $s = j\omega_z$, $y'(s) = 0$ which results in the following admittance value at the frequency of transmission zero using equation (4.29):

$$y_{in}(s = j\omega_z) = \frac{J_1^2}{jB_1} = -j\frac{J_1^2}{B_1} \quad (4.31)$$

From equation (4.28) and (4.31) we can conclude:

$$\tan(\frac{\theta_e}{2}) = \frac{J_1^2}{B_1} \quad (4.32)$$

For the design of a dual-band filter, impedance seen from the port of the high band filter at the center frequency of the low band filter needs to be infinity (open circuit) and the same condition for the low band filter at the center frequency of the high band filter should be fulfilled. Therefore, we can obtain the phase of reflection coefficient at the center frequency of the other filter by knowing that the reflection coefficient should be equal to one to satisfy an open circuit condition:

$$e^{j\theta_{11}} = \left.\frac{D(s)}{M(s)}\right|_{s=j\Omega_{dual}} = 1 \qquad (4.33)$$

Where Ω_{dual} is the center frequency of the low band or high band filters and Θ_{11} is null at these frequencies. After extraction of the filter's circuit parameters including B_1 which is discussed in next section, the required matching inductors are obtained from the following equation:

$$L = \frac{-Z_0}{2\pi f_0 B_1} \qquad (4.34)$$

C. Extraction of the filter elements

Synthesis of the filter is performed by extracting the filter elements one by one. This process needs consideration of three different cases for the sub-circuits of the filter with the in-line topology shown in Figure 4-9. The first case of the circuit extraction is shown in Figure 4-10 where we start the extraction from the source which is followed by an NRN used for phase adjustment and second NRN coupled with a dangling resonator. For this case we extract B_1 value for NRN using equation (4.31). Based on this equation B_1 value is obtained as follows:

$$B_1 = \mathrm{Im}\left[\left.\frac{J_1^2}{y_{in}(s)}\right|_{s=\omega_z}\right],\ y_{in} \leftarrow \frac{J^2}{y_{in}(s)} - jB_1 = y'(s) \qquad (35)$$

To find B_1, J_1 value should be known. Generally, values of conversion coefficients for only in-line admittance inverters (J values) including J_1 in this case, for simplicity are considered to be equal to unity.

The remainder of input admittances in (4.35) after removing J and B1 is $y_{in}=y'(s)$. By extracting the FIR value (B_1) for the first NRN, we continue the extraction for the following circuit as shown in Figure 4-11.

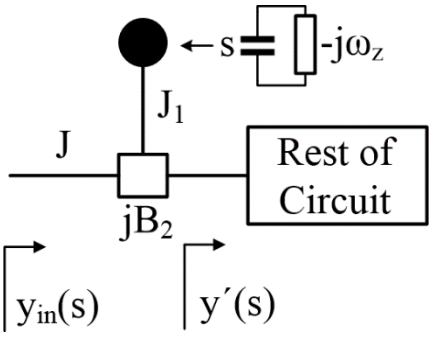

Figure 4-11: Second case of sub-circuits shows elements of the circuit that need to be extracted are J_1, B_2.

For the following circuit the input admittance is given by:

$$y_{in}(s) = \frac{J^2}{\frac{J_1^2}{s - j\omega_z} + jB + y'(s)} \quad (4.36)$$

Which can be expressed in another format as:

$$\frac{J^2}{y_{in}(s)} = \frac{J_1^2}{s - j\omega_z} + jB + y'(s) \quad (4.37)$$

Value of J_1 is obtained by finding the residue of equation (4.37) at frequency of the pole ($s = \omega_z$) as follows:

$$J_1^2 = J^2 \text{residue}\left(\frac{1}{y_{in}(s)}\right)\Bigg|_{s=j\omega_z} \quad (4.38)$$

Where, the value of J as discussed before is assumed to be unity. By knowing the values for J and J_1, the remainder input admittance can be expressed as:

$$y_{in}(s) \leftarrow \frac{J^2}{y_{in}(s)} - \frac{J_1^2}{s - j\omega_z} = jB + y'(s) \quad (4.39)$$

The first node in the rest of the circuit, as shown in Figure 4-11 is another NRN coupled with a dangling resonator that generates a transmission zero at $s = \omega_z'$. Therefore, the value of B and the remainder input impedance are obtained as follows:

$$B = \mathrm{Im}[y_{in}(s)|_{s=\omega_z'}], \quad y_{in}(s) \leftarrow y_{in}(s) - jB \qquad (4.40)$$

The circuit diagram for the third case shown in Figure 4-12 is the only remained part of the filter that needs to be extracted.

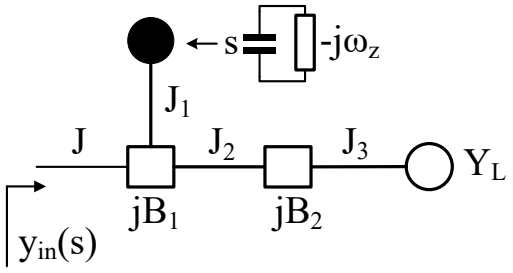

Figure 4-12: Third case of sub-circuits shows remaining circuit elements for extraction are J_1, J_2, J_3, B_1 and B_2.

The input admittance for the remained part is equal to:

$$y_{in}(s) = \frac{J^2}{jB_1 + \dfrac{J_1^2}{s-\omega_z} + \dfrac{J_2^3}{jB_2 + \dfrac{J_3^2}{Y_L}}} \qquad (4.41)$$

By considering J=1 or any arbitrary value, J_1 can be obtained as follows:

$$J_1^2 = J^2 \,\mathrm{residue}\left(\frac{1}{y_{in}(s)}\right)\Bigg|_{s=j\omega_z} \qquad (4.42)$$

Then remainder admittance can be expressed as:

$$y_{in}(s) \leftarrow \frac{J^2}{y_{in}(s)} - \frac{J_1^2}{s-j\omega_z} = jB_1 + \frac{J_2^2}{jB_2 + \dfrac{J_3^2}{Y_L}} \qquad (4.43)$$

And we can write the admittance as a complex number:

$$y_{in}(s) = \mathrm{Re}\left[y_{in}(s)\right] + j\,\mathrm{Im}[y_{in}(s)] = E + jF \qquad (4.44)$$

J_2 and J_3 can be any arbitrary value but we assume to be unity ($J_2 = J_3 = 1$) then for B_1 and B_2 we have:

$$B_2 = \pm\sqrt{\frac{1}{EY_L} - \frac{1}{Y_L^2}} \quad (45)$$

$$B_1 = F + B_2 E Y_L \quad (46)$$

B_2 can be either positive or negative and B_1 will have different values in these two cases but filtering function will be the same.

D. Representation of the filter with coupling matrix

Representation of the filter network using coupling matrix is a mathematical approach that shows all the couplings between the elements of the filter using a single matrix. Coupling matrix is a useful tool that can be used for studying the reconfiguration and transformation of the filter network by applying matrix operations [53]. For the filter circuit three different couplings are defined between the nodes that can be presented by submatrices as follows:

$M_{RR} \in \mathbb{R}^{R\times R}$: Coupling submatrix that presents the coupling between the resonant nodes. The diagonal elements of the matrix show the self-coupling for the resonant nodes.

$M_{NN} \in \mathbb{R}^{N\times N}$: Coupling submatrix that express the coupling between non-resonant nodes. In this classification source and load of the filter are considered as non-resonant nodes.

$M_{RN} \in \mathbb{R}^{R\times N}$: Coupling submatrix that shows the coupling between resonant and non-resonant nodes and it is generally non-square and asymmetric.

Based on these definitions for the comprising submatrices, the coupling matrix for the filter has an order of (R+N) × (R+N) as shown below:

$$M = \begin{pmatrix} M_{NN} & M_{RN} \\ M_{RN}^{T} & M_{RR} \end{pmatrix} \qquad (47)$$

The coupling matrices for the 7-pole low band and high band filters with specifications listed in Table 4.1 and using the described design procedure are obtained as follows:

$$\mathrm{M}=\begin{pmatrix}
0 & 0 & 1 & 0 & 0 & 0 & 0 & 0 & 0 & 0 & 0 & 0 & 0 & 0 & 0 & 0 \\
0 & 0 & 0 & 0 & 0 & 0 & 0 & 0 & 1 & 0 & 0 & 0 & 0 & 0 & 0 & 0 \\
1 & 0 & -1.7282 & 1 & 0 & 0 & 0 & 0 & 0 & 1.8602 & 0 & 0 & 0 & 0 & 0 & 0 \\
0 & 0 & 1 & 3.1493 & 1 & 0 & 0 & 0 & 0 & 0 & 2.5851 & 0 & 0 & 0 & 0 & 0 \\
0 & 0 & 0 & 1 & -2.9446 & 1 & 0 & 0 & 0 & 0 & 0 & 2.3766 & 0 & 0 & 0 & 0 \\
0 & 0 & 0 & 0 & 1 & 3.3218 & 1 & 0 & 0 & 0 & 0 & 0 & 2.6656 & 0 & 0 & 0 \\
0 & 0 & 0 & 0 & 0 & 1 & -2.9446 & 1 & 0 & 0 & 0 & 0 & 0 & 2.3766 & 0 & 0 \\
0 & 0 & 0 & 0 & 0 & 0 & 1 & 3.1493 & 1 & 0 & 0 & 0 & 0 & 0 & 2.5851 & 0 \\
0 & 1 & 0 & 0 & 0 & 0 & 0 & 1 & -1.7282 & 0 & 0 & 0 & 0 & 0 & 0 & 1.8601 \\
0 & 0 & 1.8602 & 0 & 0 & 0 & 0 & 0 & 0 & -2.2090 & 0 & 0 & 0 & 0 & 0 & 0 \\
0 & 0 & 0 & 2.5851 & 0 & 0 & 0 & 0 & 0 & 0 & 2.2827 & 0 & 0 & 0 & 0 & 0 \\
0 & 0 & 0 & 0 & 2.3766 & 0 & 0 & 0 & 0 & 0 & 0 & -1.9439 & 0 & 0 & 0 & 0 \\
0 & 0 & 0 & 0 & 0 & 2.6656 & 0 & 0 & 0 & 0 & 0 & 0 & 2.21265 & 0 & 0 & 0 \\
0 & 0 & 0 & 0 & 0 & 0 & 2.3766 & 0 & 0 & 0 & 0 & 0 & 0 & -1.9439 & 0 & 0 \\
0 & 0 & 0 & 0 & 0 & 0 & 0 & 2.5851 & 0 & 0 & 0 & 0 & 0 & 0 & 2.2827 & 0 \\
0 & 0 & 0 & 0 & 0 & 0 & 0 & 0 & 1.8601 & 0 & 0 & 0 & 0 & 0 & 0 & -2.2090
\end{pmatrix}$$

Figure 4-13: Coupling Matrix for the 7-pole low band filter

$$\mathrm{M}=\begin{pmatrix}
0 & 0 & 1 & 0 & 0 & 0 & 0 & 0 & 0 & 0 & 0 & 0 & 0 & 0 & 0 & 0 \\
0 & 0 & 0 & 0 & 0 & 0 & 0 & 0 & 1 & 0 & 0 & 0 & 0 & 0 & 0 & 0 \\
1 & 0 & -1.7668 & 1 & 0 & 0 & 0 & 0 & 0 & 1.8725 & 0 & 0 & 0 & 0 & 0 & 0 \\
0 & 0 & 1 & 3.9294 & 1 & 0 & 0 & 0 & 0 & 0 & 2.8915 & 0 & 0 & 0 & 0 & 0 \\
0 & 0 & 0 & 1 & -2.3941 & 1 & 0 & 0 & 0 & 0 & 0 & 2.1450 & 0 & 0 & 0 & 0 \\
0 & 0 & 0 & 0 & 1 & 4.0998 & 1 & 0 & 0 & 0 & 0 & 0 & 2.9642 & 0 & 0 & 0 \\
0 & 0 & 0 & 0 & 0 & 1 & -2.3941 & 1 & 0 & 0 & 0 & 0 & 0 & 2.1450 & 0 & 0 \\
0 & 0 & 0 & 0 & 0 & 0 & 1 & 3.9294 & 1 & 0 & 0 & 0 & 0 & 0 & 2.8915 & 0 \\
0 & 1 & 0 & 0 & 0 & 0 & 0 & 1 & -1.7668 & 0 & 0 & 0 & 0 & 0 & 0 & 1.8725 \\
0 & 0 & 1.8725 & 0 & 0 & 0 & 0 & 0 & 0 & -2.4247 & 0 & 0 & 0 & 0 & 0 & 0 \\
0 & 0 & 0 & 2.8915 & 0 & 0 & 0 & 0 & 0 & 0 & 2.2848 & 0 & 0 & 0 & 0 & 0 \\
0 & 0 & 0 & 0 & 2.1450 & 0 & 0 & 0 & 0 & 0 & 0 & -1.9507 & 0 & 0 & 0 & 0 \\
0 & 0 & 0 & 0 & 0 & 2.9642 & 0 & 0 & 0 & 0 & 0 & 0 & 2.1281 & 0 & 0 & 0 \\
0 & 0 & 0 & 0 & 0 & 0 & 2.1450 & 0 & 0 & 0 & 0 & 0 & 0 & -1.9507 & 0 & 0 \\
0 & 0 & 0 & 0 & 0 & 0 & 0 & 2.8915 & 0 & 0 & 0 & 0 & 0 & 0 & 2.2848 & 0 \\
0 & 0 & 0 & 0 & 0 & 0 & 0 & 0 & 1.8725 & 0 & 0 & 0 & 0 & 0 & 0 & -2.4247
\end{pmatrix}$$

Figure 4-14: Coupling matrix for the 7-pole high band filter

E. Low-Pass equivalent BVD model for resonators

For the realization of the filter using SAW resonators, we need to find a relationship between the extracted parameters of the filter with the in-line topology shown in Figure 4-9 and the low pass filter prototype using the BVD circuit model. To find the analogy between the BVD model and the extracted parameters, we divide them in two groups which are the series and shunt resonators based on the similarity that exists between the ladder type filter and the filter topology in Figure 4-9. Therefore, we can present the shunt resonator with a low-pass circuit model as shown in Figure 4-15 which consists of NRN coupled with dangling resonator.

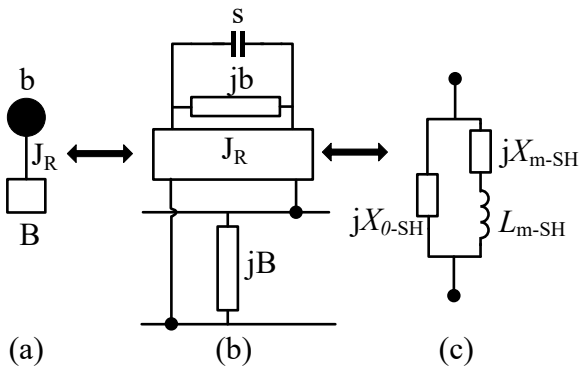

Figure 4-15: Nodal representation of a shunt resonator in (a); equivalent low-pass circuit model (b) and low-pass equivalent BVD model (c).

In the circuit diagram shown in Figure 4-15 (b), the resonant node is modeled with a unit capacitor parallel with a frequency invariant susceptance (jb) and NRN is modeled with another susceptance (jB) which is also frequency invariant. An admittance inverter represented with j_r is used to couple these two nodes. The low-pass equivalent BVD model for the shunt resonator is presented in Figure 4-15 (c) and circuit parameters of the BVD model are obtained by equating the input admittance for circuit (b) and the BVD model in (c) that results in the following equations:

$$L_{m-SH} = \frac{1}{J_R^2} \quad (4.48)$$

$$X_{m-SH} = \frac{b}{J_R^2} \quad (4.49)$$

$$X_{0-SH} = \frac{1}{B} \quad (4.50)$$

Nodal representation for the series resonator and its low-pass circuit model are presented in Figure 4-16. In addition to the NRN and coupled resonant node, nodal representation shows two connected admittance inverters to the left and right sides with opposite signs. For this circuit the equivalent low-pass BVD model is presented in Figure 4-16 (c).

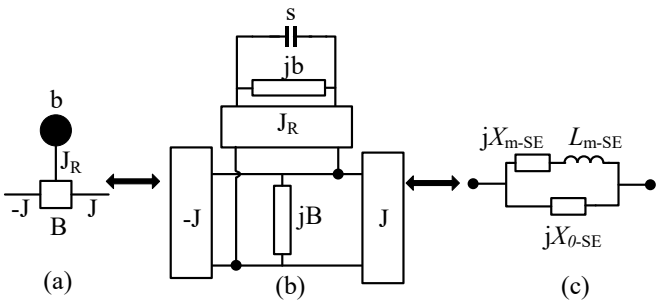

Figure 4-16: Nodal representation of series resonator in (a); low-pass circuit model for series resonator (b) and equivalent low-pass BVD model for series resonator (c).

The parameters of low-pass BVD circuit model for the series resonator can be obtained from following equations:

$$L_{m-SE} = \frac{B^2}{J_R^2 J^2} \quad (4.51)$$

$$X_{m-SE} = \frac{B}{J^2}\left(\frac{bB}{J_R^2} - 1\right) \quad (4.52)$$

$$X_{0-SE} = \frac{B}{J_R^2} \quad (4.53)$$

F. Low-Pass to bandpass transformation for BVD model

For the implementation of the filter, we need to find the elements of the BVD circuit model for each series and shunt resonator of the filter in the bandpass domain. Therefore, we need to transform the circuit model of the BVD models from low-pass domain to bandpass domain. In order to find a relationship between these two domains a frequency transformation is defined as follows:

$$\Omega = \alpha\left(\frac{\omega}{\omega_0} - \frac{\omega_0}{\omega}\right) \quad (4.54)$$

Where α is given by:

$$\alpha = \frac{\omega_0}{\omega_2 - \omega_1} \quad (4.55)$$

By equating the input impedance for the BVD model in low-pass and bandpass domains shown in Figure 4-17, a relationship between the elements of the BVD model in these two domains can be obtained as:

$$L_a = Z_0 \frac{(\alpha L_m + \frac{1}{2} X_m)}{\omega_0} \quad (4.56)$$

$$C_a = \frac{1}{Z_0} \frac{1}{\omega_0(\alpha L_m - \frac{1}{2} X_m)} \quad (4.57)$$

$$C_0 = -\frac{1}{Z_0} \frac{1}{\omega_0 X_0} \quad (4.58)$$

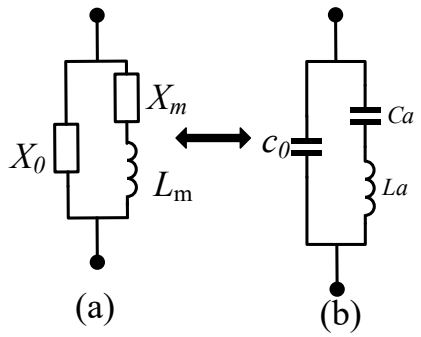

Figure 4-17: (a) Low-pass BVD model and (b) Bandpass BVD model

4.2.4 5-Pole Switched Dual-Band SAW Filter

A 5-pole switched dual-band filter is designed using SAW resonators and the described design procedure. Figure 4-18 shows the schematic diagram of the proposed filter. The frequency band associated with each channel, high-band or low-band, can be added or removed by actuating the VO_2 switches that are placed in parallel with the shunt resonators. The use of two VO_2 switches results in four possible states. The high-band and low-band filters are designed to have center frequencies of 940 MHz and 765 MHz, respectively and a return loss better than 20 dB within the passband. In the case of a dual-band filter, each channel filter is designed separately and then the input and output manifolds using transmission-line sections or LC lumped elements are designed. A perfect match at the center frequency of each filter is achieved by shifting the impedance of the counter band to an open circuit $Z_{HB}(f_{LB}) = Z_{LB}(f_{HB}) = \infty$. Careful consideration must also be taken in the design of the dual-band filter so as by switching each filter into a rejection state it does not affect the response of the other filter connected to the input and output manifolds. This is typically achieved by placing the bypassing switch in the middle shunt resonators, (SH_H_2) and (SH_L_2), as shown in Figure 4-18. This guarantees that the out of band reflected phase of one channel is not

affected while achieving isolation of the other channel when its middle resonator is detuned out of band.

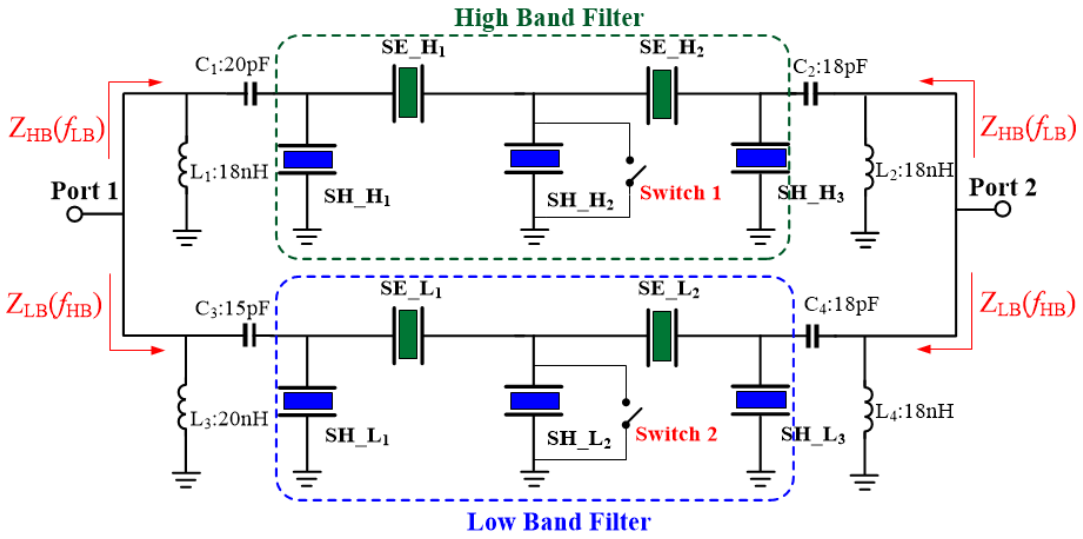

Figure 4-18: Circuit diagram of the 5-pole switched dual-band filter with SAW resonators, VO_2 switches and LC matching elements.

The main design parameters of the SAW resonators are obtained using the parameter extraction method discussed in previous section and using the measured data for SAW resonators. The extracted parameters and physical dimensions are listed in Table 4.3. Each filter is utilizing a VO_2 switch placed on the 2nd shunt resonators (SH_H_2) and (SH_L_2) as shown in Figure 4-18 which detunes the resonator by bypassing it to the ground and forcing the filter into the OFF state. The simulated S-parameter response of the designed dual-band filter when both channels are ON is shown in Figure 4-19. The simulated insertion loss is better than 3 dB in both bands with a return loss better than 20 dB. The simulation model includes the losses in the piezoelectric resonators and also in the LC matching elements.

Table 4.3: Design parameters for the 5-pole switched dual-band filter

High-Band Filter	SH_H_1	SE_H_1	SH_H_2	SE_H_2	SH_H_3
Fs (MHz)	897	941	880	941	901
Fp (MHz)	947	989	938	989	951
Pitch (μm)	2.124	2	2.15	2	2.114
# of electrodes (n)	124	85	630	88	146
Low-Band Filter	SH_L_1	SE_L_1	SH_L_2	SE_L_2	SH_L_3
Fs (MHz)	730	769	723	770	736
Fp (MHz)	772	809	765	810	778
Pitch (μm)	2.642	2.5	2.67	2.5	2.622
# of electrodes (n)	158	122	839	131	175

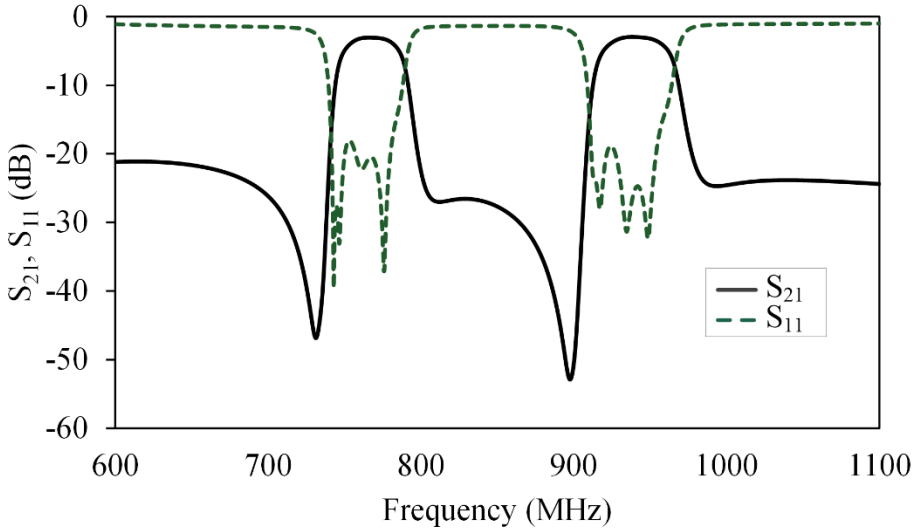

Figure 4-19: Simulated S-parameter response for switched dual-band 5-pole filter when both channels are ON.

4.2.5 7-Pole Switched Dual-Band SAW Filter

A 7-pole switched dual-band filter is designed with lower and upper frequency channels at 600 MHz and 725 MHz, respectively. The lower band filter has a bandwidth of 30 MHz, while the upper band filter has a bandwidth of 36 MHz. The bandwidth of each filter is selected based on the technological limitations of the SAW resonators in terms of maximum achievable coupling coefficients (Kt^2) at each frequency band. The filter polynomials are obtained using the filter specifications. The coupling matrix of each filter is extracted from these polynomials [52]. Figure 4-20 shows the theoretical S-parameter response for each filter as obtained from the coupling matrix.

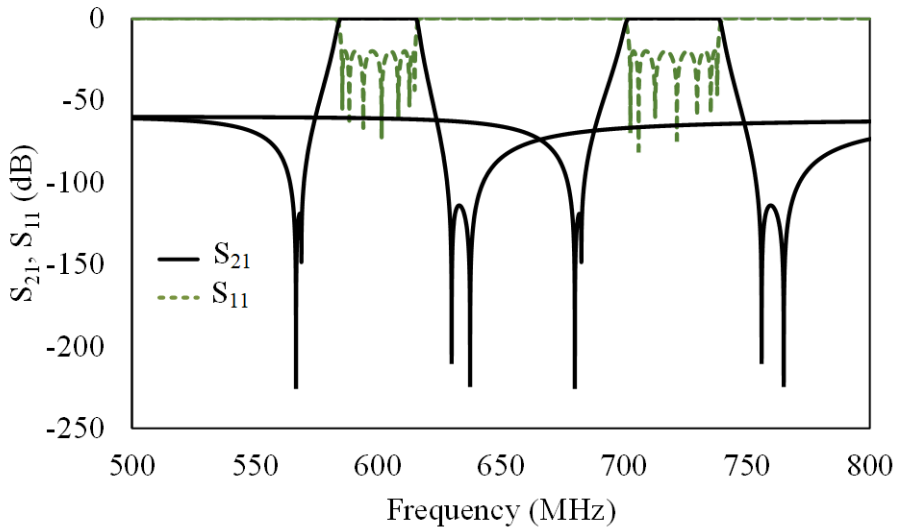

Figure 4-20: Theoretical S-parameter response of the 7-pole switched dual-band filter.

A schematic circuit diagram of the filter is presented in Figure 4-21. Each filter consists of four series and three shunt resonators and there are VO_2 switches connected in parallel with each shunt

resonator. The OFF state of each channel can be achieved by detuning only one, two or all three of the shunt resonators and by actuating the corresponding VO_2 switches separately.

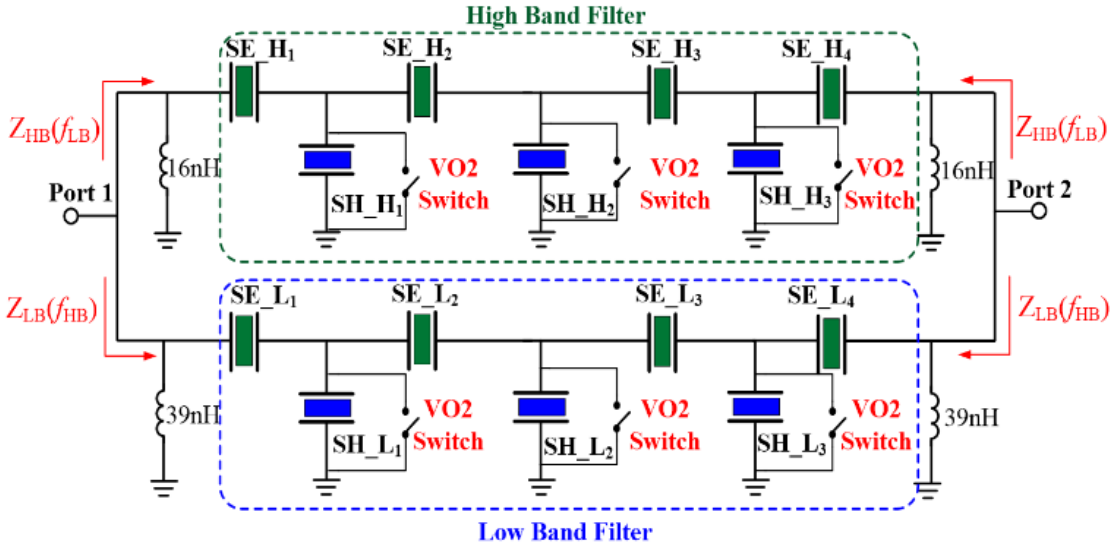

Figure 4-21: Circuit diagram of the 7-pole switched dual-band filter.

The use of a larger number of shunt resonators and VO_2 switches results in a better isolation performance for the OFF state of each channel. It should be noted that placing the switches on the manifold rather than within the filter will disturb the phase balance at the junction causing degradation of the other filter channel performance. This is why the switches are integrated within the resonators, since detuning the resonators in one channel will have only slight impact on the phase balance, and consequently less impact on the performance of the other channel. The physical design parameters of the series and shunt resonators such as resonance frequencies, pitch, and number of fingers are obtained by the parameter extraction technique discussed in section 4.2.4 and fitting the measured data for the fabricated array of resonators to the equivalent BVD circuit model of each resonator in the filter. The main design parameters of the designed 7-pole switchable dual-band filter are listed in Table 4.4.

Table 4.4: Design parameters for the 7-pole switched dual-band filter

High-Band Filter	SH_H_1	SE_H_1	SH_H_2	SE_H_2
Fs (MHz)	680	728	683	721
Fp (MHz)	717	763	720	754
Pitch (μm)	2.836	2.652	2.823	2.687
# of electrodes (n)	1117	183	1164	142
Low-Band Filter	SH_L_1	SE_L_1	SH_L_2	SE_L_2
Fs (MHz)	567	603	569	600
Fp (MHz)	598	632	600	628
Pitch (μm)	3.484	3.282	3.472	3.297
# of electrodes (n)	1075	219	1133	139

$SE\_H_3=SE\_H_2$, $SH\_H_3=SH\_H_1$, $SE\_H_4=SE\_H_1$
$SE\_L_3=SE\_L_2$, $SH\_L_3=SH\_L_1$, $SE\_L_4=SE\_L_1$

The simulated S-parameter response for the ON state of both channels where the resonators and matching inductors are assumed to be lossless is presented in Figure 4-22 (a). The simulated S-parameters including all the losses in the SAW resonators, electrode connections between the resonators, and matching inductors is shown in Figure 4-22 (b). Insertion losses are 3.4 dB and 3.5 dB for the lower and upper channels, respectively while the return loss is better than 15 dB for both channels. Figure 4-22 (c) shows simulated S-parameters when the lower channel is turned OFF by detuning only the 2nd shunt resonator. An isolation of better than 20 dB is achieved while there is almost no impact on the transmission response of the upper channel. It is possible to obtain an isolation better than 40 dB by detuning all three shunt resonators within the lower channel filter as shown in Figure 4-22 (d).

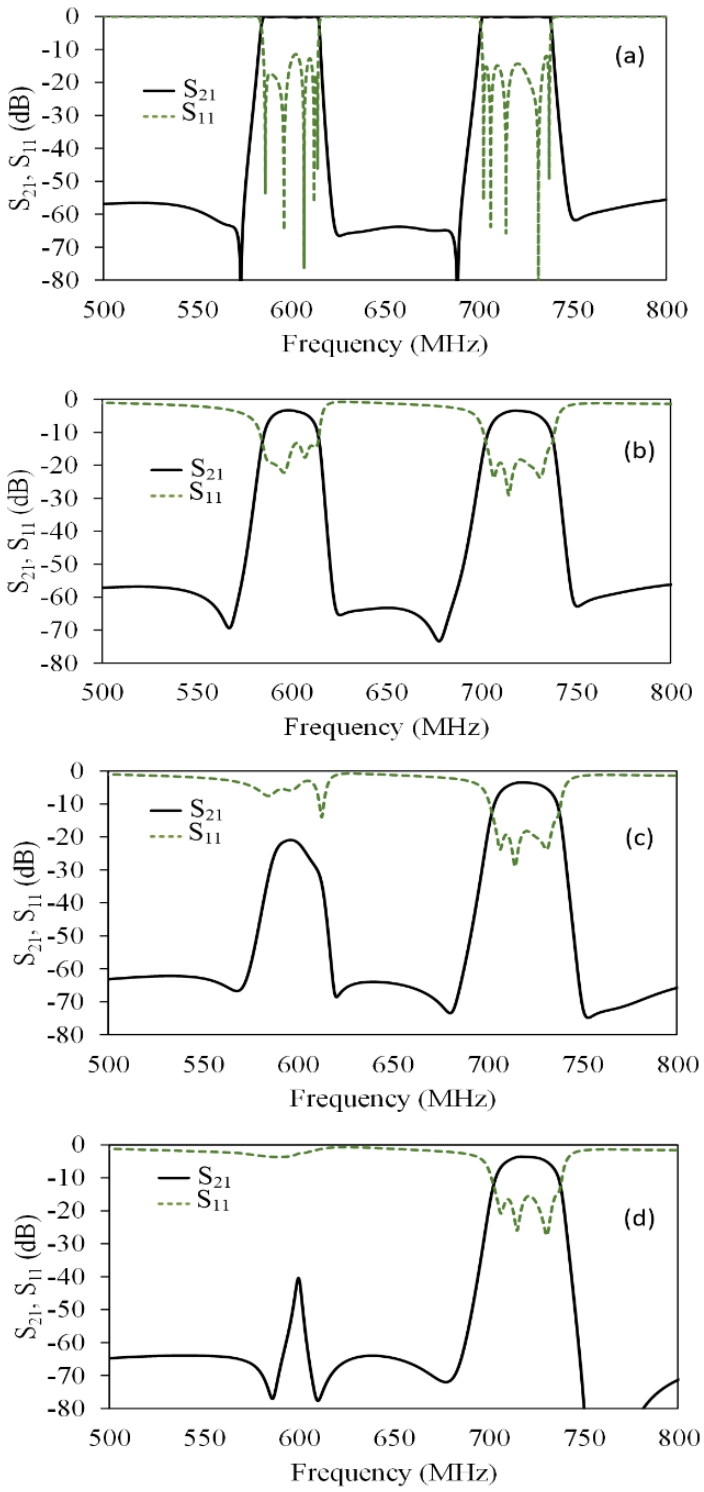

Figure 4-22: Simulated S-parameter response of the 7-pole switched dual-band filter when (a) both channels are ON and without any losses, (b) both channels are ON with losses included in the model, (c) lower channel is turned OFF by detuning middle shunt resonator, and (d) by detuning all shunt resonators.

4.3 Hybrid Integration

The Initial implementation of the designed 5-pole switched dual-band filter in section 4.2.4 is based on discrete VO_2 switches integrated with SAW resonators using wire bonds [49]. The VO_2 switches are fabricated on an alumina substrate using an in-house fabrication process at the CIRFE lab at the University of Waterloo. The switches are turned on by applying a DC bias voltage on the heater element and transition of the VO_2 layer from insulator to conducting state by the increase in temperature. The SAW chip containing the high-band and low-band filters is fabricated on a multi-layered $LiTaO_3/SiO_2/Si$ substrate. The LC matching elements were also assembled on the SAW chip and hybrid integration of the SAW chip with VO_2 switches on an alumina carrier substrate was used to implement the filter as shown in Figure 4-23. The limitations of the hybrid integration in terms of size and ease of assembly allows the use of only a limited number of switches. In this case only two VO_2 switches were placed in parallel with the 2^{nd} shunt resonators of each filter using wire bonds.

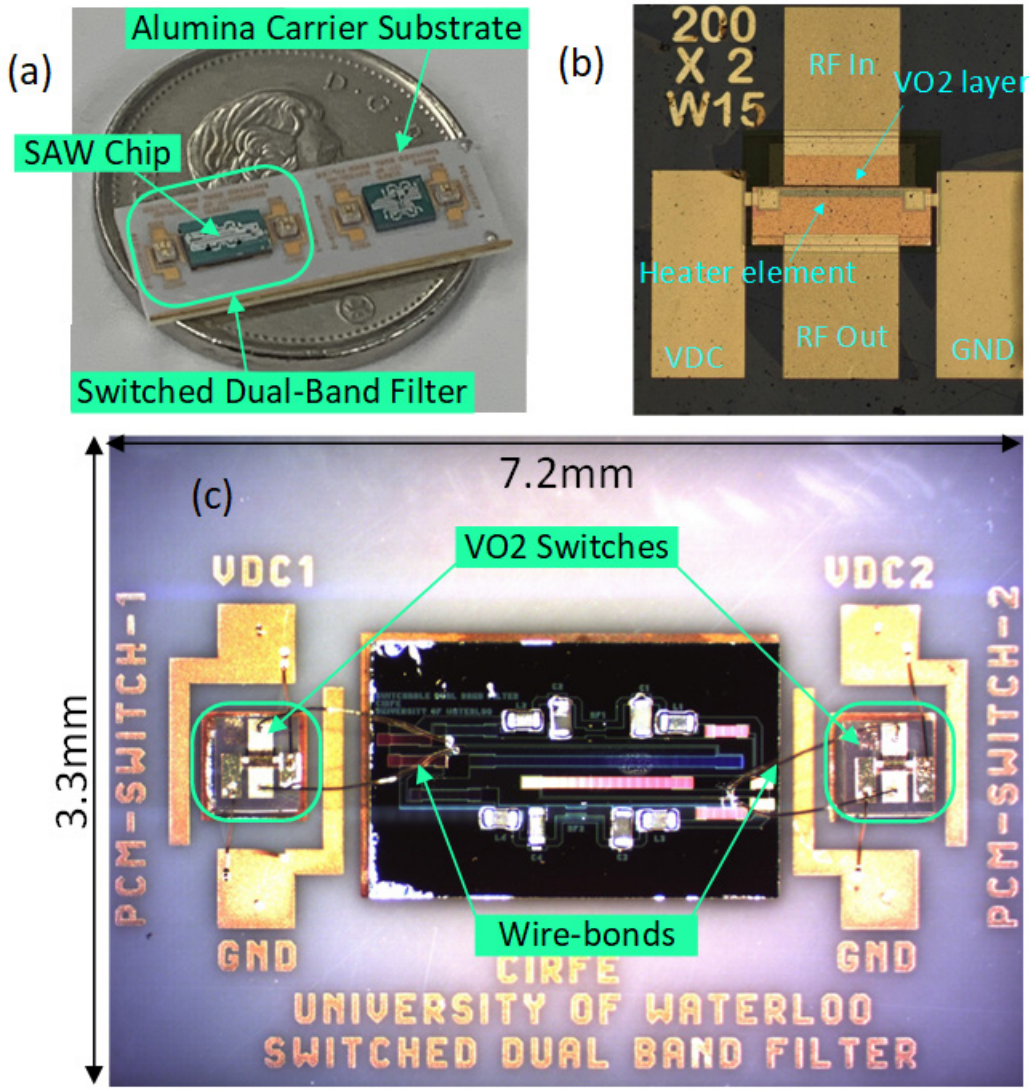

Figure 4-23: (a) Hybrid integration of the SAW filters and VO_2 switches on an alumina carrier substrate, (b) image of the discrete VO_2 switches, (c) close-up view of the switched dual-band filter with LC matching and VO_2 switches connected with wire bonds.

The measured S-parameters of the implemented switched dual-band filter are shown in Figure 4-24, for four different states of the filter. When both channels are ON, the dual-band filter has an insertion loss of 3.7 dB at 765 MHz and 3.9 dB at 935 MHz. The isolation when both filters are turned OFF is better than 9.8 dB for both high and low channels. There are small differences between the measured and simulated filter response in terms of center frequency and insertion loss, which are attributed to fabrication tolerances.

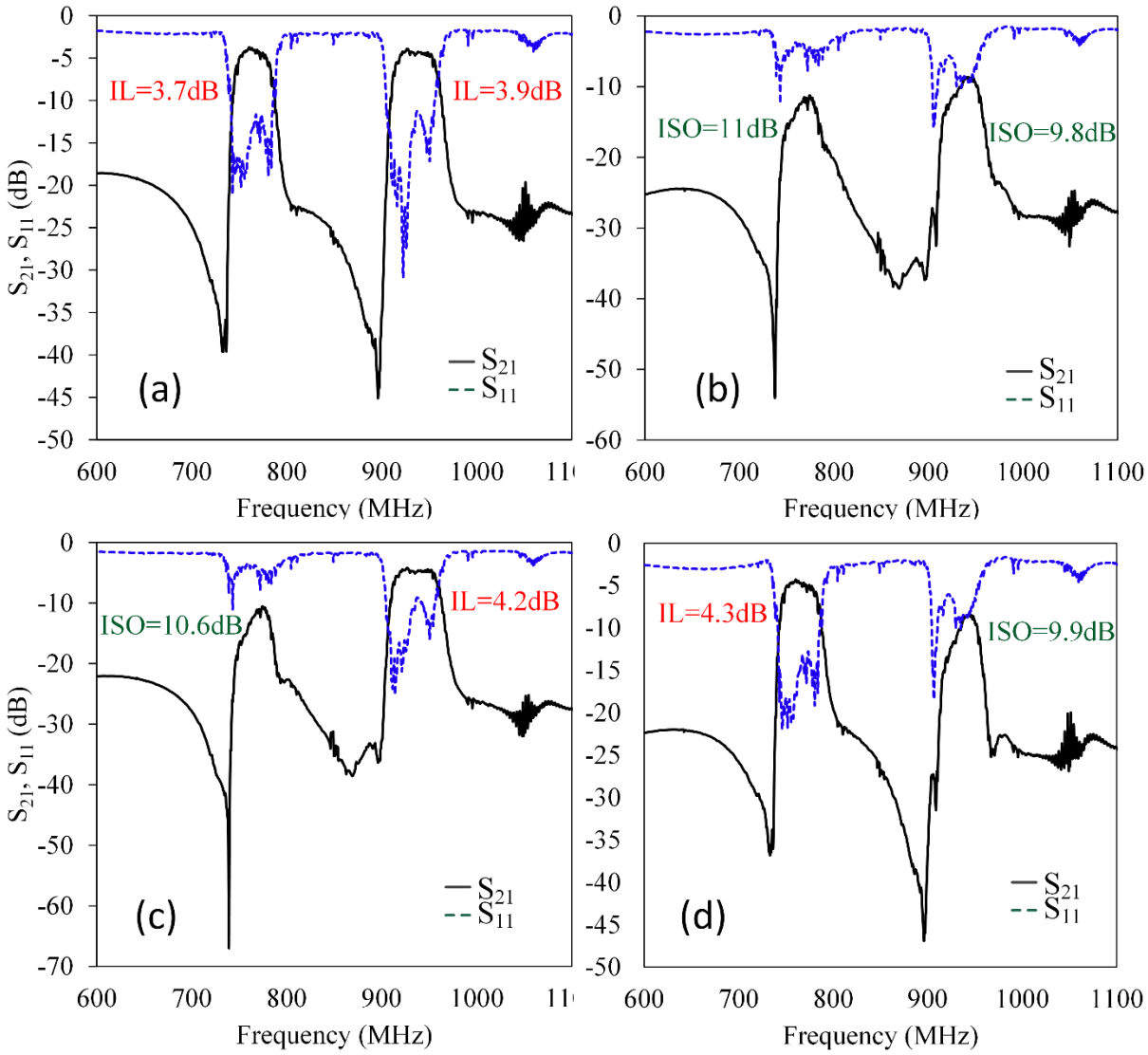

Figure 4-24: Measured S-parameter response of the 5-pole switched dual-band filter (a) when both channels are ON, (b) both channels are OFF, (c) only high channel is ON and (d) only low channel is ON.

Figure 4-25 shows a comparison between simulated and measured isolation when both low and high channels are turned OFF. The simulated isolation of the OFF channel is around 20 dB, while the measurement shows 9.8 dB of isolation. The degradation in the isolation performance of the 5-pole filter with hybrid integration of VO_2 switches is due to the parasitic inductance of the wire bonds used to connect the VO_2 switches. The use of monolithic integration of the VO_2 switches

on the SAW die eliminates the need to use wire bonds, and significantly enhances the isolation performance as will be discussed in the next section.

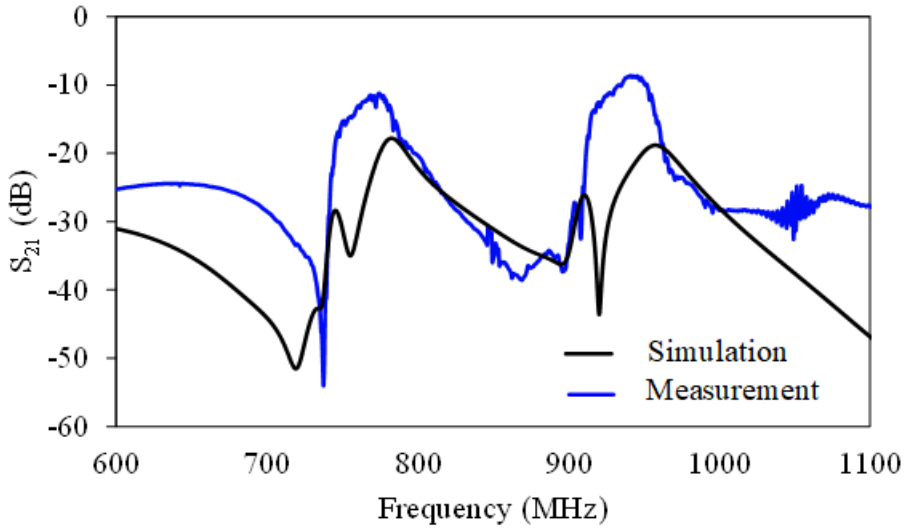

Figure 4-25: Simulated and measured isolation performance of the dual-band filter when both channels are turned off.

4.4 Monolithic Integration of VO_2 Switches

As shown in the measured data of the implemented switched dual-band filter using hybrid integration with the wire bonds, the parasitic effects of the wire bonds degraded the isolation performance for the OFF states of the channels. In addition, using discrete VO_2 switches it is possible to use only a limited number of switches due to size limitations and the complexity of assembly. In this section we are demonstrating monolithic integration of the VO_2 switches with the SAW filter, which results in significant improvement in filter performance in addition to reduced size, and ease of manufacturing for practical implementation of the proposed switched dual-band filters [54].

4.4.1 Fabrication Process

Figure 4-26 shows the processing steps for monolithic integration of the VO_2 switches with the SAW resonators. A 300 nm VO_2 layer was first deposited using a Pulsed Laser Deposition (PLD) system [55], [56] over the multi-layered $LiTaO_3/SiO_2/Si$ substrate. The rest of the fabrication process was carried out at the CIRFE Lab clean room at the University of Waterloo [57]. The deposited VO_2 layer is patterned using wet etching followed by 300 nm deposition of Al electrode layer using e-beam evaporation. The metal electrodes are patterned using metal RIE. During the next step a 200 nm silicon-nitride dielectric layer is deposited using low temperature PECVD at 150°C. The silicon nitride dielectric layer is required to have a good thermal conductivity in order to transfer most of the heat generated in the top Cr heater down to the VO_2 layer for an efficient operation of the VO_2 switches with the lowest possible DC power consumption. The silicon nitride dielectric layer is patterned using RIE and during the last processing step a 150 nm layer of Cr is deposited by e-beam evaporation and patterned using lift-off to form the heaters.

The performance of the VO_2 switches in terms of resistance ratio (R_{OFF}/R_{ON}) mainly depends on the quality of the deposited VO_2 film. Figure 4-27(a) shows the measured surface morphology of the deposited VO_2 layer using AFM which is around 4 nm [55]. The measured change in resistivity versus temperature for both heating and cooling cycles are also presented in Figure 4-27(b). A resistivity variation of 3 orders of magnitude (1.92 Ω.cm to 2×10^{-3} Ω.cm) is achieved with a transition temperature around 62°C and 64°C for the cooling and heating cycles, respectively.

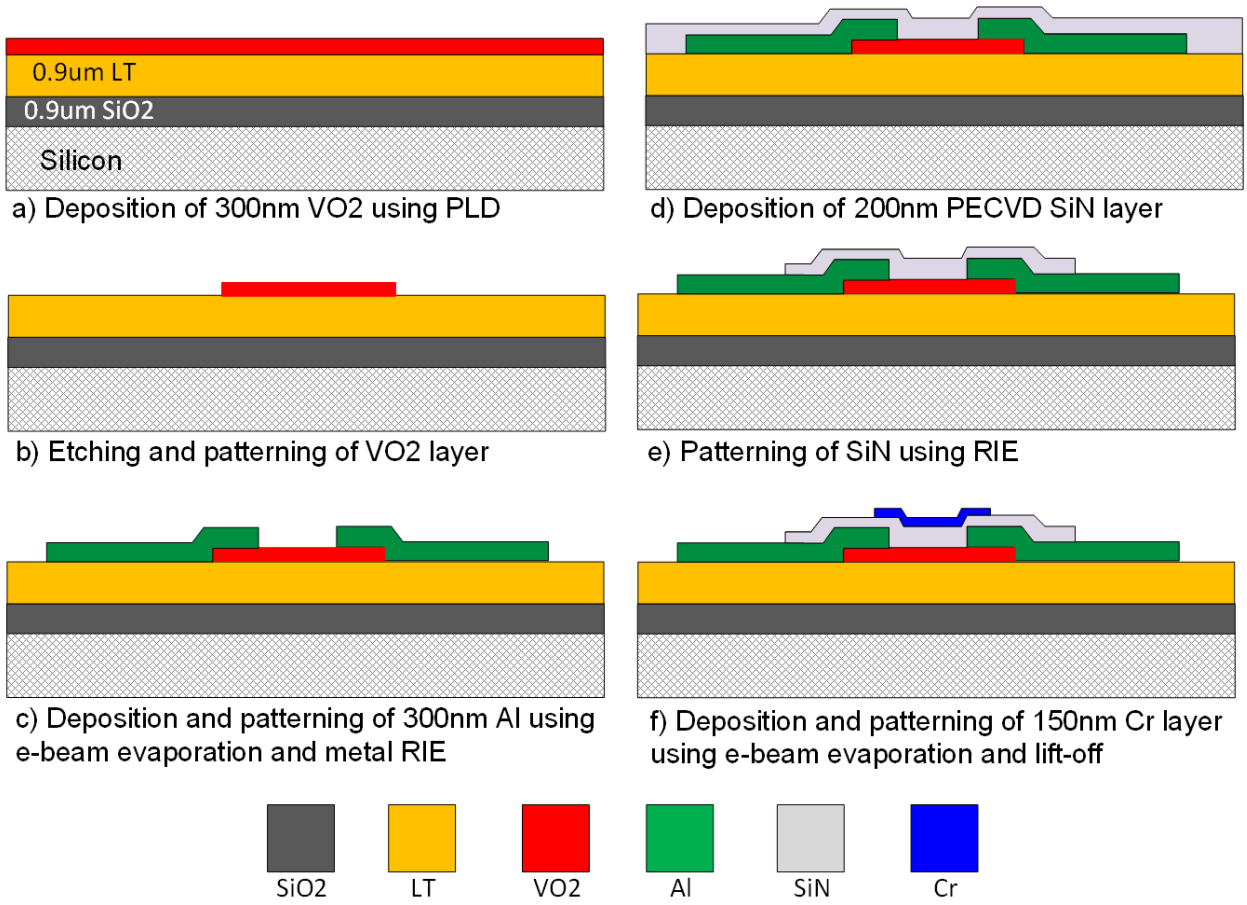

Figure 4-26: Fabrication process for monolithic integration of the VO_2 switches with SAW resonators and filters.

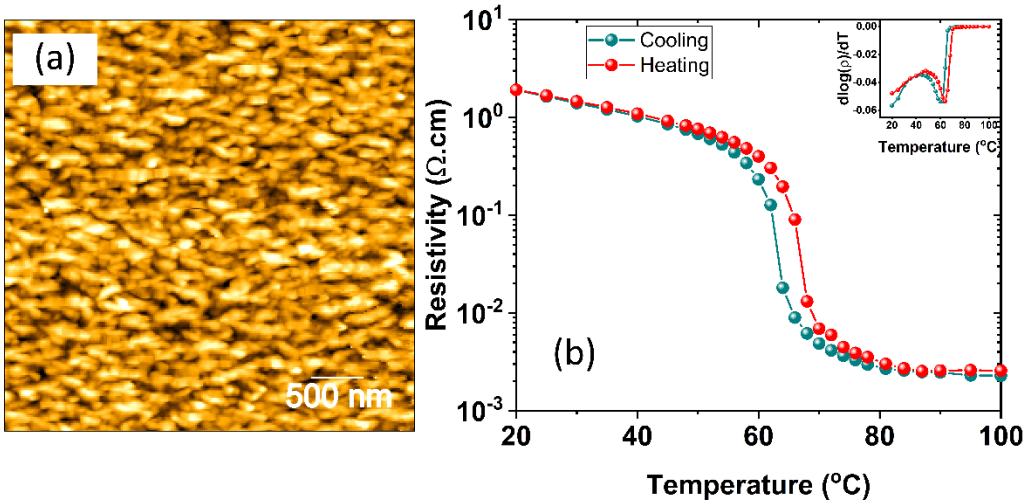

Figure 4-27: (a) Surface morphology and (b) change in resistivity for the 300 nm VO_2 layer deposited using PLD method.

4.4.2 VO_2 Switch

An optical image of the fabricated VO_2 switch along with the critical dimensions of the switch is shown in Figure 4-28. The DC resistance of the switch between the input and output aluminum electrodes is measured versus the applied DC bias voltage on the Cr heater element as shown in Figure 4-29.

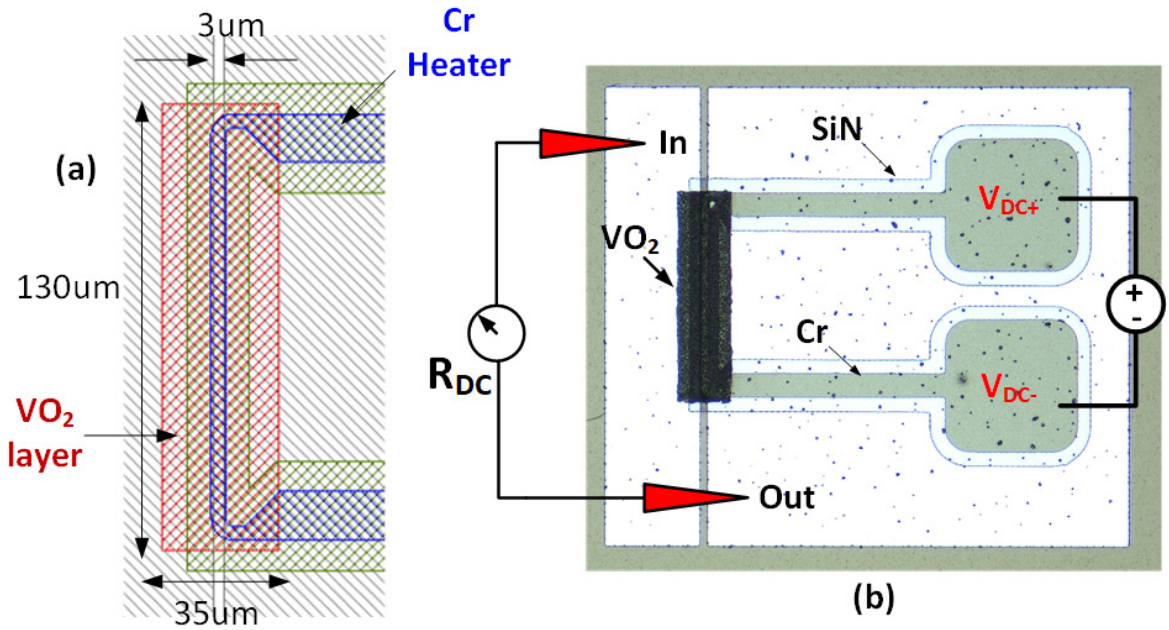

Figure 4-28: (a) Critical dimensions and (b) optical image of the fabricated VO_2 switch.

The switch turns ON when the applied DC bias voltage is larger than 2 V and the measured resistance values for the ON and OFF states of the switch are R_{ON} = 3 Ω and R_{OFF} = 1.47 kΩ, respectively which results in a resistance ratio of ~500. The resistance ratio can be further enhanced by optimizing the PLD deposition process and by improving the quality of the VO_2 layer and also by optimizing the dimensions of the switch junction.

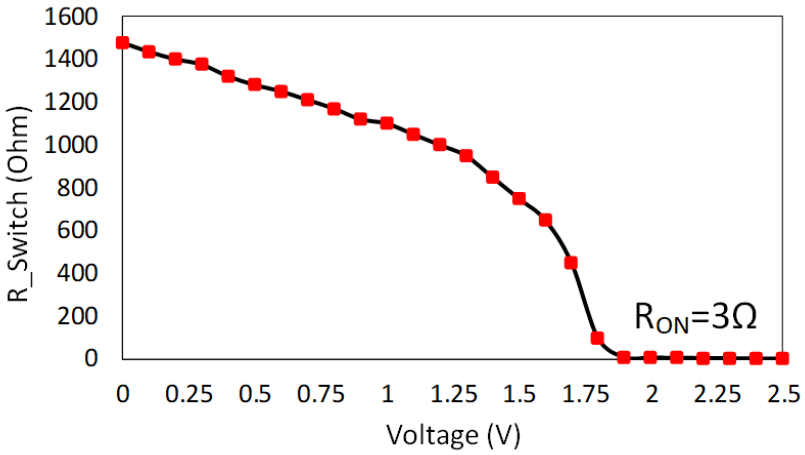

Figure 4-29: Measured resistance of the fabricated VO_2 switch versus applied DC bias voltage.

FEM simulations in COMSOL were performed to predict the transient response and switching time of the VO_2 switches. A pulse DC bias voltage with duration of 5 µs was applied on the heater element and the temperature of the hottest point of the VO_2 material is plotted as shown in Figure 4-30. The amplitude of the DC bias voltage was swept from 2 V to 3.5 V with 0.5 V steps. As shown in Figure 4-30(d), a voltage amplitude of 2.5 V is required in order to turn the switch ON with a switching time of around 2 µs. The switching time can be reduced significantly with the use of a higher actuation voltage. The required DC current is 54 mA resulting in a 135 mW power consumption.

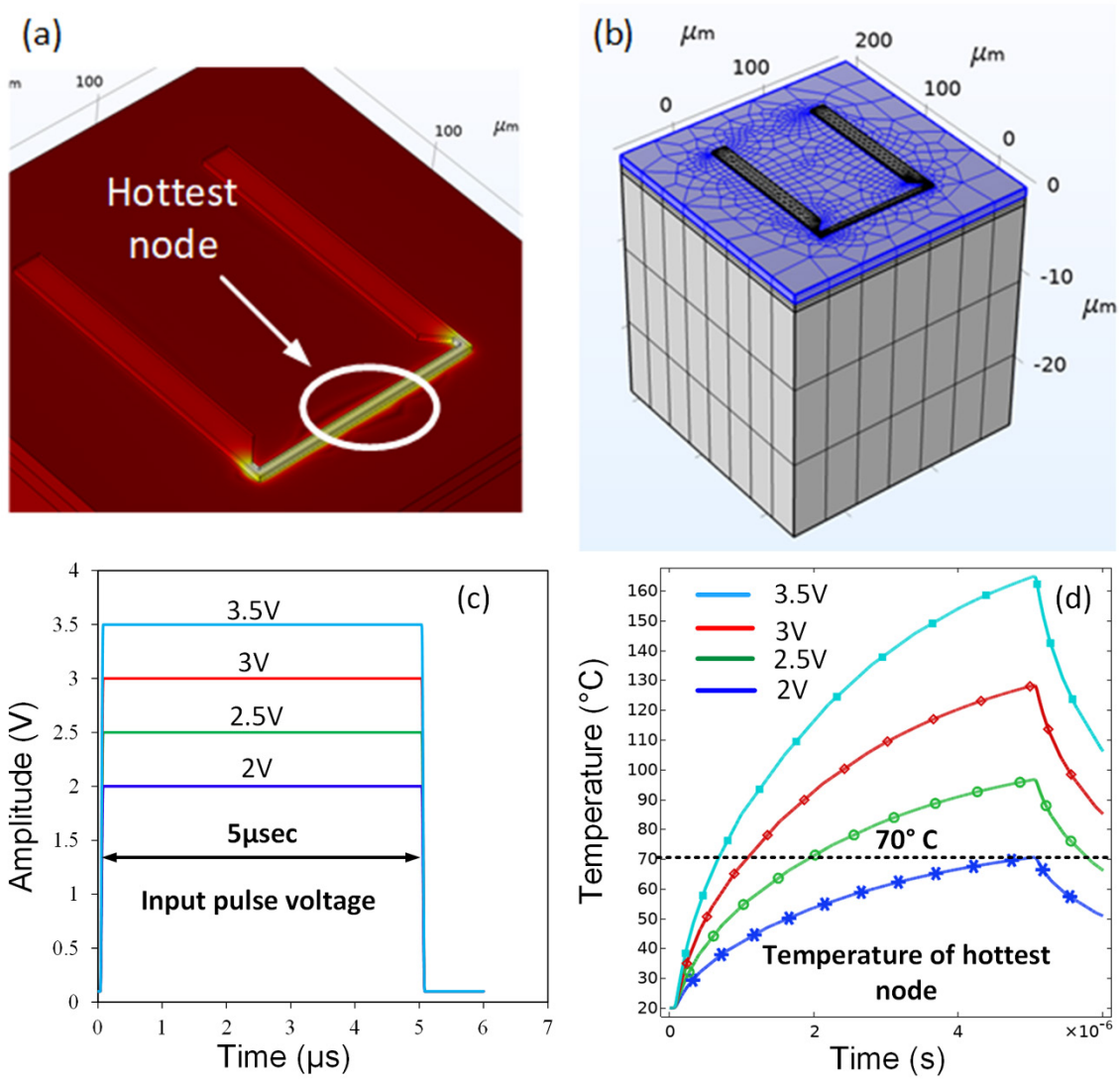

Figure 4-30: (a), (b) FEM model used to simulate transient response and switching time of the VO_2 switch, (c) applied pulse voltage to the heater element and (d) simulated transient temperature of the hottest node.

4.4.3 VO2 Switch Integrated with SAW Resonators

The monolithic integration of VO_2 switches with a SAW resonator is shown in the optical image of Figure 4-31. The fabricated switched resonator consists of a conventional SAW resonator with interdigitated Al electrodes between signal and ground electrodes in a one-port configuration

and two VO_2 switches symmetrically placed on each side of the resonator. These switches short the signal and ground electrodes when they are turned ON effectively detuning the resonator.

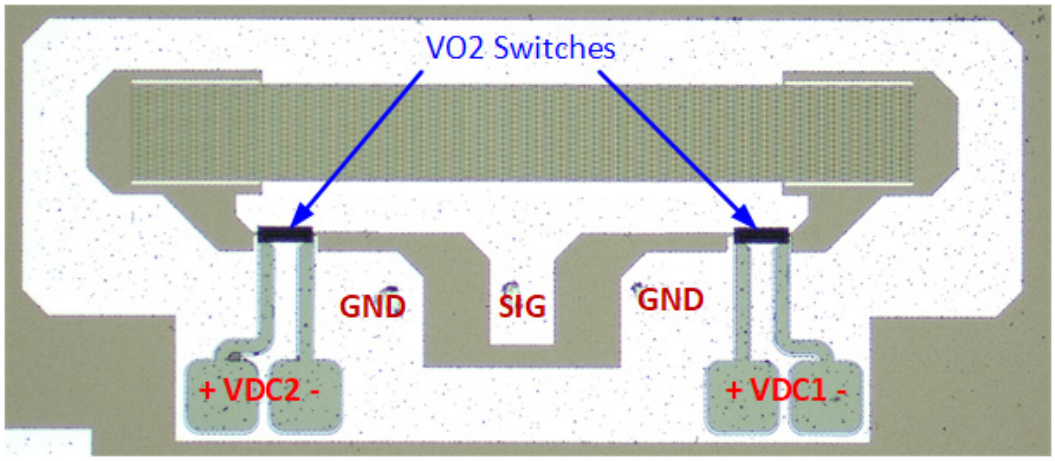

Figure 4-31: Optical image of the fabricated switched SAW resonators with monolithically integrated VO2 switches.

Measured S-parameters and impedance plots for two resonators with and without the VO_2 switches are presented in Figure 4-32. The measured resonance and anti-resonance frequencies are F_S = 742 MHz and F_P = 777 MHz, respectively and there is almost no change in the response of the switched SAW resonator compared to the conventional SAW resonator without VO_2 switches. The extracted quality factor Q for the fabricated switchable resonators are also shown in Figure 4-33. The resonator with VO_2 switches shows slightly lower Q at the anti-resonance frequency (F_p) which is due to the loading effect of the VO_2 switches in their OFF state (R_{OFF} = 1.47 kΩ). The resonator Q can be further improved by improving the quality of the deposited VO_2 layer and by increasing the resistance ratio (R_{OFF}/R_{ON}).

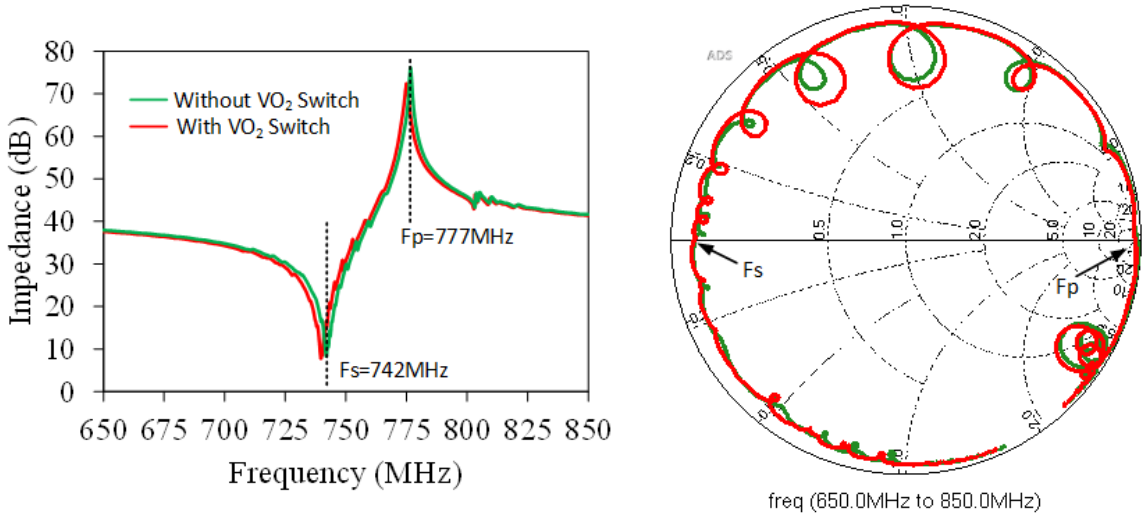

Figure 4-32: Measured impedance and S-parameter responses of SAW resonators with and without VO_2 switches.

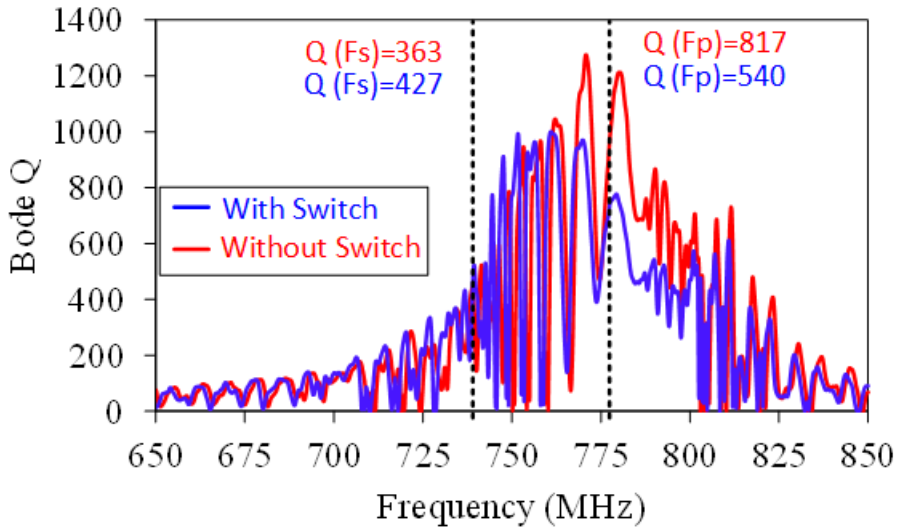

Figure 4-33: Measured Q factor of SAW resonators with and without VO_2 switches.

In order to switch the resonator OFF and characterize the switching performance of the fabricated resonator, a DC bias voltage V_{DC} = 2.5 V is applied on both VO_2 switches and the S-parameters are measured as shown in Figure 4-34. When the DC bias voltage is applied, the VO_2 material is

heated above 70°C and it becomes conductive, effectively shorting the signal and ground electrodes of the SAW resonator and preventing the excitation of the acoustic waves.

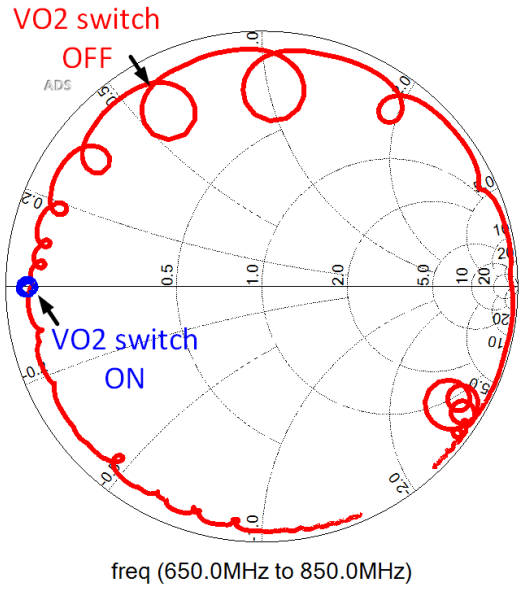

Figure 4-34: Measured S-parameters of the switched SAW resonator when the switch is turned ON and OFF.

In order to investigate the effect of VO_2 switch on the linear performance of the proposed switchable resonator, 2nd harmonic emissions of resonators with and without the VO_2 switches were measured as shown in Figure 4-35. A single-tone 2nd harmonic test setup was used to apply a +15dBm tone at resonator input port and the reflected 2nd harmonic emission was measured from the same port. The frequency of the high power tone (f) was swept from 675 MHz to 765 MHz. As shown in Figure 4-35, there is a very small difference in the measured 2nd harmonic levels for the resonators with and without the VO_2 switch, which indicates there is no impact on the linear performance of the SAW resonator when integrated with the VO_2 switch.

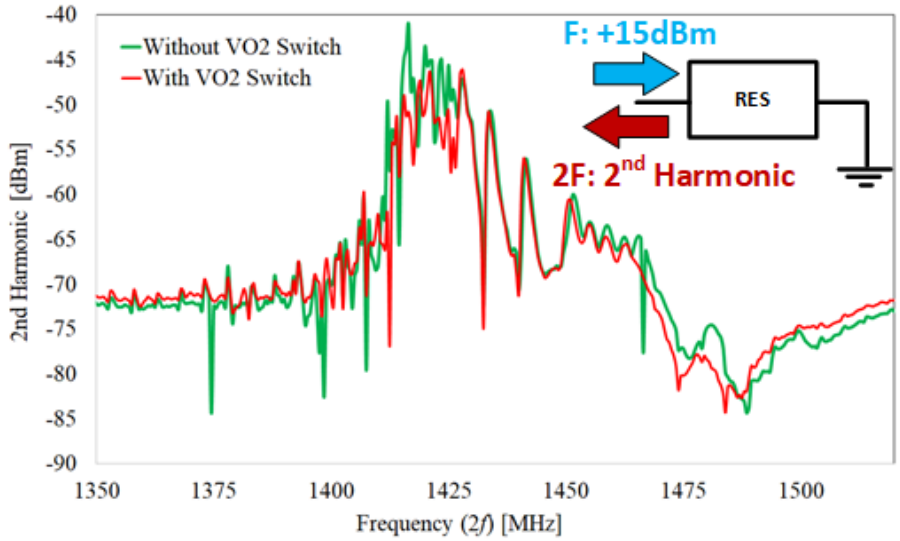

Figure 4-35: Measured 2nd harmonic emissions of SAW resonators with and without VO_2 switches.

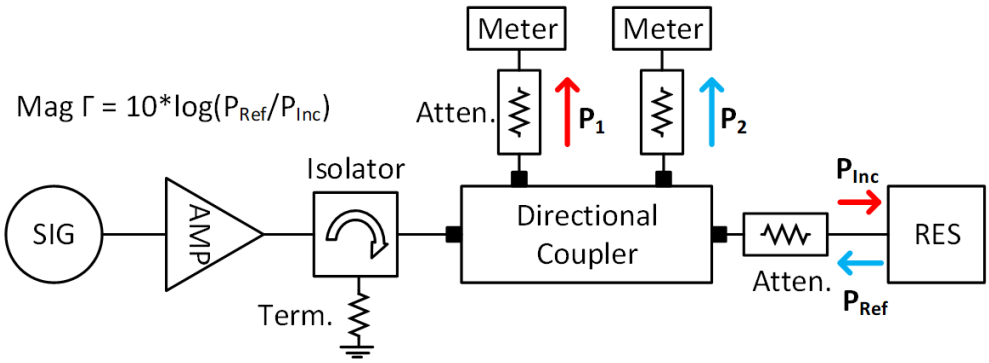

Figure 4-36: Block diagram of the high-power test setup.

High power characterization of the proposed switched resonator is performed to ensure that under high power, RF heating does not lead to self-actuation of the VO_2 switch and hence limited power handling capability. To measure power handling capability of the fabricated resonator, a high-power test setup, as shown in Figure 4-36, was used to measure the resonator response under input power levels from +15 dBm up to +26 dBm. Measured magnitude of S_{11} for different input power levels is presented in Figure 4-37. The resonator can handle RF powers up to +25 dBm without any self-actuation of the VO_2 switch or significant frequency shift or resonator Q

degradation. The irreversible change in S_{11} response and failure that occurs at +26 dBm as shown in Figure 4-37 is attributed to the damage to the aluminum electrodes which is a well-known power handling issue for SAW resonators and can be improved using a better electrode material.

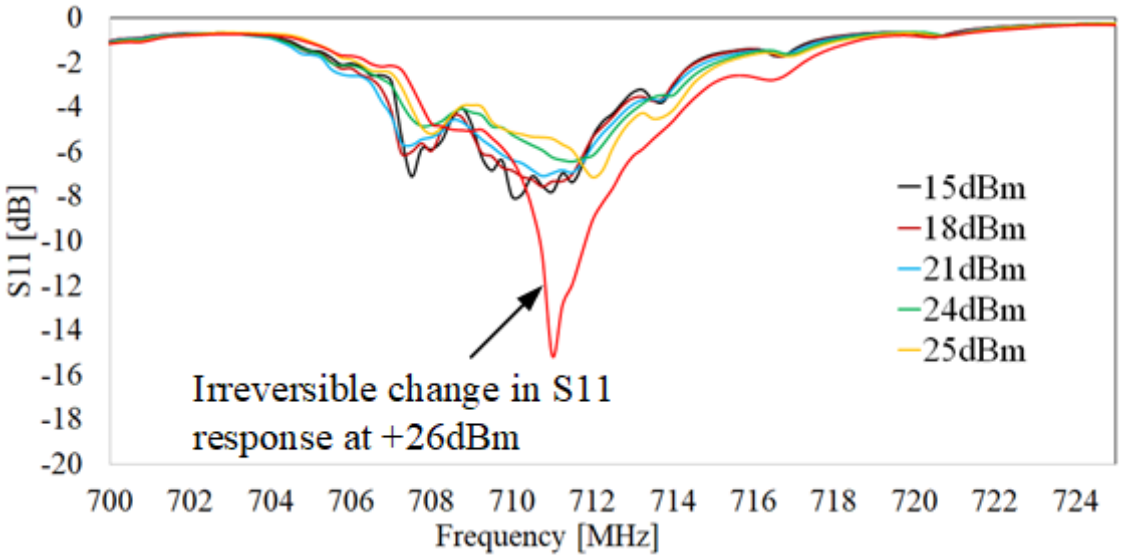

Figure 4-37: S-parameter response of the switched SAW resonator under different power levels.

4.4.4 Switched Dual-Band Filter with VO_2 Switches

The 7-pole switched dual-band filter designed in section 4.2.5 is implemented using monolithically integrated VO_2 switches, as shown in Figure 4-38. The SAW filters and VO_2 switches are all fabricated on the same $LiTaO_3/SiO_2/Si$ substrate using the four-mask fabrication process depicted in Figure 4-26. The SMD matching inductors are also assembled on the SAW chip using soldering. An optical image of the fabricated switched dual-band filter is demonstrated in Figure 4-38 which also shows a close-up view of the integrated VO_2 switches. The total area of the filter including filters for both upper and lower channels, six VO_2 switches, matching inductors,

DC bias pads and RF testing pads is only 2.8 mm × 5.3 mm. Measured S-parameter response of the fabricated switched dual-band filter for four different states is presented in Figure 4-39. When both channels are ON, the dual-band filter has an insertion loss of 3.2 dB for both low and high channels. In order to turn each channel OFF it is possible to detune the middle shunt resonators (SH-H_2) and (SH-L_2), by actuating the VO_2 switches connected to these resonators.

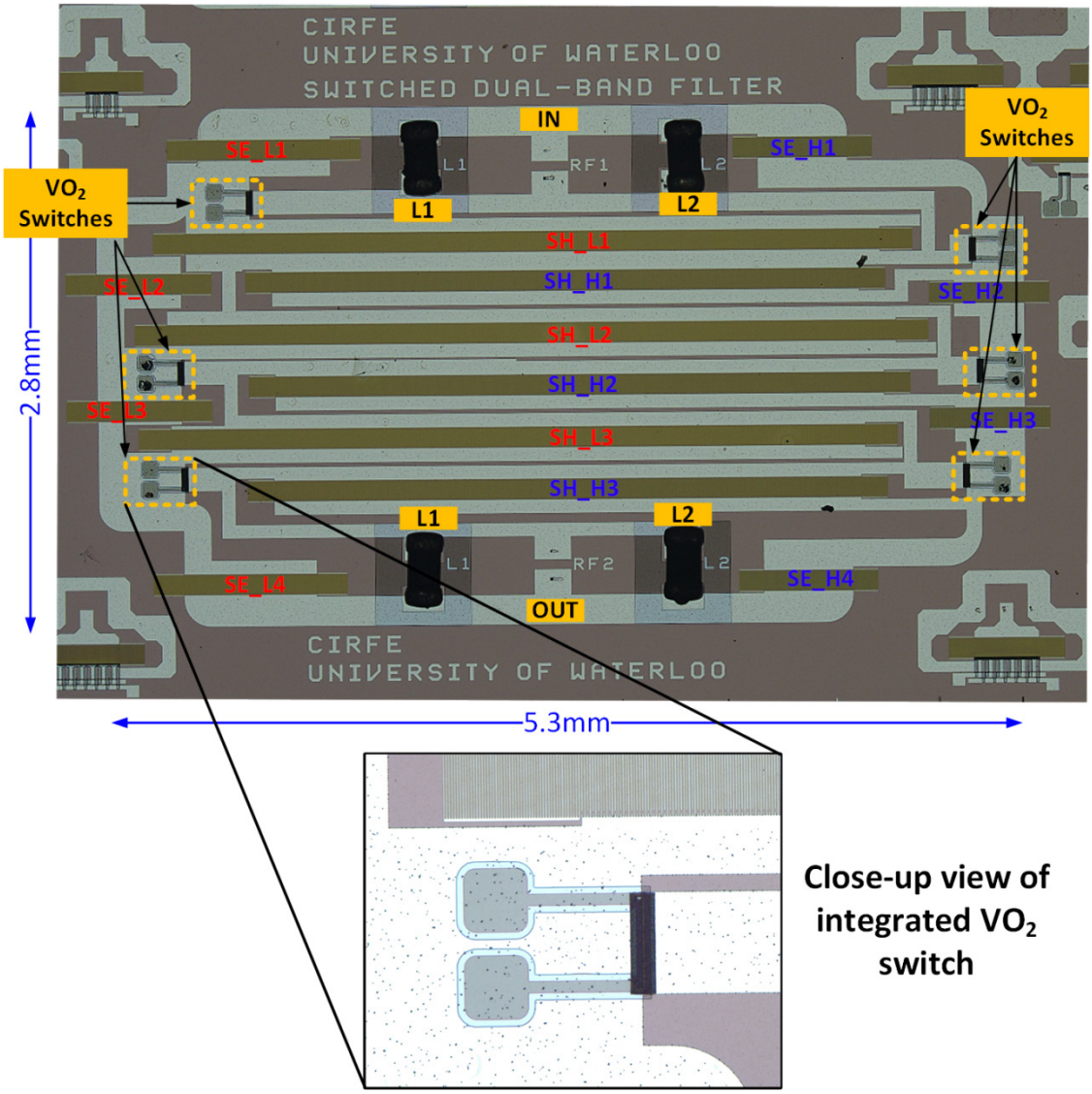

Figure 4-38: Fabricated 7-pole switched dual-band filter using monolithically integrated VO_2 switches.

By detuning only the middle shunt resonator within each filter, a maximum isolation of 20 dB, as presented by black color traces in Figure 4-39, is achieved which is roughly 10 dB better than the isolation achieved for the switched dual-band filter of Figure 4-23 which uses the wire bonds and hybrid integration approach for the VO_2 switches. It is also possible to detune all the shunt resonators by actuating all three VO_2 switches at the same time, as shown in Figure 4-39(b-d), traces in blue color. The isolation for each channel when all three shunt resonators are detuned is better than 40 dB.

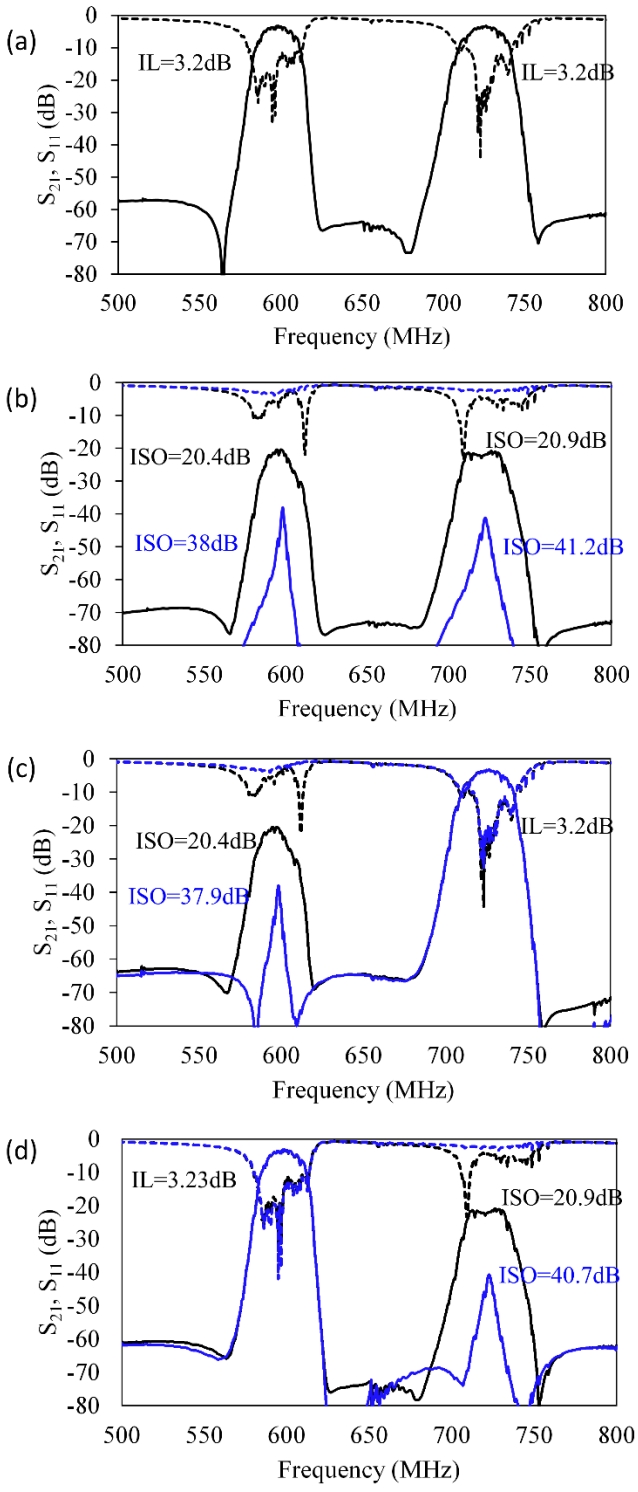

Figure 4-39: Measured S-parameters of the fabricated switched dual-band filter for four different states (a) both channels are ON, (b) both channels are OFF, (c) low channel is OFF, and (d) high channel is OFF. Traces in black color are for detuned middle shunt resonator and in blue color are when all shunt resonators are detuned.

4.5 Summary

Switched SAW dual-band filters with four filtering states have been presented and experimentally demonstrated in this chapter. The proposed switched dual-band filters have been implemented using both hybrid and monolithic integration of VO_2 switches with the SAW resonators and filters. A 5-pole dual-band filter was designed and implemented utilizing two discrete VO_2 switches that are connected to the SAW resonators using wire bonds. By detuning the middle shunt resonators of the 5-pole filters an isolation of ~10 dB was achieved in the filter's OFF state. The degraded isolation performance is due to the parasitic effects of the wire bonds using hybrid integration approach. Monolithic integration of VO_2 switches with SAW filters on a single chip was demonstrated. Linear and high-power performance characteristics of the proposed switched SAW resonators have been studied. A 7-pole switched dual-band filter utilizing integrated VO_2 switches was designed and implemented. The monolithic integration approach resulted in significant improvement in the isolation performance while allowing a compact implementation of the proposed filters. To our knowledge, this is the first time a monolithically integrated VO_2 switched SAW filter is ever presented.

Chapter 5

Reconfigurable SAW Resonators and Tunable Filters Using Monolithically Integrated VO_2 Switches

5.1 Introduction

The conventional RF frontend modules consist of many filters each allocated for a specific frequency band. The deployment of new standards will require addition of more filters and multiplexing circuits, resulting in a more complex and expensive RF frontend module. Miniaturization will be essential in order to fit a large number of filters into the limited space that is allocated for the RF frontend module. A tunable filter solution can address this issue by enabling the use of a single filter that can cover multiple frequency bands. However, this tunable filter is also required to meet the critical performance requirements, such as low insertion loss, sufficient power handling and good linearity, while maintaining a compact size. For implementation of a tunable filter, there is a need for reconfigurable resonators that can be tuned and operate at different frequency bands. In this chapter we will present reconfigurable SAW resonators using monolithically integrated VO_2 switches with a tunable resonance frequency. The use of VO_2 switches which are only a few tens of micrometers in size, allows the manufacturing of reconfigurable SAW resonators that can be used in the design and practical implementation of tunable filters. We also demonstrate a modified structure of the proposed reconfigurable SAW

resonator with only one VO_2 switching element manufactured using a five-mask in-house fabrication process. For the first time, we also present design, implementation and measurement results for a tunable SAW filter using the newly developed reconfigurable SAW resonators.

5.2 Reconfigurable Resonator Design

5.2.1 Proposed Frequency Tuning Concept

The resonance frequency of a SAW resonator depends on the geometric dimensions, such as the spacing between interdigitated metal electrodes. To adjust the resonance frequency, a mechanism is required to vary the electrode spacing. In a conventional SAW resonator since the metal electrodes are fixed on a piezoelectric substrate after electrode deposition and patterning, it is not possible to adjust the resonance frequency. The schematic diagram of an IHP-SAW resonator using a multi-layered stack of $LiTaO_3/SiO_2/Si$ is shown in Figure 5-1. The use of a 900 nm thin $LiTaO_3$ piezoelectric layer with Y-42° crystal orientation over a thin layer of SiO_2 and the Si substrate results in a more efficient confinement of acoustic energy within the top piezoelectric layer and improved resonator performance [50].

The unit cell for the proposed reconfigurable SAW resonator, as shown in Figure 5-2(a), consists of m reflective fingers and n active fingers. The tuning mechanism is based on using tuning electrodes that are connected to the ground busbar through monolithically integrated VO_2 switches. In a conventional SAW resonator, reflective fingers can be used to tune the coupling coefficient (K_t^2) of the resonator.

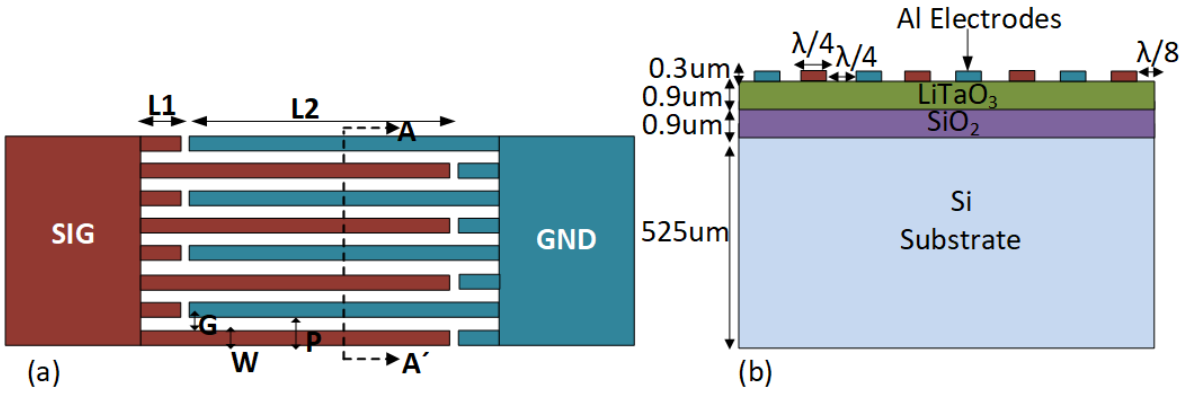

Figure 5-1: (a) Top view of the conventional SAW resonator and (b) cross-section view of the multi-layered substrate stack used in IHP-SAW.

The tuning concept is based on the fact that the mechanical compliance of the piezoelectric transducer is a function of geometry and material properties as well as the electrical boundary condition that is imposed by the interdigitated electrodes on top of the piezoelectric layer [50], [60], [61]. The proposed resonator operates at two different states based on the configuration of the reflective fingers. When the VO_2 switches are turned OFF the tuning electrodes are disconnected from the ground busbar and remain floating, as depicted in Figure 5-2(a). In this case, the static capacitance between the tuning and ground electrodes increases the effective modulus of the stack and the resonator operates at a higher resonance frequency (F_s) [62]. When the VO_2 switches are turned ON and the tuning electrodes are connected to the ground busbar, as shown in Figure 5-2(b), the imposed electric boundary condition results in lowering the anti-resonance frequency (F_p) of the resonator.

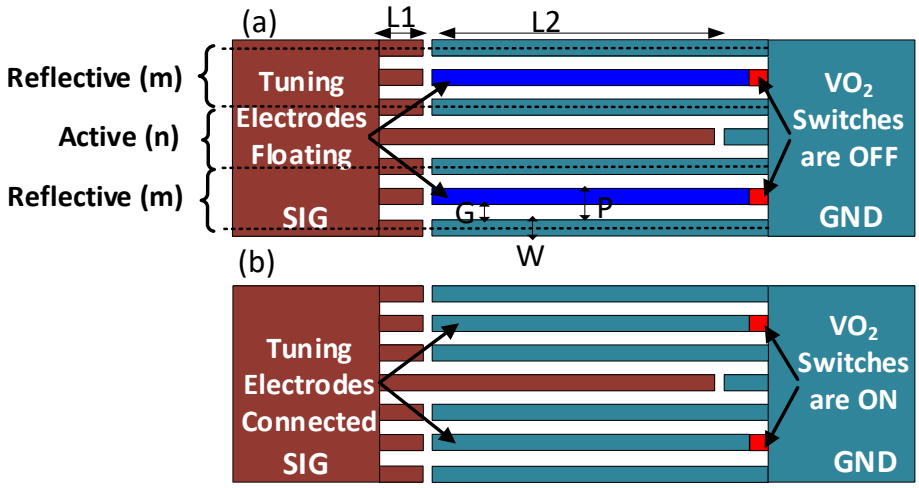

Figure 5-2: (a) Unit cell of the reconfigurable resonator in higher frequency state when the VO_2 switches are turned OFF and (b) lower frequency state when the VO2 switches are turned ON.

5.2.2 FEM Simulation Results

Finite element modeling results in COMOSL for a unit cell consisting of m = n = 2 fingers and dimensions of W = G = λ/4 = 1.375 µm, P = 2.75 µm, L_1 = 5 µm, and L_2 = 100 µm are presented in Figure 5-3. The simulated impedance of a conventional resonator without any tuning electrodes shows resonance and anti-resonance frequencies of F_s = 711 MHz and F_p = 754 MHz, respectively and the simulated effective coupling coefficient is K_t^2 = 13.5%. For an electrode configuration where tuning electrodes are disconnected from the ground busbar and are floating, as shown in Figure 5-2(a), the simulated impedance response shows a higher resonance frequency of F_s = 734 MHz while the anti-resonance frequency F_p = 755 MHz is similar to the conventional resonator. By shorting the tuning fingers to the ground busbar, as shown in Figure 5-2(b), the resonator shows a lower anti-resonance frequency of F_p = 732 MHz and the same resonance frequency of F_s = 711 MHz as the conventional resonator.

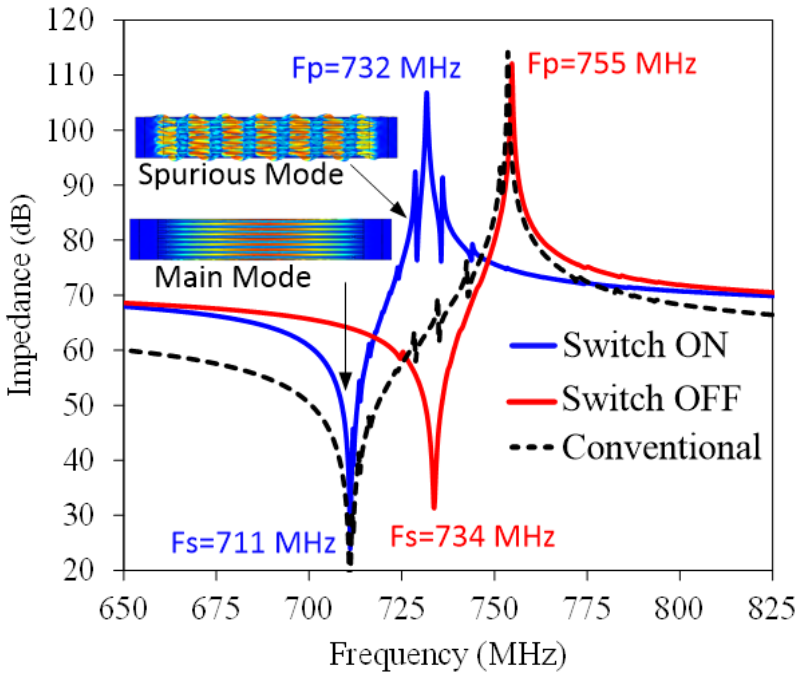

Figure 5-3: FEM simulation results for a unit cell with m=n=2 fingers for the different tuning states and comparison with a conventional SAW resonator.

By employing switching elements that can connect or disconnect the tuning electrodes to the ground busbar, it is possible to construct a reconfigurable resonator with a tuning range of 23 MHz and an effective coupling coefficient of K_t^2 = 6.7%. The reconfigurable resonators presented in this chapter utilize unit cells with m = n = 2 fingers in order to achieve the maximum tuning range however, in other configurations where m ≠ n it is possible to obtain different tuning values. It is also important to note that the maximum achievable tuning range depends on the effective coupling coefficient of the resonator which can be improved by employing a piezoelectric material with a higher piezoelectric constant such as Lithium Niobate. The simulated impedance response of the designed resonators presents spurious modes as shown in the FEM simulation results of Figure 5-3. These spurious modes can be reduced or eliminated using design techniques for the interdigitated metal electrodes as presented in [63].

5.2.3 Reconfigurable Resonator with VO_2 Switches

A schematic diagram of the reconfigurable SAW resonator using monolithically integrated VO_2 switches along with the critical dimensions are shown in Figure 5-4. The switching element consists of a 14 μm × 62 μm VO_2 layer deposited over the 1.25 μm gap between the tuning electrodes and the ground busbar near the contact points, as shown in Figure 5-4 (a). A 3 μm wide Cr layer is used as a heater element. The heater element is deposited over a SiN dielectric which electrically isolates the Cr heater from the metal electrodes and the VO_2 material. The SiN dielectric is also a good thermal conductor and is used to transfer the heat generated in the heater element down to the VO_2 layer. The VO_2 material which is a phase change material changes its state from insulator to conductor when a DC bias current is applied through the Cr heater and when a temperature above a transition temperature of around 70°C is achieved. The performance of the VO_2 switch in terms of resistance ration (R_{OFF}/R_{ON}) depends on the quality of the VO_2 film and its change in resistivity. The measured change in resistivity versus temperature for the deposited VO_2 material using Pulsed Laser Deposition (PLD) technique for both heating and cooling cycles is presented in Figure 5-5. A resistivity variation of four orders of magnitude (1.4 Ω.cm to 5×10^{-4} Ω.cm) is achieved with a transition temperature of around 70°C. An optimized design of the heater element is required in order to reduce the amount of DC power required to operate the switches. Since the SAW resonator consists of hundreds of interdigitated fingers and tuning electrodes, for a reliable operation, it is also required to design the heater elements in a way that a uniform temperature profile is achieved across all the contact points.

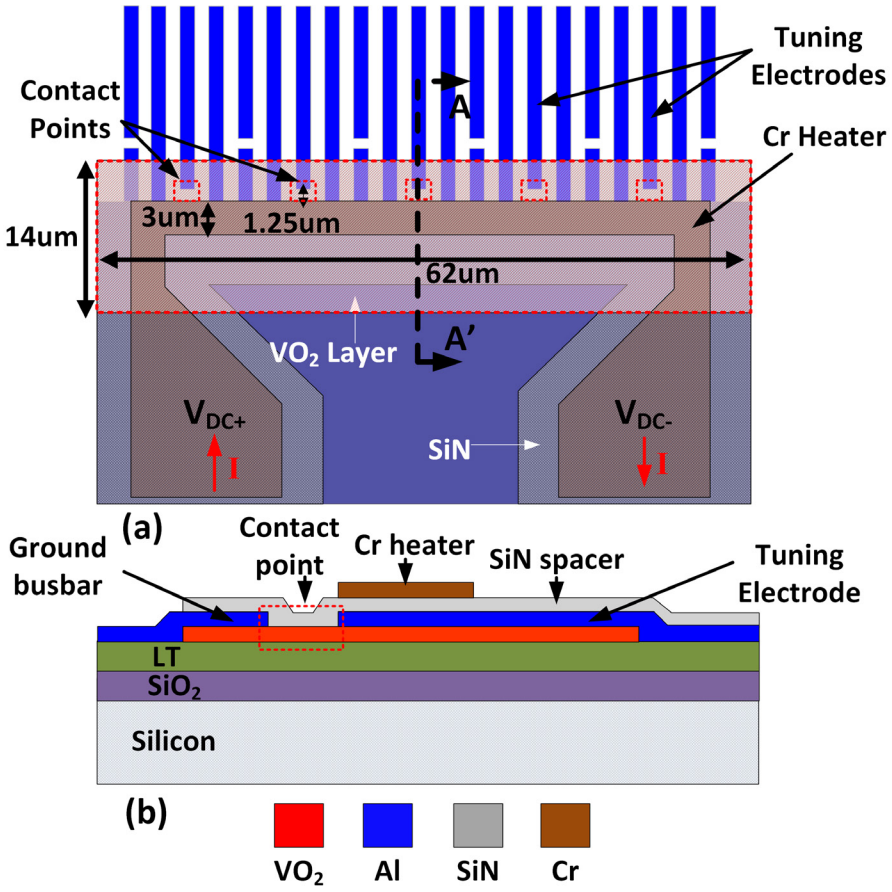

Figure 5-4: Schematic diagram of the reconfigurable SAW resonator with monolithically integrated VO_2 switches (a) and cross-sectional view of the switching element (b).

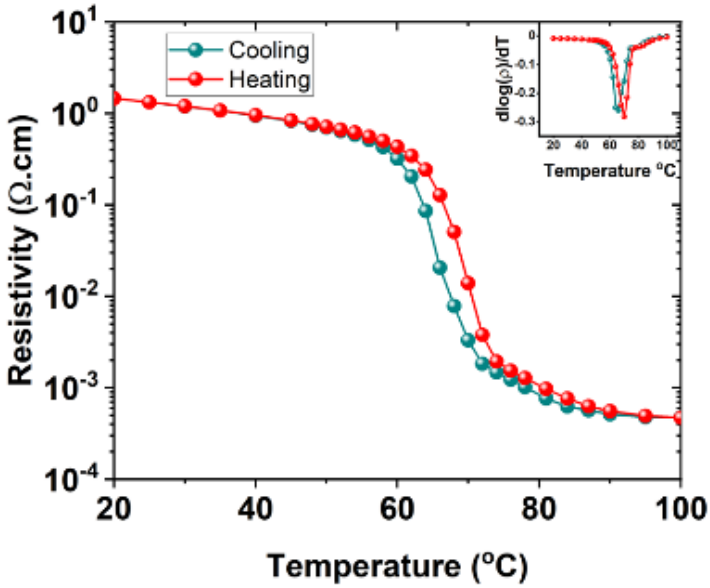

Figure 5-5: Change in resistivity versus temperature for the PLD deposited VO_2 material.

For the designed resonator with a total of 256 metal electrodes we are using six heater elements connected to the same DC bias lines in parallel as shown in the 3D model of Figure 5-6. Finite element simulation in COMSOL is used to find the temperature profile within the VO_2 material and at the location of the contact points between the tuning electrodes and the ground busbar as shown in Figure 5-6(b). A uniform temperature profile is achieved using six heater elements which guarantee a reliable operation of all switching elements and connection between the tuning electrodes and the ground busbar for the ON state of the VO_2 switches. To predict the transient response and switching time, a pulse DC bias voltage with duration of 1.5 μs is applied to the heater element and the peak temperature is plotted as shown in Figure 5-7. The amplitude of the DC bias voltage is swept from 2 V to 3.5 V. A switching time of 1.2 μs is achieved for a DC bias voltage of 2 V while the required DC current is 740 mA. A faster switching can be achieved by increasing the amplitude of the bias voltage.

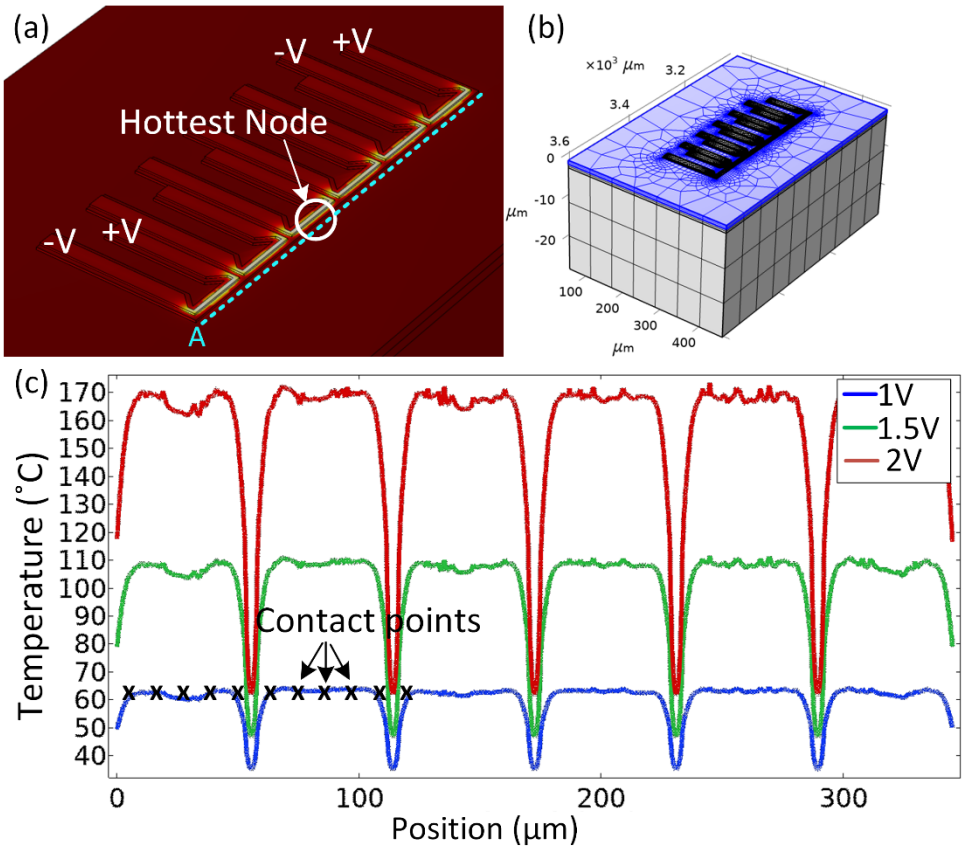

Figure 5-6: 3D FEM model (a, b) and simulated temperature profile along the VO_2 layer and at the location of contact points for the designed resonator with 256 fingers and 6 heater elements (c).

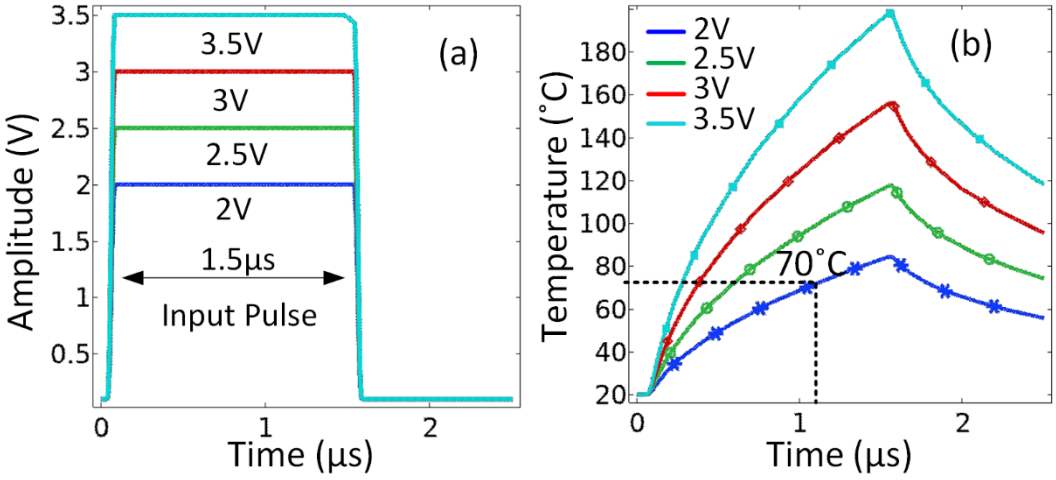

Figure 5-7: Simulated transient response and switching time of the VO_2 switches.

Figure 5-8 shows the processing steps of the reconfigurable SAW resonator with monolithically integrated VO_2 switches. A 300 nm VO_2 layer was deposited using PLD system and then patterned followed by the deposition and patterning of a 300 nm thick aluminum layer used for the interdigitated electrodes. A 200 nm thick SiN layer is then deposited using low temperature PECVD followed by the deposition and patterning of the final 150 nm Cr layer used as the heater element.

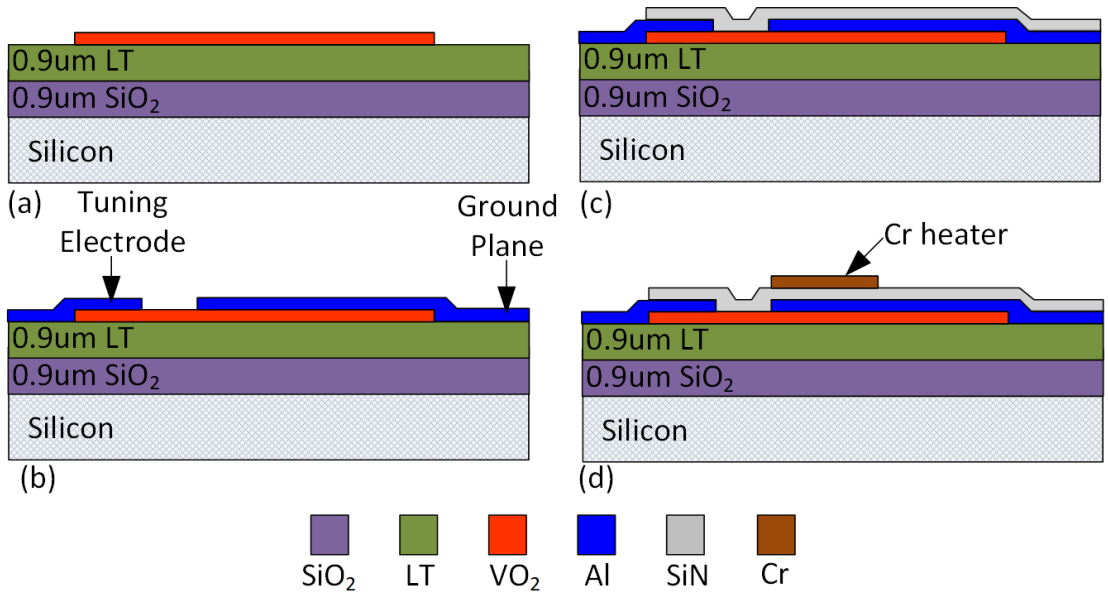

Figure 5-8: Fabrication processing steps for the reconfigurable SAW resonator with monolithically integrated VO_2 switches.

An optical image of the fabricated resonator is shown in Figure 5-9. The reconfigurable SAW resonator consists of interdigitated metal electrodes between the signal and ground busbars in a one-port configuration, tuning electrodes that are connected to the ground busbar through VO_2 switches, and six heater elements connected in parallel to the DC bias pads in order to create a uniform temperature distribution across the VO_2 switching elements.

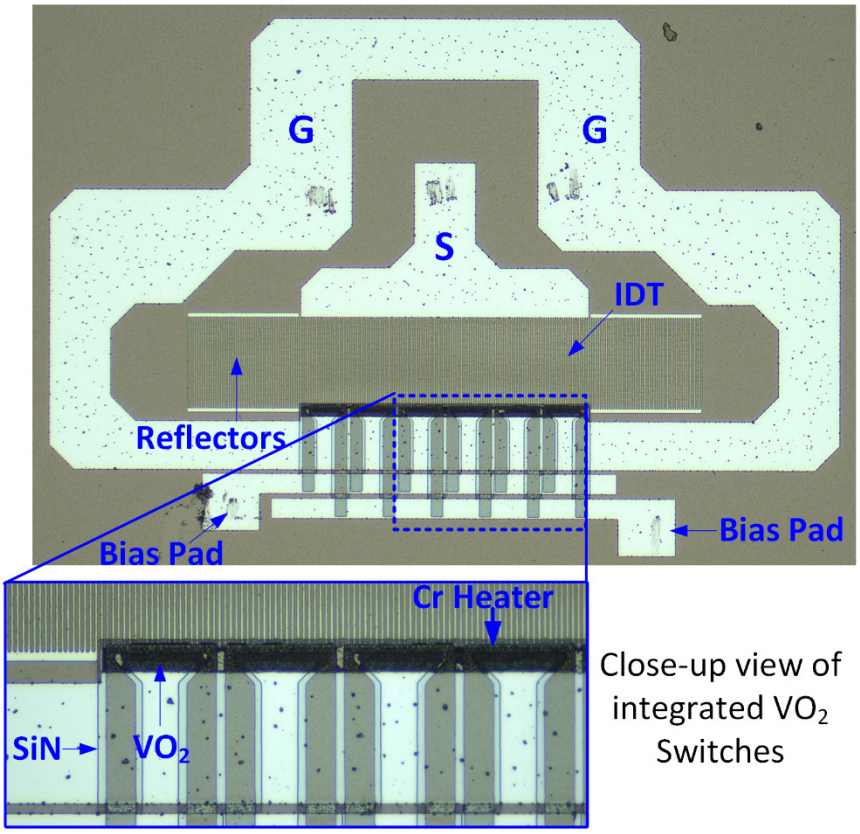

Figure 5-9: Optical image of the fabricated reconfigurable SAW resonator with monolithically integrated VO_2 switches.

Measurement results for the fabricated resonator are presented in Figure 5-10. As shown in the impedance response, the resonance and anti-resonance frequencies are F_s = 720 MHz and F_p = 737 MHz, respectively in the high frequency operation state, when the VO_2 switches are OFF. By applying a DC bias voltage of 2 V and turning ON the VO_2 switches the frequency of the resonator is shifted by 20 MHz. As shown in Figure 5-11, the measured quality factor (Q) of the fabricated reconfigurable resonator varies from 346 to 672 over the tuning range.

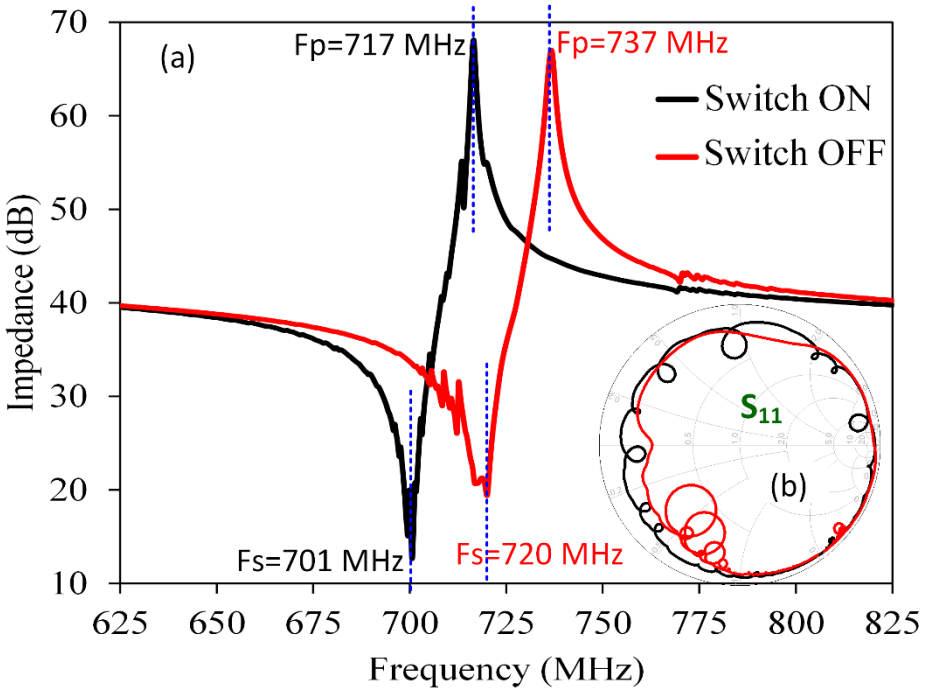

Figure 5-10: Measured impedance response (a) and reflection coefficient S_{11} (b) of the fabricated reconfigurable SAW resonator for two tuning states.

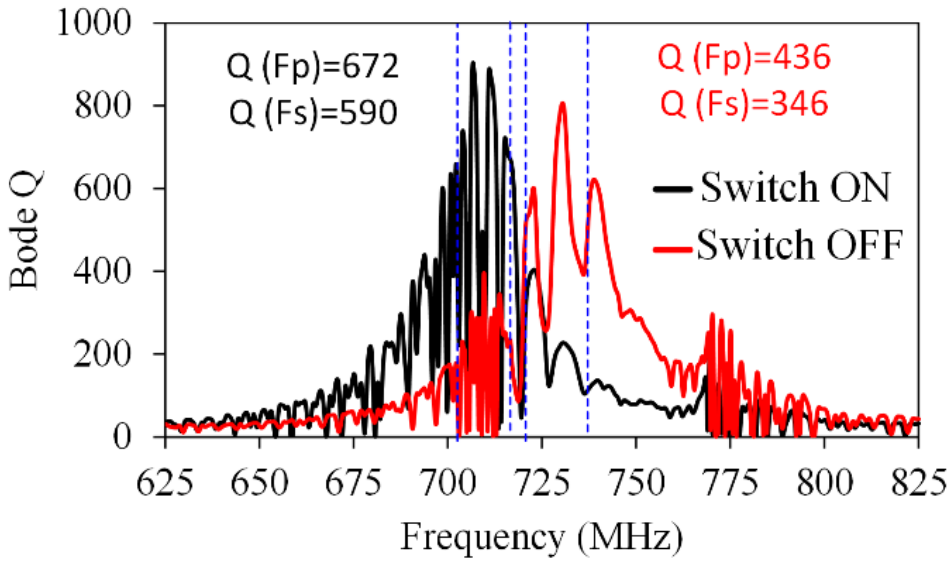

Figure 5-11: Measured resonator quality factor (Q) for different tuning states.

The monolithic integration of the VO_2 switches results in a compact implementation of the proposed reconfigurable SAW resonator. However, for a reliable operation of all the switching elements, a uniform temperature above the transition temperature of 70ºC is required which is only possible by utilizing a number of heater elements distributed uniformly along the tuning electrodes of the resonator. The use of too many heater elements results in increased DC power consumption for the reconfigurable resonators and filters constructed based on these resonators. Another drawback of the proposed structure is the proximity of the heater elements to the interdigitated electrodes within the active region of the SAW resonator. This proximity can cause frequency shift of the resonator due to the increased temperature during the operation of the VO_2 switching elements in the ON state. To address these issues, we are proposing a modified reconfigurable SAW resonator which utilizes only a single VO_2 switching element located outside the active area of the resonator as explained in the next section.

5.3 Modified Reconfigurable SAW Resonator

Schematic diagram of the reconfigurable SAW resonator with modified structure consisting of a single VO_2 switching element located outside the resonator's active area and away from the interdigitated electrodes is presented in Figure 5-12. The resonator consists of interdigitated and tuning electrodes constructed using the 1st aluminum metal layer M1 deposited and patterned on a multi-layered piezoelectric substrate stack of $LiTaO_3/SiO_2/Si$. Each tuning electrode is connected to a 2nd metal electrode M2 using M1-to-M2 via holes. A single VO_2 switching element is used to electrically connect or disconnect the top M2 electrode from the ground busbar. The VO_2 switch is placed away from the interdigitated electrodes and consists of a 34 μm × 80 μm VO_2 layer deposited over the 3 μm gap between the M1 electrodes within the contact point, as shown in

Figure 5-12 (a). A 4 µm wide Cr layer is used as the heater element which is electrically separated from the underlying M1 electrodes using a SiN dielectric layer.

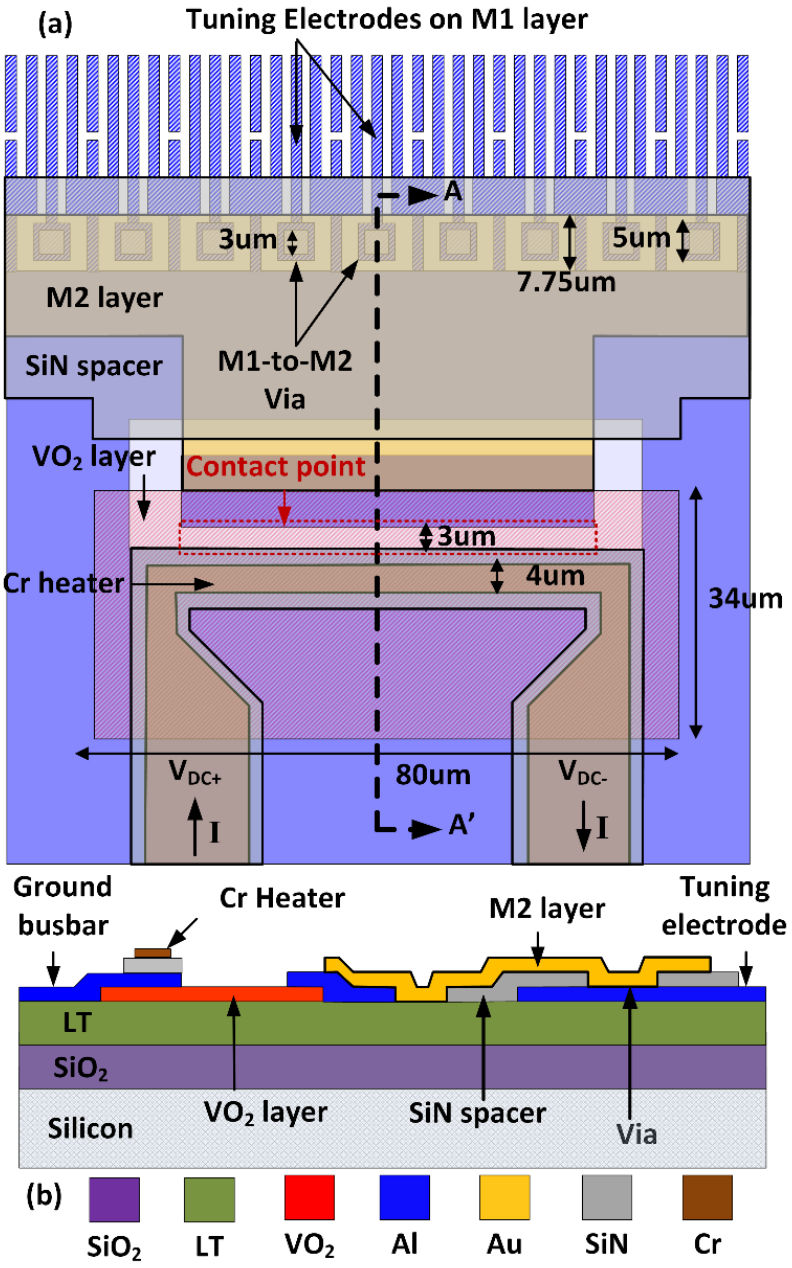

Figure 5-12: Schematic diagram of the modified reconfigurable SAW resonator with a single VO_2 switching element (a) and the cross-sectional view (b).

Figure 5-13 shows the processing steps for the fabrication of the modified reconfigurable SAW resonator using a 5-mask fabrication process carried out at the CIRFE lab clean room at the University of Waterloo. A 300 nm VO_2 layer was first deposited using a PLD system over the multi-layered $LiTaO_3/SiO_2/Si$ substrate. The deposited VO_2 layer is patterned using RIE etching followed by 300 nm deposition of M1 aluminum electrode layer using e-beam evaporation. The aluminum electrodes are patterned using metal RIE. During the next step a 200 nm SiN dielectric layer is deposited using low temperature PECVD at 150ºC. The SiN layer is then patterned using RIE etching to create the M1-to-M2 via holes and also contact pads to the M1 layer. During the next processing step a 100 nm Cr layer is deposited and patterned using lift-off to create the heater elements and also DC connections to the bias pads. The final processing step is the e-beam deposition of a 500 nm gold layer and patterning using lift-off to create the M2 top electrode. The gold layer is also used on the Cr connections used to carry the DC current from the bias pads to the heater elements and also over the RF signal connections between the resonators in a filter to reduce the ohmic losses. In order to create a good M1 to M2 metal contact it is required to remove the native oxide on the M1 aluminum electrodes before the deposition of the M2 gold layer.

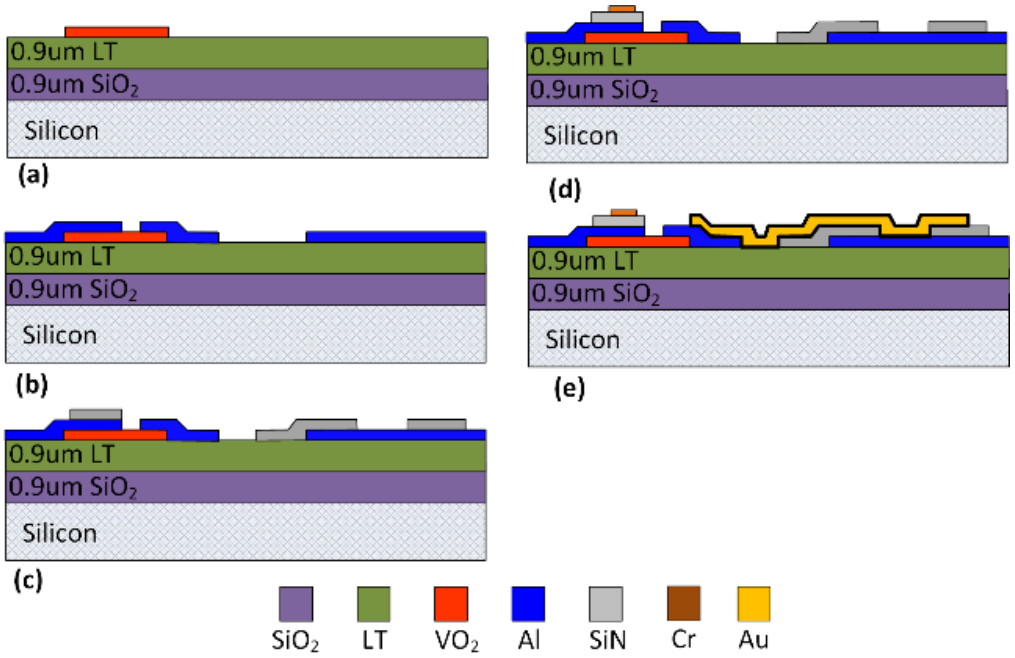

Figure 5-13: Fabrication processing steps for the modified reconfigurable SAW resonator.

An image of the fabricated reconfigurable SAW resonator is shown in Figure 5-14. The resonator consists of 1240 interdigitated fingers and 310 tuning electrodes. The tuning electrodes are connected to the 2nd electrode using vias through the SiN dielectric layer and a single VO_2 switching element is utilized between the top gold electrode and the ground busbar to achieve tuning. The resonator's dimensions are W = G = $\lambda/4$ = 1.43 µm and P = 2.85 µm. Measured small signal S-parameter and impedance response for the fabricated resonator are shown in Figure 5-15. The resonance and anti-resonance frequencies are F_s = 713 MHz and F_p = 730 MHz, respectively in the high frequency operation state, when the VO_2 switch is OFF. A frequency shift of 18 MHz is achieved by turning the VO_2 switch ON and connecting the tuning electrodes to the ground busbar through the top metal electrode and via connections. For the high frequency state, the resonator shows a strong spurious mode below F_s as shown in the S_{11} plot in Figure 5-15 (b). This

spurious mode can be reduced by optimizing the shape of the interdigitated electrodes near the M1-to-M2 via connections.

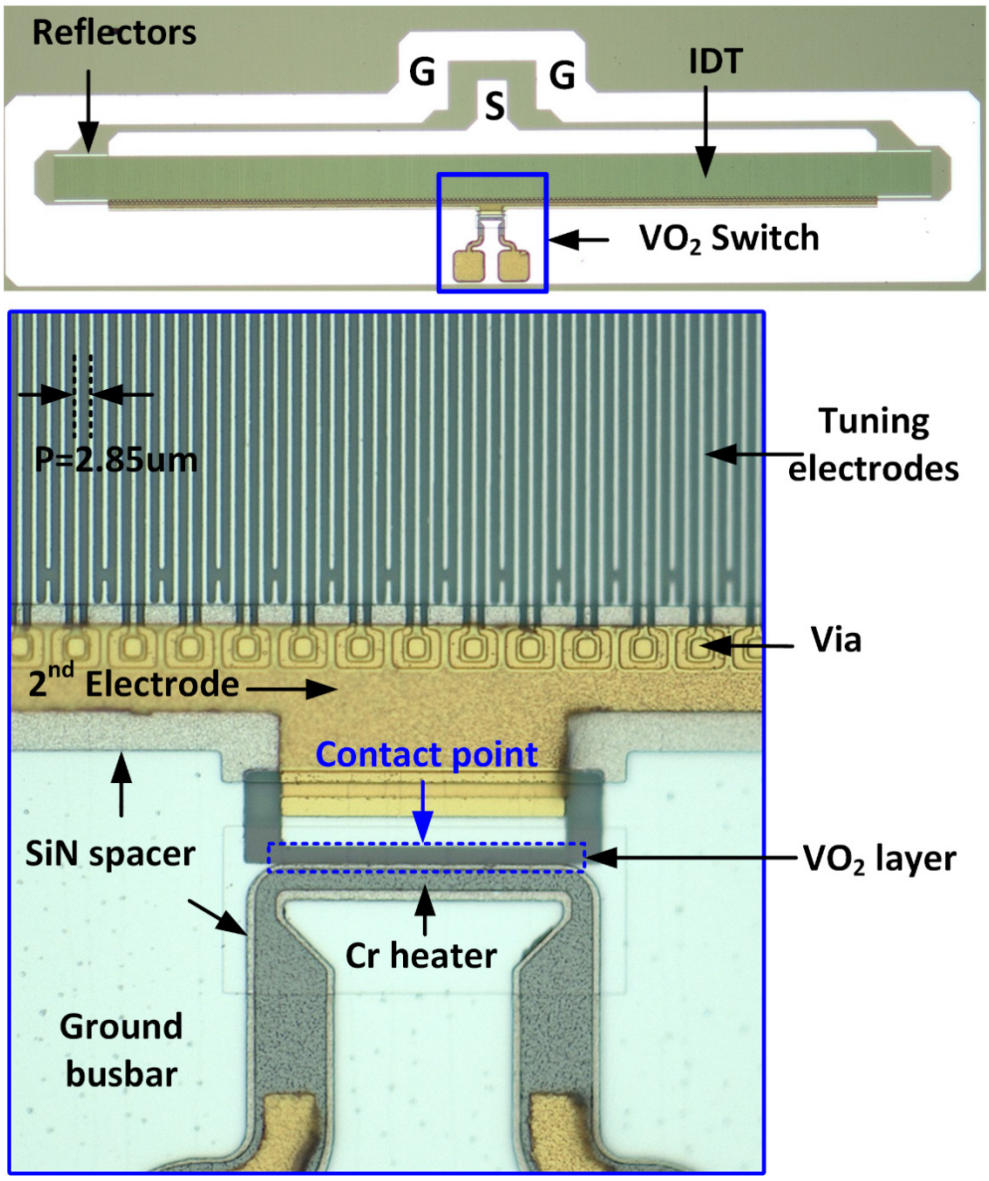

Figure 5-14: Optical image of the fabricated reconfigurable SAW resonator with only one VO_2 switching element.

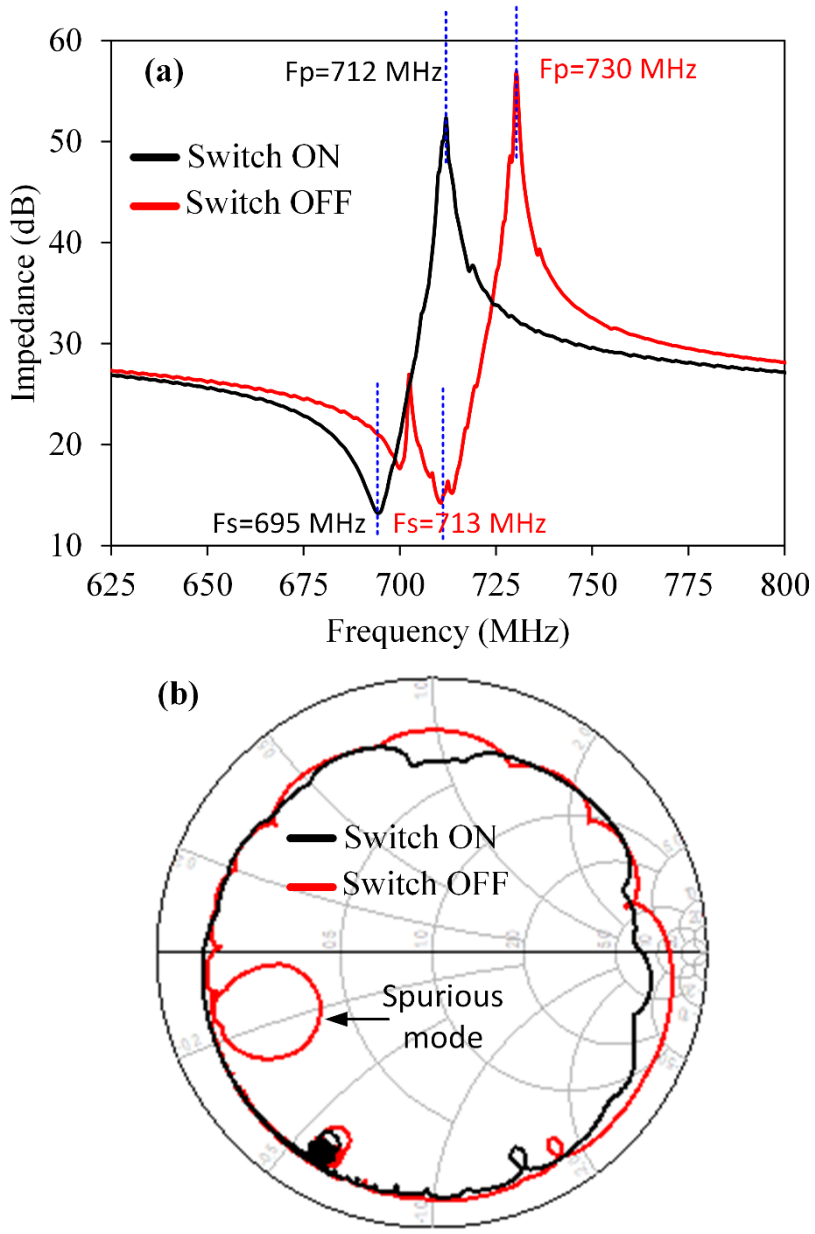

Figure 5-15: Measured impedance (a) and reflection coefficient S_{11} (b) of the fabricated reconfigurable SAW resonator with single VO_2 switch.

As shown in Figure 5-16 the measured resonator quality factor Q (F_p) is better than 514 and Q (F_s) remains above 121 for both tuning states. The resonator Q can be further improved by improving the conductivity of the aluminum electrodes and reducing the ohmic losses in the resonator and

also by optimizing the thickness of the $LiTaO_3$ and SiO_2 layers in the multi-layered piezoelectric substrate stack.

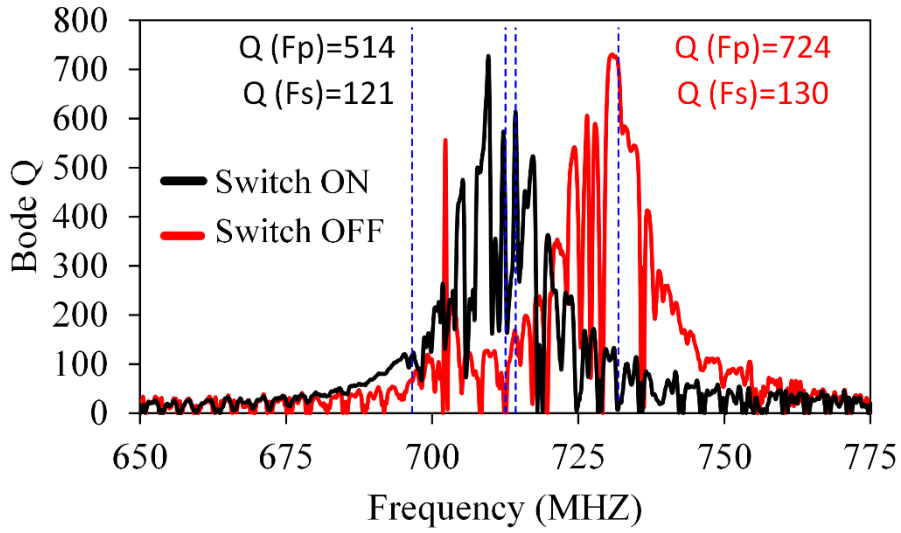

Figure 5-16: Measured quality factor of the resonator for different tuning states.

Thermal imaging of the VO_2 switch using an IR microscope is presented in Figure 5-17. A DC bias voltage of 6 V with a DC bias current of 21 mA is applied to the heater element. The required DC power to turn the VO_2 switch ON is ten times smaller than the DC power required for the reconfigurable SAW resonator with six switching elements presented in section 5.2. The temperature profile along the cross-section of the heater element (AA'), as presented in Figure 5-17 (b), shows a uniform temperature above the 70ºC transition temperature which is required for the operation of the VO_2 switch. The temperature profile along the cross-section of the IDT electrodes of the SAW resonator is also measured as shown in Figure 5-17(c). In the modified structure of the resonator by placing the heater element far away from the electrodes, the maximum temperature in the IDT electrode region is maintained at room temperature and the rise in

temperature by the heater element does not result in frequency shift of the resonator while the switch is turned ON.

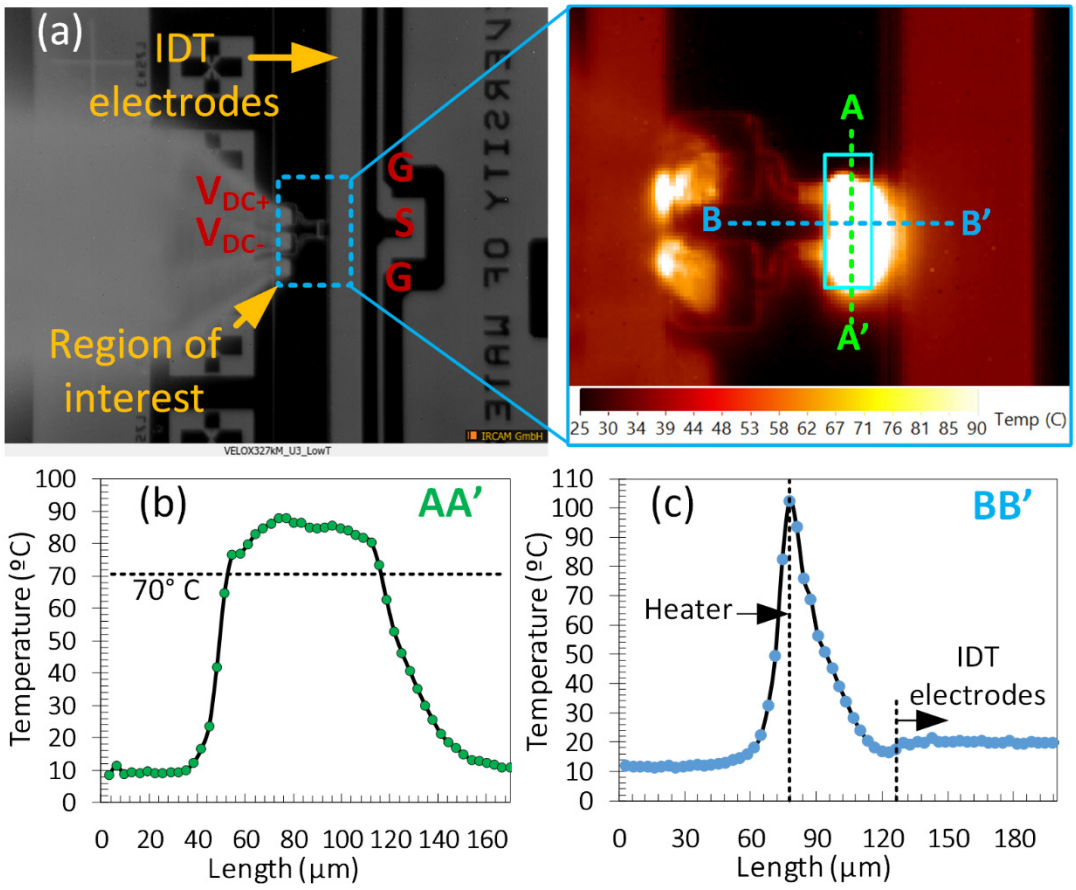

Figure 5-17: Thermal imaging of the VO_2 switching element (a) and temperature profiles along the heater and IDT electrodes (b).

To characterize the power handling, reflection coefficient (S_{11}) of the fabricated resonator is measured by varying the input power from 30 dBm up to 38 dBm as presented in Figure 5-18 for both tuning states. The resonator doesn't show any sign of failure due to high power for both high frequency and low frequency states. A small frequency shift of less than 1 MHz is observed under

high power. The resonator also doesn't show any sign of self-actuation of the VO_2 switching element due to self-heating under the applied high power test conditions presented here. However it is important to note that under real-world operating conditions where the resonators or filters constructed using the proposed resonators are placed inside an RF module, the overall temperature of the module can exceed 70ºC resulting in unwanted switching of the resonators or filters using VO_2 switches. This issue can be addressed by using an alternative phase change material, such as Germanium Telluride (GeTe) with higher transition temperature around 220ºC [64]. In addition to a higher transition temperature, GeTe also possess fast and reversible phase transition that does not require continuous application of high temperature. This property can be utilized as a latching mechanism to conserve the amount of DC power consumption.

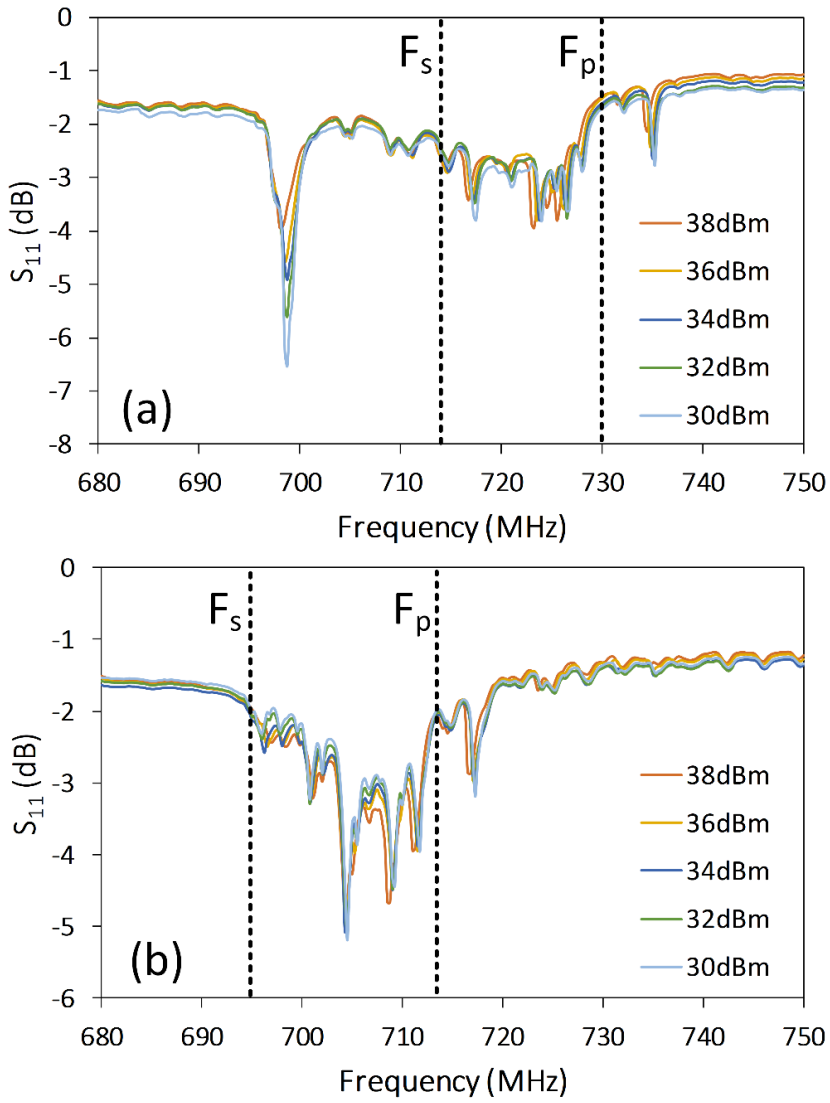

Figure 5-18: Reflection coefficient (S_{11}) of the reconfigurable SAW resonator under high power when the VO_2 switch is OFF (a) and when the switch is turned ON (b).

Nonlinear characterization of the fabricated reconfigurable SAW resonator is illustrates in Figure 5-19. Using a single-tone harmonic measurement test setup, a 23 dBm tone is applied at the fundamental frequency from 680 MHz to 755 MHz and the reflected 2^{nd} harmonic from the resonator is measured at the input port. The resonator shows a higher 2^{nd} harmonic emission for the lower frequency state. This is due to a stronger electric field inside the piezoelectric material

when the VO_2 switch is turned on and the tuning electrodes are connected to the ground busbar.

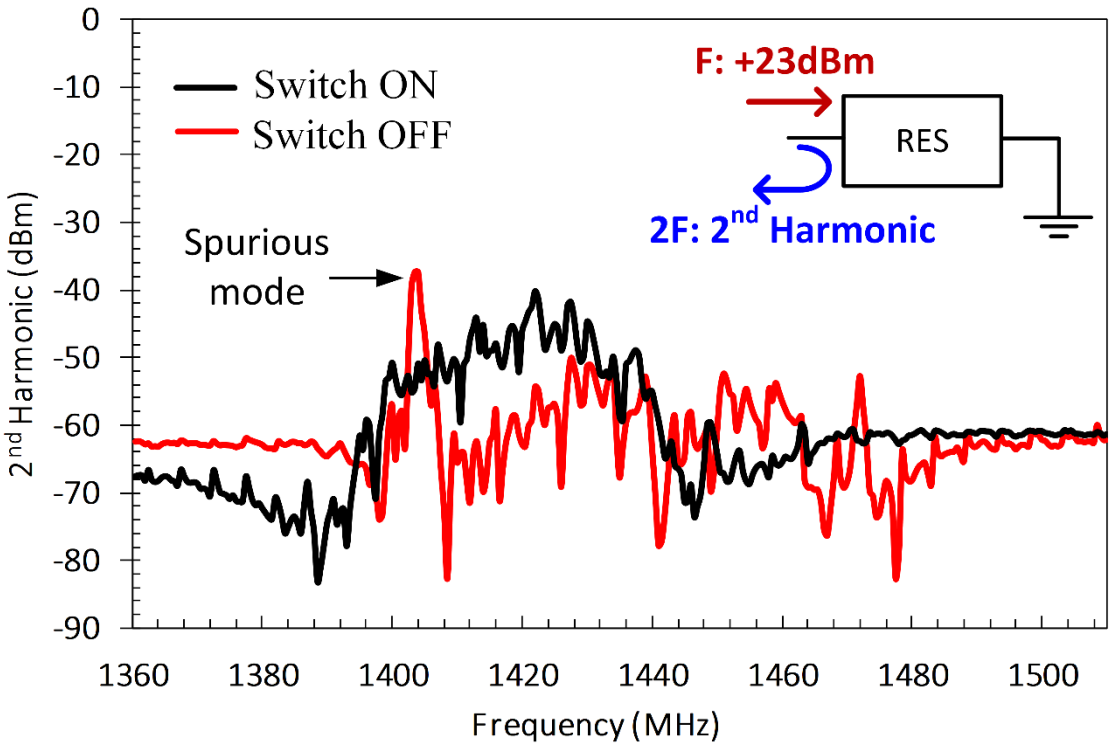

Figure 5-19: Measured 2nd harmonic performance of the reconfigurable SAW resonator for different tuning states.

5.4 Tunable Filter Design

Tunable SAW filters designed based on the proposed frequency tuning method are presented in this section. A proof of concept 6-pole SAW filter comprising of three series and three shunt resonators which has an in-line topology consisting of dangling resonant and non-resonant nodes (NRNs), as shown in Figure 5-20 (a) is designed. Filter synthesis is based on extracted pole technique using the input admittance from each node to find the equivalent parameters of the modified Butterworth Van Dyke (MBVD) circuit model for each series and shunt resonator as

shown in Figure 5-20 (c) [53]. The filter is designed for a center frequency of 970 MHz, bandwidth of 37 MHz and return loss of better than 15 dB within the passband, for the high frequency state, when the tuning electrodes within each resonator are disconnected from the ground busbar. For the low frequency state, when the tuning electrodes are shorted to the ground, the filter has a center frequency of 944 MHz. Filter's bandwidth is determined by the effective coupling coefficient of the reconfigurable SAW resonators which is K_t^2 = 6.7% for the IDT electrode configuration presented here. The parameters of the equivalent MBVD circuit model for each resonator, for the high frequency state, are listed in Table 5.1. The physical dimensions of the resonators such as IDT electrode pitch and number of fingers are then obtained by fitting the measured data from a library of resonators, with different dimensions, to the equivalent MBVD circuit model. The physical parameters of the series and shunt resonators for the designed 6-pole filter are listed in Table 5.2. The resonance frequency F_s and anti-resonance frequency F_p values listed in Table 5.2 are for the high frequency state when the tuning electrodes are disconnected from the ground busbar. The simulated S-parameter response for the designed 6-pole filter and for both tuning states is presented in Figure 5-21. The filter achieves a center frequency tuning from 971 MHz to 944 MHz while the insertion loss is better than 2 dB over the tuning range. The simulation model, in this case, does not include the losses due to the VO_2 switching elements.

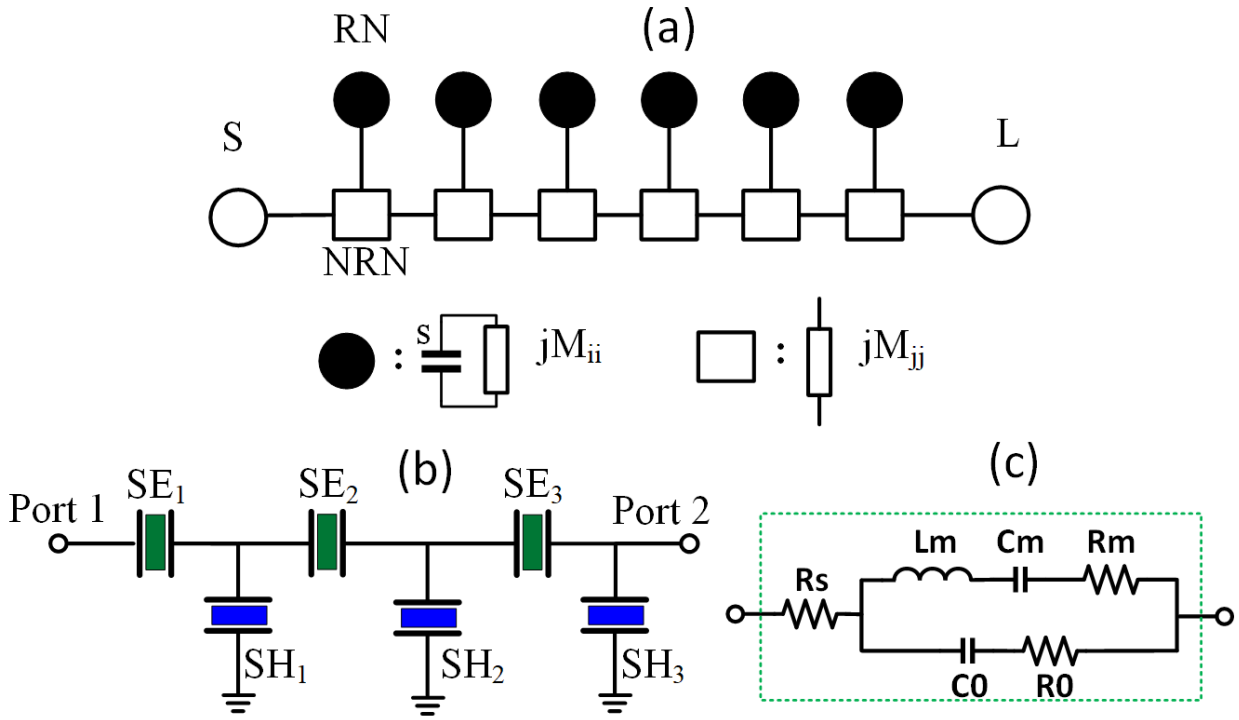

Figure 5-20: Topology (a) and circuit diagram (b) of the 6-pole filter with the equivalent MBVD circuit model for each series and shunt resonators (c).

Table 5.1: MBVD parameters for the 6-pole tunable filter

Parameter	SE_1	SE_2	SE_3	SH_1	SH_2	SH_3
L_m (nH)	108.7	247.08	182	125	107.6	227.7
C_m (pF)	0.249	0.109	0.148	0.23	0.267	0.126
C_0 (pF)	5.081	2.234	3.033	4.417	5.133	2.424
R_m (Ω)	0.9	2.055	1.514	1.039	0.894	1.894
R_0 (Ω)	0.093	0.212	0.156	0.107	0.092	0.195
R_s (Ω)	4.288	1.886	2.56	3.728	4.332	2.046

Table 5.2: Physical design parameters of the 6-Pole tunable filter

Parameter	SE_1	SE_2	SE_3	SH_1	SH_2	SH_3
F_s (MHz)	968	968	968	938	938	938
F_p (MHz)	991	991	991	963	963	963
Pitch (μm)	2	2	2	2.07	2.07	2.07
# of electrodes (n)	360	336	280	472	392	416

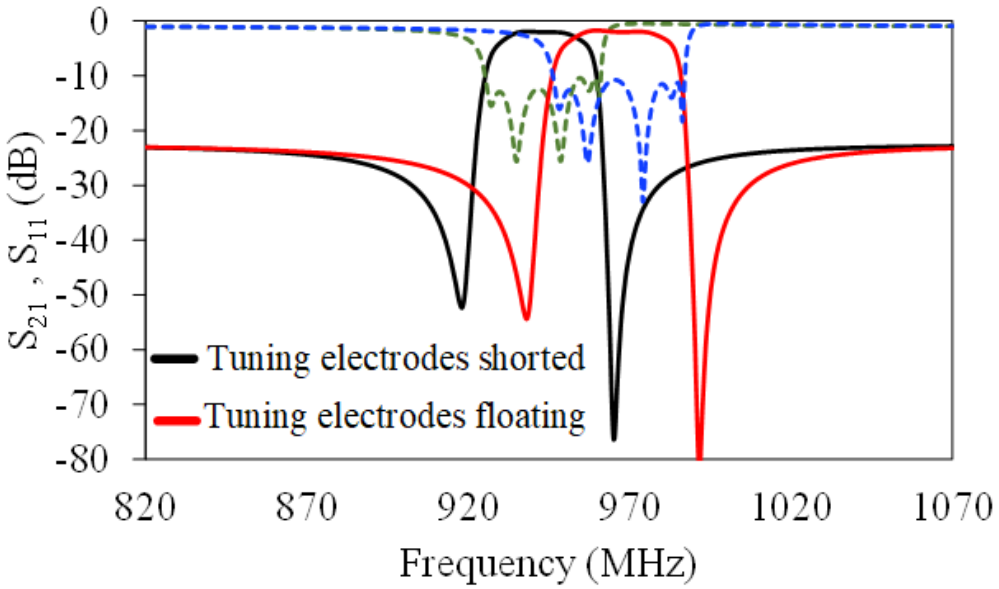

Figure 5-21: Simulated S-parameter response of the 6-pole tunable SAW filter for both tuning states.

Another tunable 3-pole filter is designed using the reconfigurable SAW resonators with monolithically integrated VO_2 switching elements. The filter is comprised of two series and one shunt resonator as shown in Figure 5-22. The filter is designed for a center frequency of 730 MHz and a bandwidth of 16 MHz at the higher frequency state when the VO_2 switches of each resonator are turned OFF. The parameters of the equivalent MBVD circuit model for each resonator and the physical parameters of the series and shunt resonators for the designed filter are listed in Tables Table 5.3 and Table 5.4, respectively.

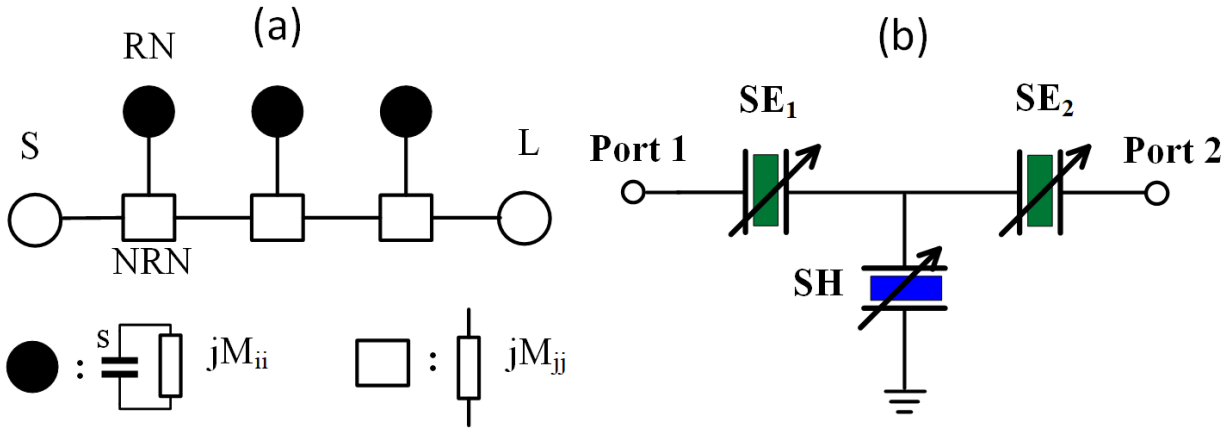

Figure 5-22: Topology and circuit diagram of the tunable 3-pole filter.

Table 5.3: MBVD Parameters for the 3-pole tunable filter

Parameter	SE_1	SE_2	SH_1
L_m (nH)	174	174	97.54
C_m (pF)	0.275	0.275	0.519
C_0 (pF)	5.699	5.699	10.266
R_m (Ω)	1.989	1.989	1.001
R_0 (Ω)	0.242	0.242	0.06
R_s (Ω)	2.372	2.372	3.562

Table 5.4: Physical design parameters of the 3-pole tunable filter

Parameter	SE_1	SE_2	SH_1
Fs (MHz)	726	726	708
Fp (MHz)	744	744	725
Pitch (μm)	2.77	2.77	2.85
# of electrodes (n)	705	705	1241

The simulated S-parameter response for the higher frequency state when the VO_2 switches are turned OFF is presented in Figure 5-23. The simulated filter response for lossless case where both the mechanical loss in resonators and the ohmic loss in the connections are assumed to be zero ($R_s = R_m = R_0 = 0$) is shown in Figure 5-23 (a). The simulated S-parameters by including all the losses

in the SAW resonators, VO_2 switches and the electrical connections between them is presented in Figure 5-23 (b). The simulated insertion loss is better than 2.5 dB with a return loss better than 20 dB within the 16 MHz bandwidth.

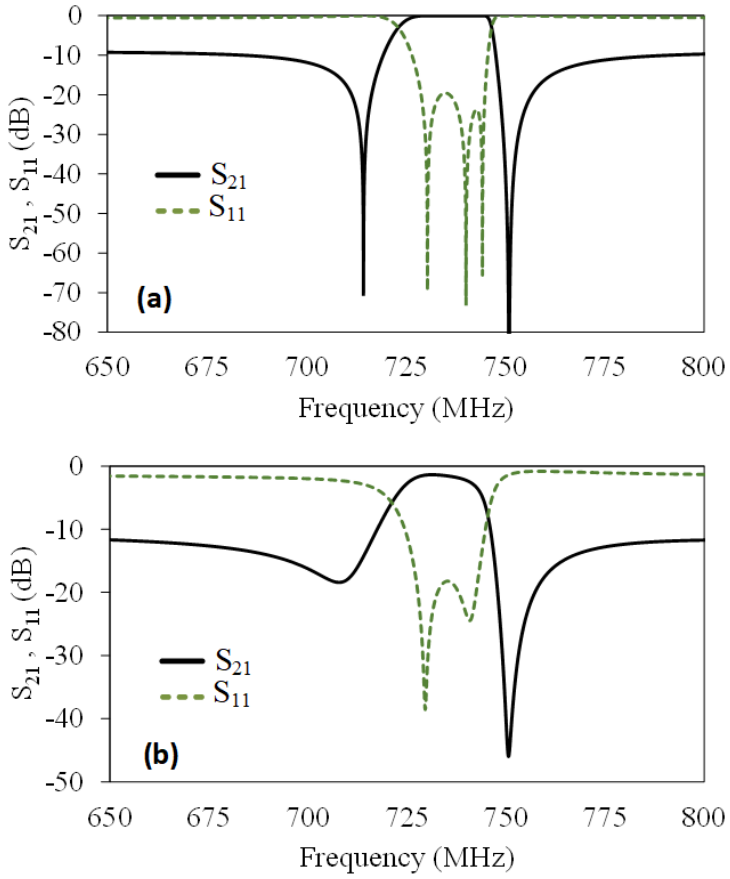

Figure 5-23: Simulated S-parameter response of the 3-pole filter for the loss-less case (a) and when the losses are included (b).

5.5 Measurement Results for Tunable Filter

To demonstrate the application of the proposed frequency tuning concept in a SAW filter, two 6-pole SAW filters are fabricated on the same chip using the design parameters listed in Table 5.2. In the first filter layout, the tuning electrodes within each series and shunt resonator are disconnected from the ground busbar while in the second layout, the tuning electrodes are shorted

to the ground busbar. This is a proof of concept implementation using a standard SAW filter fabrication process with only one metal layer deposition and patterning step and without using any VO_2 switching elements. An optical image of the fabricated 6-pole SAW filter is shown in Figure 5-24. As shown in the measured S-parameter response of the fabricated filters in Figure 5-25, the filter's center frequency can be tuned from 970 MHz to 944 MHz while the insertion loss is better than 3.6 dB over the tuning range and the bandwidth is maintained around 36 MHz.

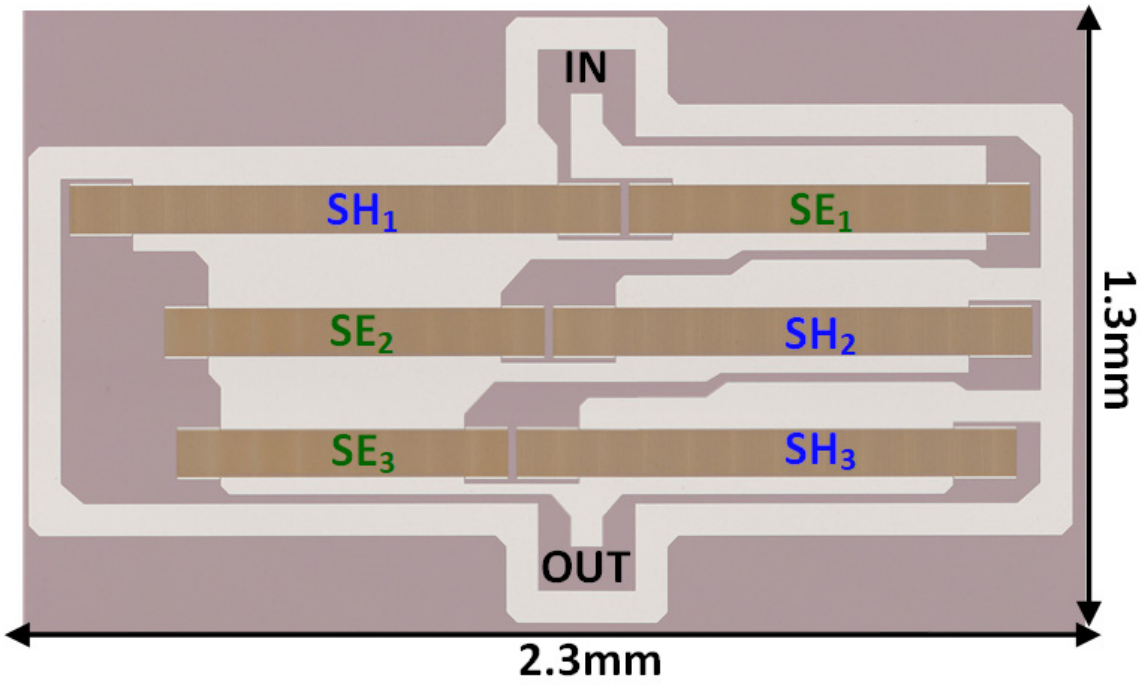

Figure 5-24: Optical image of the fabricated 6-pole SAW filter.

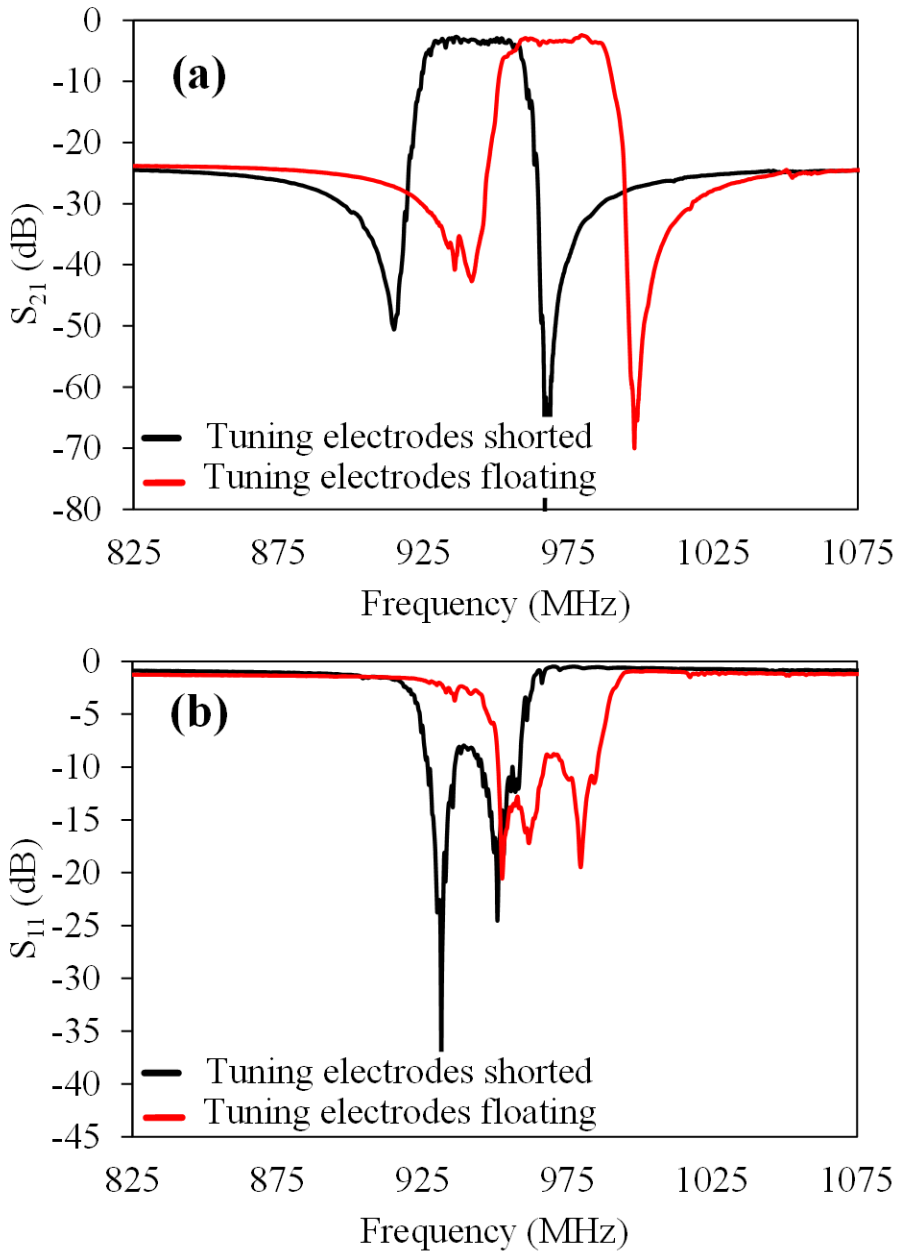

Figure 5-25: Measured S-parameter response of the 6-pole SAW filters for both tuning states.

The implementation of a tunable 3-pole SAW filter using the proposed reconfigurable SAW resonators and fully integrated VO_2 switching elements is presented in Figure 5-26 which also shows a close-up view of the monolithically integrated VO_2 switches. The 3-pole tunable filter is fabricated using the 5-mask in-house fabrication process. The total area of the 3-pole filter

including the three VO_2 switching elements, DC bias lines and pads is 1.6 mm × 4.2 mm. Measurement results for the tunable filter for both tuning states are presented in Figure 5-27. For the high frequency state, when the VO_2 switches are OFF, the filter has a center frequency at 733 MHz with a bandwidth of 24 MHz. The measured insertion loss for this state is better than 2.44 dB. When the VO_2 switches are turned ON, the filter is tuned to a lower center frequency at 713 MHz, the bandwidth is 22 MHz and the maximum insertion is 2.5 dB.

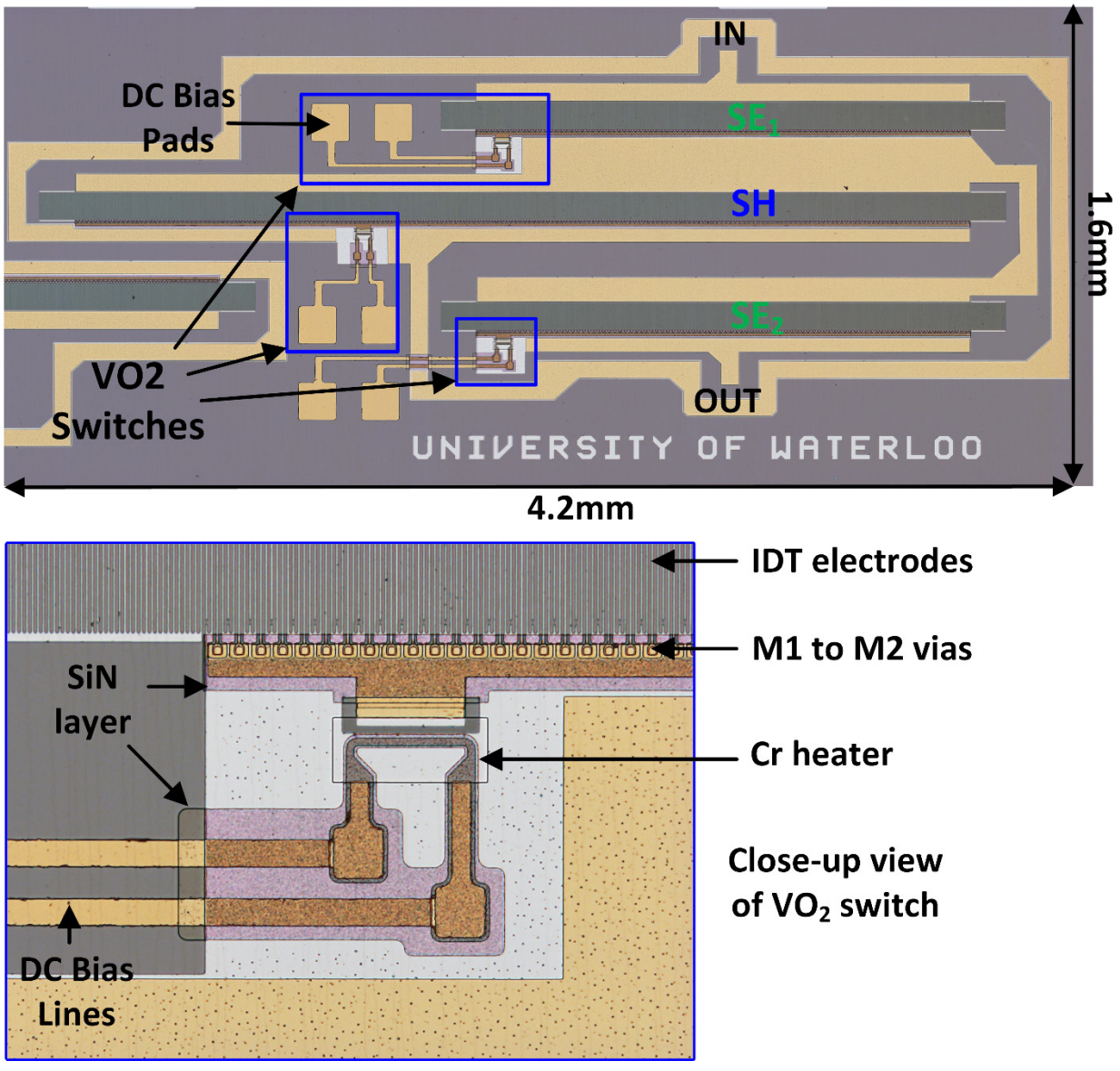

Figure 5-26: Fabricated tunable 3-pole filter and close-up view of the monolithically integrated VO_2 switches.

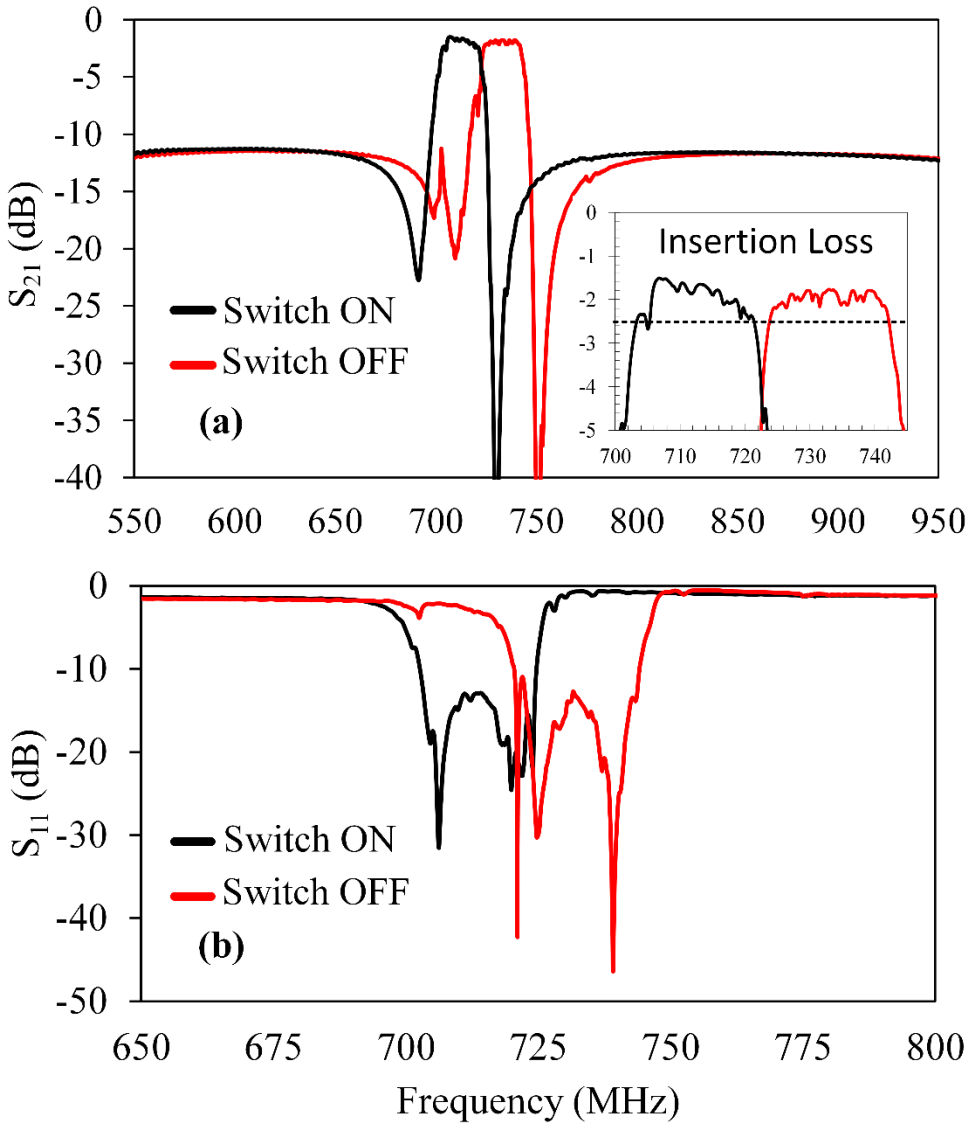

Figure 5-27: Measured S-parameter response of the 3-pole tunable SAW filter for different tuning states.

The high power measurement results for the fabricated tunable filter are presented in Figure 5-28. A high power input tone from 30 dBm up to 40 dBm is applied at the input port and the output power (P_{out}) is measured from the filter's other port for both the lower frequency and higher frequency states. The filter can handle up to 40 dBm (10 Watt) input power for the low frequency state without any permanent damage to the resonators or the VO_2 switches. For the high frequency

state, the filter can handle up to 38 dBm input power and there is an irreversible change in the S_{21} response at 40 dBm. The permanent failure, as shown in the optical image of Figure 5-28 (b), is due to the damage to the aluminum electrodes and not due to the VO_2 switches used for tuning. This is a known power handling issue for SAW resonators and filters which can be addressed with a better choice of material for the electrodes.

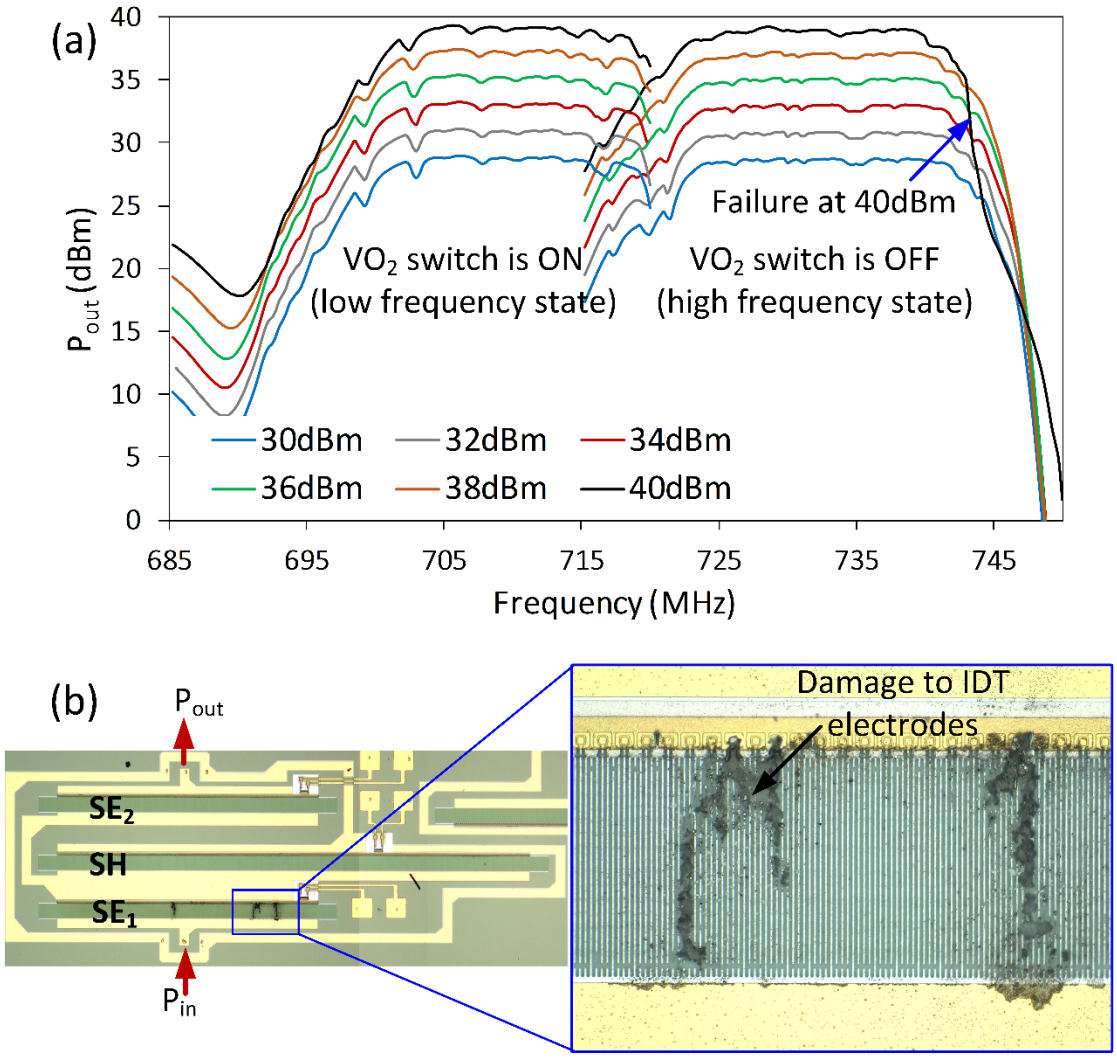

Figure 5-28: Measured output power (P_{out}) for different input power levels for the fabricated tunable filter (a) and optical image of the damaged resonator (b).

The nonlinear performance of the filter in terms of 2nd harmonic emission for both tuning states is presented in Figure 5-29. The 2nd harmonic emission of the filter is measured using a single-tone nonlinear test setup and by applying a 23 dBm tone at the input port and measuring the 2nd harmonic from the output port. Similar to the nonlinear measurement results for a single resonator, as shown in Figure 5-19, the tunable filter shows a higher 2nd harmonic emission for the low frequency state when the VO_2 switches are turned ON and the tuning electrodes are connected to the ground busbars which is due to the higher electric field within the piezoelectric layer for this state.

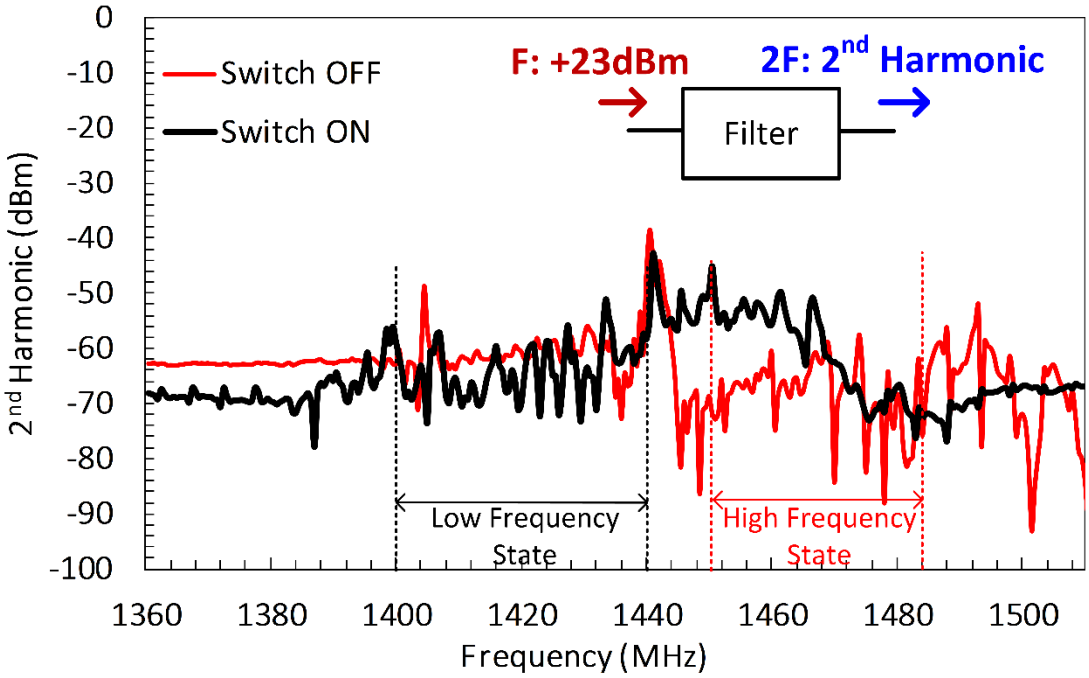

Figure 5-29: Measured nonlinear performance of the tunable filter.

Table 5.5 compares the performance of tunable SAW filters that previously reported using technologies such as BST variable capacitors (varactors), MEMS varactors with the proposed tunable filter in this reach work which is based on using the monolithically integrated vanadium

dioxide switches. Using the vanadium dioxide switches with compact size enables the monolithic integration of the switches with SAW resonators for implementation of tunable filters without any major performance degradation or increase of the filter size.

Table 5.5: Comparison between the previous works on tunable SAW filters and this research work.

Publication	Frequency Range	Max Insertion Loss	Power Handling	2nd harmonic Nonlinearity	Technology /Size
Ref. [29]	905-925MHz	2dB	NA	NA	Fixed capacitors for each state/0.9mm×1.9 mm
Ref. [47]	3MHz BW tunability at 1.004GHz	10dB	NA	NA	BST Varactors/ 3mm×2.5mm
Ref. [58]	7MHz BW and center frequency tunability (1.07GHz-1.063GHz)	7dB	NA	NA	MEMS Varactors/2.55m m×1.2mm
This Research	713-733MHz	2.5dB	38dBm	-65dBm, -70dBm (Low & High Freq) States	Vanadium Dioxide Switches/4.2mm× 1.6mm

5.6 Summary

Reconfigurable SAW resonators with tunable frequency have been presented and experimentally demonstrated using monolithically integrated VO_2 switches. A new configuration of interdigitated electrodes was proposed to enable resonance frequency tuning through integration of switches with some of the metal electrodes. The first reconfigurable resonator utilizes multiple VO_2 switching elements integrated with the electrodes. Six heater elements distributed over the tuning electrodes were required in order to achieve a uniform temperature profile for a reliable

operation and tuning of the resonator. The resonator's center frequency was tuned from 720 MHz to 700 MHz (20 MHz tuning range) without any major degradation in resonator's RF performance. A DC bias voltage of 2 V and a bias current of 740 mA were required to tune the resonator. A modified structure of the reconfigurable SAW resonator was demonstrated where the tuning electrodes are connected to a 2nd metal electrode through vias and a single VO_2 switching element was used for tuning. The modified structure results in ten times reduction in the consumed DC power in addition to other performance improvements such as reduction in thermal cross-talk between the heater element and the SAW resonator and reducing the frequency shift due to temperature drift. The use of a single VO_2 switch also allows even a higher level of integration for a practical use of the proposed resonators in a tunable filter. A 3-pole tunable filter was designed and implemented using the proposed reconfigurable SAW resonators. The filter's center frequency is tuned from 733 MHz to 713 MHz while the insertion loss was maintained below 2.5 dB. The fabricated SAW resonators and filters also showed acceptable linear and high-power performance characteristics. To our knowledge, this is the first time that reconfigurable SAW resonators and tunable filters with monolithically integrated VO_2 switches are presented.

Chapter 6

Conclusions

The main focus of this thesis is on the design and development of high-performance reconfigurable filters with switchable and tunable frequency response using piezoelectric SAW technology. This is achieved through monolithic integration of the SAW resonators with VO_2 based switching elements that allow the practical implementation of RF reconfigurable filters with acceptable RF performance. To conclude this thesis, the major contributions of the research are summarized and some of the issues that can be addressed as future work are given in this chapter.

6.1 Contributions

The major contributions for this thesis are summarized as follows:

- TPoS resonators based on AlN piezoelectric material and single crystalline silicon substrate with different electrode dimensions are developed. The resonators are fabricated using commercially available PiezoMUMPs process. The main advantage for this type of resonators is ultra-high quality factor in excess of 6200 at room temperature, however because of extremely low coupling coefficient, $kt^2 \sim 0.1\%$, the achievable bandwidth for the filters constructed using these resonators is very low. To investigate the effect of temperature on filter's performance in terms of insertion loss, a 3-pole filter was implemented and measured using a cryogenic probe station at -196°C up to +120ºC. Measured results show an improvement of quality factor from 6200 to 8830 for a single

resonator while the insertion loss for the fabricated 3-pole filter is improved by 2.9 dB. Nonlinear characterization of the fabricated resonators is also performed using a single tone 2nd harmonic measurement setup. The peak value of 2nd harmonic changes from -76 dBm to -52 dBm (24 dBm variation) while the incident power is swept from 8 dBm up to 20 dBm.

- Reconfigurable multi-band filters that are capable of switching several frequency channels ON and OFF are realized by integration of VO_2 switching elements within the resonators of the filters. A switched dual band filter is implemented using hybrid integration of discrete VO_2 switches with SAW filters and using wire bonds. The fabricated 5-pole dual-band filter including two VO_2 switches, two SAW filters, and the wire bonds assembled on an alumina carrier substrate is 3.3 mm × 7.2 mm in size. When both channels are ON, the dual-band filter has an insertion loss of 3.7 dB at low channel (765 MHz) and 3.9 dB at the upper channel (935 MHz), respectively. The isolation when both filters are turned OFF is better than 9.8 dB for both high and low channels. The reason for the limited performance in terms of isolation is due to the parasitic inductance of the wire bonds using the hybrid integration approach.
- Another implementation for the switched dual-band filter is presented by monolithic integration of the VO_2 switches on the same chip as the SAW filters. The monolithic integration allows the implementation of higher order filters with improved RF performance. A switched 7-pole dual-band filter using six VO_2 switching elements (three for each channel) is designed and fabricated. For this implementation each shunt resonator within the filter is connected in parallel with a monolithically integrated VO_2 switching element. The total area of the filter including two 7-pole filters, six VO_2 switches, matching

inductors, DC bias pads and RF testing pads is only 2.8 mm × 5.3 mm. When both channels are ON, the dual-band filter has an insertion loss of 3.2 dB for both low and high channels. In order to turn each channel OFF it is possible to detune the middle shunt resonators by actuating the VO_2 switches connected to these resonators. By detuning only the middle shunt resonator within each filter, a maximum isolation of 20 dB is achieved, which is roughly 10 dB better than the isolation achieved for the previous switched dual-band filter using the hybrid integration approach. It is also possible to detune all three shunt resonators by actuating all three VO_2 switches within each filter at the same time. The isolation for each channel when all three shunt resonators are detuned is better than 40 dB. The main advantages of monolithic integration in comparison to hybrid integration are size reduction and improved performance in terms of high isolation.

- A novel reconfigurable SAW resonator with tunable center frequency is developed by utilizing tuning electrodes and monolithically integrated VO_2 switches. Resonance frequency can be tuned from low to high frequency state by switching the VO_2 switches to ON and OFF states. The proposed tuning concept can be extended to other frequencies and higher number of tuning states. A first reconfigurable SAW resonator is implemented using VO_2 switches that are directly connected to the tuning electrodes. The frequency of the resonator is tuned between two different states from 700 MHz to 720 MHz while the resonator maintains a quality factor better than 350 over the tuning range. For a reliable operation of all the switching elements, a uniform temperature above the transition temperature of 70ºC is required which is only possible by utilizing multiple heater elements increasing the amount of required DC power consumption and the complexity of the structure. To address this issue, a second structure is proposed using a modified fabrication

process to include a top electrode that is used to indirectly connect the tuning electrode to a single VO_2 switching located outside the active area of the resonator. The fabricated tunable SAW resonator shows a tuning range of 18 MHz by utilizing a single VO_2 switching element that connects the tuning electrodes to the ground busbar through the top metal electrode and via connections. A DC bias voltage of 6 V with a DC bias current of 21 mA is required to turn the VO_2 switch ON. The required DC power is ten times smaller than the DC power required for the previous reconfigurable SAW resonator using six switching. In addition to lower DC power, the modified structure also reduces the thermal crosstalk between the heater element and the SAW resonator and hence reduces the frequency shift due to temperature drift. The use of a single VO_2 switch also allows a higher level of integration for a practical use of the proposed resonators in a tunable filter. A 3-pole tunable filter including two series and one shunt resonator is designed and implemented with a total area of 1.6 mm × 4.2 mm. The filter's center frequency is tuned from 733 MHz to 713 MHz while the insertion loss is maintained below 2.5 dB. The fabricated SAW resonators and filters also showed good linear and high-power performance characteristics. This is the first successful demonstration of reconfigurable SAW resonators and filters with tunable center frequency employing monolithically integrated VO_2 switches.

6.2 Future Works

There has been an extensive research and investigation of a wide range of topics in this thesis to advance the development of reconfigurable resonators and filters using piezoelectric SAW technology and integration with VO_2 switches. However, there are several unexplored issues that are suggested for researchers who want to further explore this field.

- An investigation of the proposed reconfigurable SAW technology is required in terms of lifetime and reliability characterization of the VO_2 switches which plays an important role in the manufacturing of the developed filters for commercial wireless applications. Environmental effects such as ambient temperature can also influence the performance of these devices. The transition temperature for VO_2 material which is about 70°C is below the typical maximum temperature of 85ºC required for the safe operation of RF components used in frontend modules. Alternative phase change materials such as Germanium Telluride (GeTe) with a higher transition temperature around 220ºC can be employed to address this issue.
- Another problem related to the use of VO_2 switches is the requirement for a continuous application of a DC bias to keep the switches in their ON state. It is possible to utilize latching mechanisms for phase change materials such as GeTe without the need for a continuous application of DC bias.
- Although we presented the application of switching mechanisms for only SAW resonators, similar switching methods can be applied to other piezoelectric technologies such as BAW and FBAR resonators.
- The proposed tunable SAW resonator concept based on programmable interdigitated electrodes can be extended to achieve more than only two frequency tuning states by

employing several sets of tuning electrodes and a higher number of VO_2 switching elements. Extensive FEM modeling and research can also be employed to improve the performance of the tunable SAW resonators discussed in this thesis in terms of spurious modes and also resonator quality factor by optimizing the dimensions of the metal electrodes and also the thicknesses of different layers present in the multi-layered piezoelectric substrate stack.

Bibliography

[1] ACMD-620 datasheet, available at: https://www.broaDCom.com/products/wireless/fbar/duplexer/acmd-6207

[2] R. Aigner, "Filter technologies for converged RF-frontend architectures: SAW, BAW and beyond," 2010 Topical Meeting on Silicon Monolithic Integrated Circuits in RF Systems (SiRF), New Orleans, LA, 2010, pp. 136-139.

[3] http://www.memscap.com/products/mumps/piezomumps/reference-material

[4] H. C. Nathanson, W. E. Newell, R. A. Wickstrom and J. R. Davis, "The resonant gate transistor," in IEEE Transactions on Electron Devices, vol. 14, no. 3, pp. 117-133, March 1967.

[5] J. G. Rodriguez-Madrid, G. F. Iriarte, J. Pedros, O. A. Williams, D. Brink and F. Calle, "Super-High-Frequency SAW Resonators on AlN/Diamond," in IEEE Electron Device Letters, vol. 33, no. 4, pp. 495-497, April 2012.

[6] B. Abbott et al., "Temperature compensated SAW with high quality factor," 2017 IEEE International Ultrasonics Symposium (IUS), Washington, DC, 2017, pp. 1-1..

[7] Y. Wang et al., "A zero TCF band 13 SAW duplexer," 2015 IEEE International Ultrasonics Symposium (IUS), Taipei, 2015, pp. 1-4.

[8] J. B. Shealy et al., "Low loss, 3.7GHz wideband BAW filters, using high power single crystal AlN-on-SiC resonators," 2017 IEEE MTT-S International Microwave Symposium (IMS), Honololu, HI, 2017, pp. 1476-1479.

[9] S. Tanifuji, Y. Aota, S. Kameda, T. Takagi and K. Tsubouchi, "Discussion of millimeter wave FBAR with very thin AlN film fabricated using MOCVD method," 2009 IEEE International Ultrasonics Symposium, Rome, 2009, pp. 2170-2173.

[10] M. Akiyama, T. Kamohara, K. Kano, A. Teshigahara, Y. Takeuchi and N. Kawahara, “Enhancement of piezoelectric response in scandium aluminum nitride alloy thin films prepared by dual reactive cosputtering,” Adv. Mater., vol. 21, no. 5, pp 593–596, Feb. 2008.

[11] V. Yantchev and I. Katardjiev, "Micromachined thin film plate acoustic resonators utilizing the lowest order symmetric lamb wave mode," in IEEE Transactions on Ultrasonics, Ferroelectrics, and Frequency Control, vol. 54, no. 1, pp. 87-95, January 2007.

[12] G. Piazza, P. J. Stephanou and A. P. Pisano, "Piezoelectric Aluminum Nitride Vibrating Contour-Mode MEMS Resonators," in Journal of Microelectromechanical Systems, vol. 15, no. 6, pp. 1406-1418, Dec. 2006.

[13] Gianluca Piazza, Philip J. Stephanou, Albert P. Pisano, "One and two port piezoelectric higher order contour-mode MEMS resonators for mechanical signal processing," Solid-State Electronics, Volume 51, Issues 11–12, 2007, Pages 1596-1608.

[14] M. Rinaldi, C. Zuniga and G. Piazza, "5-10 GHz AlN Contour-Mode Nanoelectromechanical Resonators," 2009 IEEE 22nd International Conference on Micro Electro Mechanical Systems, Sorrento, 2009, pp. 916-919.

[15] G. Piazza, P. J. Stephanou and A. P. Pisano, "Single-Chip Multiple-Frequency ALN MEMS Filters Based on Contour-Mode Piezoelectric Resonators," in Journal of Microelectromechanical Systems, vol. 16, no. 2, pp. 319-328, April 2007.

[16] R. Abdolvand and F. Ayazi, "Monolithic Thin-Film Piezoelectric-on-Substrate Filters," 2007 IEEE/MTT-S International Microwave Symposium, Honolulu, HI, 2007, pp. 509-512.

[17] R. Abdolvand, H. M. Lavasani, G. K. Ho and F. Ayazi, "Thin-film piezoelectric-on-silicon resonators for high-frequency reference oscillator applications," in IEEE Transactions on Ultrasonics, Ferroelectrics, and Frequency Control, vol. 55, no. 12, pp. 2596-2606, December 2008.

[18] R. T. Howe and R. S. Muller, "Resonant-microbridge vapor sensor," in IEEE Transactions on Electron Devices, vol. 33, no. 4, pp. 499-506, Apr 1986.

[19] Ark-Chew Wong and C. T. C. Nguyen, "Micromechanical mixer-filters ("mixlers")," in Journal of Microelectromechanical Systems, vol. 13, no. 1, pp. 100-112, Feb. 2004.

[20] J. R. Clark, Wan-Thai Hsu and C. T. C. Nguyen, "High-Q VHF micromechanical contour-mode disk resonators," International Electron Devices Meeting 2000. Technical Digest. IEDM (Cat. No.00CH37138), San Francisco, CA, USA, 2000, pp. 493-496.

[21] Jing Wang, Z. Ren and C. T. C. Nguyen, "1.156-GHz self-aligned vibrating micromechanical disk resonator," in IEEE Transactions on Ultrasonics, Ferroelectrics, and Frequency Control, vol. 51, no. 12, pp. 1607-1628, Dec. 2004.

[22] D. Weinstein and S. A. Bhave, "Internal Dielectric Transduction in Bulk-Mode Resonators," in Journal of Microelectromechanical Systems, vol. 18, no. 6, pp. 1401-1408, Dec. 2009.

[23] M. A. El-Tanani and G. M. Rebeiz, "High-Performance 1.5–2.5-GHz RF-MEMS Tunable Filters for Wireless Applications," in IEEE Transactions on Microwave Theory and Techniques, vol. 58, no. 6, pp. 1629-1637, June 2010.

[24] R. Mansour, "Multi-function RF filters," 2017 IEEE MTT-S International Microwave Workshop Series on Advanced Materials and Processes for RF and THz Applications (IMWS-AMP), Pavia, 2017, pp. 1-1.

[25] C. H. Ko, K. M. J. Ho, R. Gaddi and G. M. Rebeiz, "A 1.5–2.4 GHz tunable 4-pole filter using commercial high-reliability 5-bit RF MEMS capacitors," 2013 IEEE MTT-S International Microwave Symposium Digest (MTT), Seattle, WA, 2013, pp. 1-4.

[26] L. Pantoli, V. Stornelli and G. Leuzzi, "A wideband class-AB tunable active filter," 2015 European Microwave Conference (EuMC), Paris, 2015, pp. 1272-1275.

[27] K. Kiela and R. Navickas, "Active low-pass filter design with variable filter order for wideband transceivers," 2015 IEEE 3rd Workshop on Advances in Information, Electronic and Electrical Engineering (AIEEE), Riga, 2015, pp. 1-4.

[28] T. Omori, K. Seo, T. F. C. J. Ahn and K. y. Hashimoto, "Flexible RF one-chip active filter based on recursive architecture in UHF range," 2014 Asia-Pacific Microwave Conference, Sendai, Japan, 2014, pp. 1309-1311.

[29] T.Komatsu, K.Hashimoto, T.Omori and M.Yamaguchi, “Tunable Radio Frequency Filters Using Acoustic Wave Resonators and Variable Capacitors,” Jpn. J. Appl. Phys., 49, 7 (2010).

[30] M.Inaba, T.Omori, and K.Hashimoto, “A Configuration of Widely Tunable Surface Acoustic Wave Filter,” Jpn. J. Appl. Phys., 52, 7 (2013).

[31] T.Samoto, et al, “Wafer-to-wafer Transfer Process of Barium Strontium Titanate for Frequency Tuning Applications using Laser Pre-irradiation,” Journal of Micromechanics and Microengineering, 23 (2013).

[32] M. Kadota and S. Tanaka, "Ultra-wideband ladder filter using SH_0 plate wave in thin $LiNbO_3$ plate and its application to tunable filter," in IEEE Transactions on Ultrasonics, Ferroelectrics, and Frequency Control, vol. 62, no. 5, pp. 939-946, May 2015.

[33] X. Zhu, V. Lee, J. Phillips and A. Mortazawi, "An Intrinsically Switchable FBAR Filter Based on Barium Titanate Thin Films," in IEEE Microwave and Wireless Components Letters, vol. 19, no. 6, pp. 359-361, June 2009.

[34] V. Lee, S. A. Sis, J. D. Phillips and A. Mortazawi, "Intrinsically Switchable Ferroelectric Contour Mode Resonators," in IEEE Transactions on Microwave Theory and Techniques, vol. 61, no. 8, pp. 2806-2813, Aug. 2013.

[35] S. Lee and A. Mortazawi, "An Intrinsically Switchable Ladder-Type Ferroelectric BST-on-Si Composite FBAR Filter," in IEEE Transactions on Ultrasonics, Ferroelectrics, and Frequency Control, vol. 63, no. 3, pp. 456-462, March 2016.

[36] M. Z. Koohi, S. Lee and A. Mortazawi, "Fabrication of a Low insertion loss intrinsically switchable BAW filter based on BST FBARs," 2017 IEEE MTT-S International Microwave Symposium (IMS), Honololu, HI, 2017, pp. 1480-1483.

[37] V. Yantchev, and I. Katardijiev, "Micromachined thin film plate acoustic resonators utilizing the lowest order symmetric lamb wave mode", IEEE Tran. on Ultrasonics, 54 (1), pp. 87-95, Jan 2007.

[38] G. Piazza, P. J. Stephanou, and A. P. Pisano "One and two port piezoelectric higher order contour-mode MEMS resonators for mechanical signal processing", J. of Solid-State Electronics, vol. 51, pp. 1596-1608, Dec 2007.

[39] H. Zhu, C. Tu, and J. E. Lee, "High-Q low impedance UHF-band AlN-on-Si MEMS resonators using quasi-symmetrical lamb wave modes", IEEE-MEMS Int., Conf., Shanghai, 2016, pp. 970-973.

[40] A. F. Azarnaminy and R. R. Mansour, "Analysis of Aluminum Nitride Resonators and Filters Over Temperature and Under High Power," 2019 20th International Conference on Solid-State Sensors, Actuators and Microsystems & Eurosensors XXXIII (TRANSDUCERS & EUROSENSORS XXXIII), 2019, pp. 897-900.

[41] C.-M. Lin, Y.-Y. Chen, V. V. Felmetsger, D. G. Senesky, and A. P. Pisano, "AlN/3C–SiC composite plate enabling high-frequency and high-Q micromechanical resonators," Adv. Mater., vol. 24, pp.2722–2727, May 2012.

[42] Jie Zou, " High Quality Factor Lamb wave Resonator," M.S. thesis, Dept. Electrical and Computer Engineering, University of California at Berkeley, Berkeley, US, Jan 2015

[43] D. A. Feld, R. Parker, R. Ruby, P. Bradley and S. Dong, "After 60 years: A new formula for computing quality factor is warranted," 2008 IEEE Ultrasonics Symposium, Beijing, 2008, pp. 431-436.

[44] R. R. Mansour, F. Huang, S. Fouladi, W. D. Yan and M. Nasr, "High-Q Tunable Filters: Challenges and Potential," in IEEE Microwave Magazine, vol. 15, no. 5, pp. 70-82, July-Aug. 2014.

[45] L. Gao, T. Lin, and G. M. Rebeiz, "Design of tunable multi-pole multi-zero bandpass filters and diplexer with high selectivity and isolation," IEEE Trans. Circuits Syst. I, Reg. Papers, vol. 66, no. 10, pp. 3831–3842, Oct. 2019.

[46] P. D. Laforge, R. R. Mansour, and M. Yu, "Reconfigurable MEMS-based BPF for manifold-coupled-superconducting triplexers," IEEE Trans. Appl. Supercond., vol. 28, no. 6, pp. 1–8, Sep. 2018.

[47] K. Y. Hashimoto et al., “Moving tunable filters forward: A ‘heterointegration’ research project for tunable filters combining MEMS and RF SAW/BAW technologies,” IEEE Microw. Mag., vol. 16, no. 7, pp. 89–97, Aug. 2015.

[48] G. Hummel, Y. Hui, and M. Rinaldi, “Reconfigurable piezoelectric MEMS resonator using phase change material programmable vias,” J. Microelectromech. Syst., vol. 24, no. 6, pp. 2145–2151, Dec. 2015.

[49] A. F. Azarnaminy, J. Jiang, and R. R. Mansour, “Switched dual-band SAW filter using vanadium oxide switches,” in IEEE MTT-S Int. Microw. Symp. Dig., Jun. 2021, pp. 677–680.

[50] T. Takai et al., “IHP SAW technology and its application to microacoustic components,” in Proc. IEEE Int. Ultrason. Symp. (IUS), Washington, DC, USA, Sep. 2017, pp. 1–8.

[51] NGK Insulators, Ltd. Accessed: Dec. 1, 2021. [Online]. Available: https://www.ngk-insulators.com/en/products/wafer.html

[52] R. J. Cameron, C. M. Kudsia, R. R. Mansour, “Microwave filters for communication systems: Fundamentals, Design, and Applications”, New Jersey, Wiley, 2018.

[53] M. J. Blasco, “A Coupling Matrix Vision For Mobile Filtering Devices With Micro-Acoustic Wave Technologies, A Systematic Approach,” Ph.D. Thesis, Universitat Autonoma de Barcelona, July 2015.

[54] A. Fouladi Azarnaminy and R. R. Mansour, "Switched Dual-Band SAW Filters Using Hybrid and Monolithically Integrated Vanadium Oxide Switches," in IEEE Transactions on Microwave Theory and Techniques, vol. 70, no. 1, pp. 876-885, Jan. 2022, doi: 10.1109/TMTT.2021.3130597.

[55] INRS, Dec. 2021, [online] Available: https://inrs.ca/en/research/research-facilities/find-a-research-facilitie/laboratory-of-micro-and-nanofabrication.

[56] A. O. Suleiman et al., "Probing the role of thermal vibrational disorder in the SPT of VO_2 by Raman spectroscopy ", Sci. Rep., vol. 11, pp. 1620, Jan. 2021.

[57] CIRFE, Dec. 2021, [online] Available: https://uwaterloo.ca/centre-integrated-rf-engineering.

[58] A. Konno, H. Hirano, M. Inaba, K. Hashimoto, M. Esashi, and S. Tanaka, “Tunable surface acoustic wave filter using integrated micro-electro-mechanical-system based varactors made of electroplated gold,” Jpn. J. Appl. Phys., vol. 52, no. 7, pp. 07HD13– 07HD13-5, 2013.

[59] A. F. Azarnaminy, A. O. Suleiman, M. Chaker and R. R. Mansour, “A Reconfigurable SAW Resonator Using Monolithically Integrated Switches,” in IEEE MTT-S Int. Microw. Symp. Dig., Jun. 2022 (Accepted for Presentation)

[60] K. Hashimoto, “Analysis for Multi-Electrode IDTs,” in Surface Acoustic Wave Devices in Telecommunications, Berlin: Springer, 2000, pp.221-227.

[61] T. Kodama, H. Kawabata, Y. Yasuhara and H. Sato, "Design of Low-Loss SAW Filters Employing Distributed Acoustic Reflection Transducers," IEEE 1986 Ultrasonics Symposium, 1986, pp. 59-64.

[62] S. Gong and G. Piazza, "Large frequency tuning of Lithium Niobate laterally vibrating MEMS resonators via electric boundary reconfiguration," 2013 Transducers & Eurosensors XXVII: The 17th International Conference on Solid-State Sensors, Actuators and Microsystems, 2013, pp. 2465-2468.

[63] H. Iwamoto, T. Takai, Y. Takamine, T. Nakao, T. Fuyutsume and M. Koshino, "Transverse Modes in I.H.P. SAW Resonator and Their Suppression Method," 2018 IEEE International Ultrasonics Symposium (IUS), 2018, pp. 1-4.

[64] Bahl S K and Chopra K L 1970 Amorphous versus crystalline GeTe films. III. Electrical properties and band structure J. Appl. Phys. 41 2196–212.